



Norwegian University of
Science and Technology

Synthesis of high-temperature solid sorbents for CO₂ capture

Ane Sofie Lilleng

Chemical Engineering and Biotechnology

Submission date: June 2018

Supervisor: Edd Anders Blekkan, IKP

Co-supervisor: Li He, IKP

Kumar Ranjan Rout, IKP

De Chen, IKP

Norwegian University of Science and Technology

Department of Chemical Engineering

Preface

This master thesis marks the end of five years at the Norwegian University of Science and Technology (NTNU). The thesis is written for the Catalysis group at the Department of Chemical Engineering, and is a continuation of the master thesis of Mawanga Moses written during the spring 2017. This work is performed in collaboration with Gassnova in conjunction with the project *Moving Bed Carbonate-Looping (MBCL) Technology for Post-combustion CO₂ capture*.

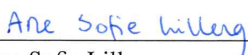
I would like to express my gratitude to my supervisor Professor Edd Anders Blekkan for providing an excellent learning environment during the weekly meetings. I would also like to thank my co-supervisors Dr. Li He and Dr. Kumar Ranjan Rout for supplying highly appreciated help and guidance whenever I needed. Thanks to the PhD student Jianyu Ma at the Catalysis group for good advices regarding picture-taking with SEM and thanks to the laboratory technician Lars Erik Mollan Parnas from SINTEF AS Industry for performing the mercury porosimetry experiments.

The sections 1.1, 3.4, 3.5, 3.6, 4.1.1, 4.2.1, 4.2.2 and 4.2.4 are inspired by previous work [1].

The Research Council of Norway is acknowledged for the support to the Norwegian Micro- and Nano-Fabrication Facility, NorFab, project number 245963/F50.

I declare that this is an independent work according to the exam regulations of the Norwegian University of Science and Technology.

Trondheim, 18.06.2018


Ane Sofie Lilleng

Abstract

The use of fossil fuels have escalated since the first industrial applications at the mid 19th century with a consequence of increased emissions of CO₂ and other green house gases. As a result, the global climate has been affected negatively and caused an elevated global average temperature. Because of this it is desirable to limit further emissions of green house gases, especially CO₂ which is the main contributor. Carbon Capture and Storage technology (CCS) is an interesting solution, but due to disadvantages of the present state of the art technology, high-temperature solid sorbents are investigated as a possible solution. CaO-based sorbents have gained attention since they have a high CO₂ capacity and the raw materials are cheap and abundant. The disadvantage of this technology is a steep decline in capacity during the initial carbonation-calcination cycles which is attributed to sintering. The goal of this work was to synthesize high-temperature solid CaO-based sorbents for CO₂ capture by incorporation of dopants in calcined dolomite. The scope of this work was also to determine the optimal sorbent composition that gives the highest cyclic stability. The dopants form metal oxides upon heat treatment which acts as a structural stabilization among the CaO-particles.

This work have utilized dolomite as the CaO-source for the synthesis. Dolomite, which is CaCO₃MgCO₃, was calcined at 800 °C for 6 hours to make the CaO source. Sorbents were prepared using a one-pot granulation procedure which consists of impregnation and granulation. Calcined dolomite was doped with the elements Mg, Zr, Al and Ce using incipient wetness impregnation. Mostly soluble precursors were used, but cement was also utilized as an Al-precursor since it is easier to handle and a cheaper alternative. Granulation was performed after impregnation, and the dried sorbents were sifted into four size ranges, < 250 μm, 250-500 μm, 500-850 μm and > 850 μm. The sorbents were pre-calcined at 800 °C for 3 hours in an inert atmosphere and at 950 °C for 3 hours in an atmosphere containing air. The sorbents with the size 500-850 μm were tested under wet carbonation conditions in the TGA. Carbonation was run at 570 °C with 10 % CO₂ and 8 % steam balanced with Ar. Calcination was run at 950 °C with 100 % CO₂. The sorbents were characterised using N₂ adsorption-desorption, mercury porosimetry, XRD, a mechanical falling test, SEM and EDS. Calcined dolomite was also characterised using the three former methods.

The impregnation of the dopants Mg, Zr, Al and Ce gave the stabilizing phases MgO, CaZrO₃, Ca₁₂Al₁₄O₃₃ and CeO₂. The capturing capacity in the first cycle, C₁, was comparable for most sorbents with a value around 30 %, except the sorbents Al(insol)Mg and Al(insol)_AZr which had an initial capacity of 23.3 % and 36.1 %, respectively. The specific surface area and pore volume of the sorbents were lower compared to calcined dolomite, and this was attributed to the pre-calcination procedure. The adsorption isotherms and the pore size distribution plots revealed that calcined dolomite and the sorbents had similar features in the mesoporous range, except for a higher volumetric appearance of pores in the raw material. The mercury intrusion experiment showed that the sorbents Al(insol)Ce and Al(insol)_AZr had a lower volumetric appearance of macropores and a shift in maximum when compared to calcined dolomite. It was not observed any relations between C₁

and specific surface area, nor C_1 and pore volume. It was speculated that this was due to the relatively narrow range of values these parameters lay in.

The examination of the raw files from the TGA experiments showed that the captured CO_2 was released during the regeneration step. The deactivation of sorbents was therefore not because of permanent trapping of CaCO_3 in the pores, but rather sintering of CaO particles. This result was supported by comparing SEM pictures of fresh and spent sorbents which revealed that carbonation-calcination cycling lead to larger particles and a more compact structure.

An elemental mapping was performed of the sorbents $\text{Al}(\text{sol})\text{Mg}$ and $\text{Al}(\text{sol})\text{Mg}$ to explore if the use of different Al-precursors lead to differences in distribution of aluminium. It was found that the distribution of aluminium using aluminium nitrate as precursor was slightly more even compared to utilization of cement as the precursor. An elemental mapping of the least and most stable sorbents relative to cycle 14, $\text{Al}(\text{insol})_A\text{Zr}$ and MgZr , was also performed. The analysis showed that both sorbents had some areas which exhibited higher concentration of dopants within the analyzed area. Therefore it was speculated that the slightly inhomogeneous distribution of dopants was only one of the factors affecting cyclic stability.

The sorbents $\text{Al}(\text{sol})\text{Ce}$, $\text{Al}(\text{insol})\text{Mg}$ and MgZr stood out since they had the highest stability from cycle 14 to 68. The relative loss in CO_2 capacity from cycle 14 to 68 was 31.6 %, 25.0 % and 11.8 %, respectively, unlike the sorbent $\text{Al}(\text{insol})_A\text{Zr}$ which had the lowest stability from cycle 14 to 68 with a relative loss of 50.0 % during these cycles. It was difficult to observe a relation between Tammann temperature of the stabilizing phase and the cyclic stability among these three sorbents. This was because the sorbents contained the four stabilizing phases in various combinations, and the Tammann temperature lay in the relatively narrow range 1275-1483 °C, except for $\text{Ca}_{12}\text{Al}_{14}\text{O}_{33}$ which had a Tammann temperature of 744 °C.

The material loss in the first drop of the falling test showed that the sorbent $\text{Al}(\text{sol})\text{Ce}$ had an exceptionally high material loss of 19 %, unlike the sorbents $\text{Al}(\text{insol})\text{Mg}$ and MgZr which had material losses of 2.9 % and 0.59 %. The overall capacity values of the sorbents $\text{Al}(\text{insol})\text{Mg}$ and MgZr were compared. The values stabilized at a value around 10 % for the former and 12 % for the latter. Therefore, the sorbent MgZr was found to have a trade-off between the three important parameters cyclic stability, CO_2 capturing capacity and material loss. This sorbent consisted of 2.8 wt% Mg and 1.9 wt% Zr, so this was found to be the optimal sorbent composition among the tested sorbents.

Sammendrag

Bruken av fossile brenslere har eskalert siden de først ble brukt i industrielle anvendelser på midten av 1900-tallet. Konsekvensen har vært økte utslipp av CO₂ og andre drivhusgasser som har påvirket det globale klimaet og er en av årsakene til at den globale middeltemperaturen har økt. Det er derfor ønskelig å begrense videre utslipp av drivhusgasser, spesielt CO₂ som er den største bidragsyteren. Karbonfangst og -lagring er derfor en interessant løsning. På grunn av ulemper ved den mest brukte nåværende teknologien blir sorbenter undersøkt som en mulig erstatning. Høy-temperatur sorbenter basert på CaO har fått oppmerksomhet på grunn av høy kapasitet for å fange opp CO₂ i tillegg til at billige råmaterialer finnes i store mengder i naturen. En av utfordringene ved å bruke CaO baserte sorbenter er en bratt nedgang i CO₂-kapasitet i løpet av de første karboneringskalsineringssyklusene på grunn av sintring. Målet med dette arbeidet var å syntetisere høy-temperatur CaO-sorbenter for CO₂ fangst ved å tilsette ulike elementer til kalsinert dolomitt, og bestemme den optimale sammensetningen som leder til den høyeste sykliske stabiliteten. Elementene danner metalloksider ved varmebehandling og fungerer som en strukturell stabilisering blant CaO-partiklene.

I dette arbeidet ble dolomitt brukt som CaO-kilde i syntesen. Dolomitt, som foreligger naturlig som CaCO₃MgCO₃, ble kalsinert ved 800 °C i 6 timer for å lage CaO-kilden. Kalsinert dolomitt ble deretter impregnert med elementene Mg, Zr, Al og Ce. Det ble for det meste brukt vannløselige salter som kilde til disse elementene, men sement ble også brukt som kilde til Al fordi det er lett å håndtere og et billigere alternativ. Granulering ble utført etter impregnering, og de tørkede sorbentene ble siktet og delt inn i fire størrelser, < 250 μm, 250-500 μm, 500-850 μm and > 850 μm. Sorbentene ble deretter kalsinert ved 800 °C i 3 timer i en inert atmosfære, og ved 950 °C i 3 timer i en atmosfære av luft. Sorbenter med størrelse 500-850 μm ble testet under våte karboneringsforhold i en termogravimetrisk analyse. Karbonering ble kjørt ved 570 °C med 10 % CO₂ og 8 % vandamp balansert med Ar. Kalsinering ble kjørt ved 950 °C med 100 % CO₂. De kalsinerte sorbentene ble karakterisert med N₂ adsorpsjon-desorpsjon, kvikksølvporosimetri, røntgen-diffraksjon, en mekanisk falletest, sveipeelektronmikroskop og røntgenfluorescensspektrometri. Kalsinert dolomitt ble også karakterisert med de tre førstnevnte karakteriseringsmetodene.

Impregneringen med elementene Mg, Zr, Al og Ce førte til dannelse av de stabiliserende fasene MgO, CaZrO₃, Ca₁₂Al₁₄O₃₃ og CeO₂. Kapasiteten til å fange CO₂ i den første syklusen, C₁, var sammenlignbar for de fleste av sorbentene med en verdi rundt 30 %, utenom sorbentene Al(insol)Mg og Al(insol)_AZr som hadde 23.3 % og 36.1 % kapasitet i den første syklusen. Det spesifikke overflatearealet og porevolumet til sorbentene var lavere sammenlignet med kalsinert dolomitt, og dette var forårsaket av pre-kalsineringen. Adsorpsjonsisotermene og fordelingen i porestørrelse viste at kalsinert dolomitt og sorbentene hadde lignende trekk i det mesoporøse området, utenom en høyere volumetrisk forekomst av porer i råmaterialet. Kvikksølvporosimetri viste at sorbentene Al(insol)Ce og Al(insol)_AZr hadde en lavere volumetrisk forekomst av makroporer og et skift i maksimum sammenlignet med kalsinert dolomitt. Det ble ikke oppdaget en sammenheng mellom C₁

og spesifikt overflateareal, og heller ikke mellom C_1 og porevolum. Det er spekulert i at årsaken bak dette er at det spesifikke overflatearealet og porevolumet til sorbentene ligger i et relativt snevert område.

Råfilene fra TGA eksperimentene viste at all CO_2 som var fanget ble frigitt under regenereringen av sorbentene. Nedgangen i kapasitet til å fange opp CO_2 er derfor mest sannsynlig ikke på grunn av permanent fanget $CaCO_3$ i porene, men heller sintring av CaO partikler. Dette resultatet ble støttet av SEM-bilder av ferske og brukte sorbenter. Disse bildene viste at karbonering-kalsinering syklusene førte til større partikler og en mer kompakt struktur.

En elementanalyse ved bruk av EDX ble utført på sorbentene $Al(sol)Mg$ og $Al(insol)Mg$ for å undersøke fordelingen av aluminium ved bruk av aluminiumnitrat of sement som kilder. Det ble funnet at fordelingen av aluminium ved bruk av aluminiumnitrat var litt mer jevn enn ved bruk av sement. En elementanalyse av sorbentene med lavest og høyest stabilitet relativt til syklus 14, $Al(insol)_A$ og $MgZr$, ble også utført for å undersøke om forskjellen i den sykliske stabiliteten var forårsaket av forskjell i fordeling av elementene. Det ble funnet at ingen av sorbentene hadde en helt homogen fordeling av elementer. Dermed er det spekulert i at fordelingen av elementer bare er en av årsakene til forskjeller i den sykliske stabiliteten.

Sorbentene $Al(sol)Ce$, $Al(insol)Mg$ and $MgZr$ skilte seg ut ved å ha den høyeste sykliske stabiliteten fra syklus 14 til 69. The relative tapet i kapasitet for å fange opp CO_2 relativt til syklus 14 var 31.6 %, 25.0 % og 11.8 % i motsetning til sorbenten $Al(insol)_A$ som hadde et relativt tap i kapasitet på 50.0 %. Det var vanskelig å observere en sammenheng mellom Tammann temperatur og den sykliske stabiliteten blant disse tre sorbentene. Det var fordi sorbentene inneholdt ulike kombinasjoner av de fire stabiliserende fasene, og Tammann temperaturene til disse fasene ligger i et relativt snevert område på 1275-1483 °C, utenom $Ca_{12}Al_{14}O_{33}$ som har Tammann temperatur 744 °C.

Tapet av masse under det første fallet i den mekaniske falletesten viste at sorbenten $Al(sol)Ce$ hadde et eksepsjonelt høyt tap i masse på 19 % i motsetning til sorbentene $Al(insol)Mg$ og $MgZr$ som hadde et massetap på 2.9 % og 0.59 %. De absolutte kapasitetene for å fange CO_2 i syklusene 28, 42 og 68 ble sammenlignet for $Al(insol)Mg$ og $MgZr$. Verdiene stabiliserte seg ved 10 % for den førstnevnte sorbenten, mens verdiene stabiliserte seg ved 12 % for den sistnevnte sorbenten. Sorbenten $MgZr$ hadde dermed et kompromiss mellom de tre viktige faktorene stabilitet, evne til å fange opp CO_2 og massetap under den mekaniske falletesten. Denne sorbenten bestod av 2.8 vektprosent Mg og 1.9 vektprosent Zr , så dette ble funnet til å være den optimale sammensetningen av de testede sorbentene.

Table of Contents

Abstract	iii
Sammendrag	v
Table of Contents	ix
List of Tables	xii
List of Figures	xvii
List of symbols	xxiii
Abbreviations	xxiii
1 Introduction	1
1.1 Introduction	1
2 Moving Bed Carbonate-Looping (MBCL) Technology for Post-Combustion CO₂ capture	5
2.1 Moving Bed Carbonate-Looping (MBCL) Technology for Post-Combustion CO ₂ capture	5
3 Literature review	7
3.1 Deactivation of sorbents	7
3.2 Pelletization	7
3.3 Mechanical strength	8
3.4 Pre-calcination	8
3.5 Introduction of dopant to improve cyclic performance of calcined dolomite	8
3.6 Choice of precursor	10
3.7 Factors affecting sorbent performance	11
3.7.1 Dispersion of inert support, Tammann temperature and surface area	11

3.7.2	Pore volume	11
3.8	The impact of steam	12
4	Theory	13
4.1	Synthesis	13
4.1.1	Incipient wetness impregnation (IWI)	13
4.2	Characterisation	14
4.2.1	Thermogravimetric analysis (TGA)	14
4.2.2	N ₂ adsorption-desorption measurement	14
4.2.3	Mercury intrusion	19
4.2.4	Analysis methods based on x-rays and beams of electrons	19
5	Experimental procedure	23
5.1	Synthesis of sorbents	23
5.1.1	Preparation of raw material	23
5.1.2	Preparation of impregnation solutions	24
5.1.3	Incipient wetness impregnation	24
5.1.4	Granulation	24
5.1.5	Pre-calcination	25
5.2	Thermogravimetric Analysis (TGA)	25
5.3	Scanning electron microscope (SEM)	26
5.4	X-ray diffraction (XRD)	26
5.5	Falling test	26
5.6	N ₂ adsorption-desorption measurement	27
5.7	Mercury intrusion	27
5.8	Energy-dispersive x-ray spectrometry (EDS)	27
6	Results and discussion	29
6.1	Synthesis	29
6.2	Thermogravimetric Analysis (TGA)	31
6.3	Scanning electron microscope (SEM)	37
6.4	X-ray diffraction (XRD)	42
6.5	Falling test	45
6.6	N ₂ adsorption-desorption analysis and mercury intrusion	47
6.7	Energy-dispersive x-ray spectrometry (EDS)	54
7	Conclusion	65
8	Limitations of work	69
9	Recommendations	71
	Bibliography	73
A	Calculations	77
A.1	Amount of precursor needed for IWI	77
A.2	Nominal weight percent dopant in sorbent	78

A.3	CO ₂ capacity	79
A.3.1	CO ₂ capacity in interval one for Al(sol)Mg	81
A.3.2	Pre-calcination file for MgZr	82
A.4	Theoretical maximum CO ₂ capacity	82
A.5	Relative loss in CO ₂ capturing capacity	83
A.6	Porosity from N ₂ adsorption-desorption measurement	83
A.7	Total relative percentage weight loss during the falling test	85
B	Raw data	87
B.1	Synthesis of sorbents	87
B.2	Tammann temperature	87
B.3	Thermogravimetric analysis (TGA)	88
B.3.1	Al(sol)Mg	88
B.3.2	Al(insol)Mg	91
B.3.3	Al(sol)Ce	93
B.3.4	Al(insol)Ce	96
B.3.5	Al(insol) _A Zr	98
B.3.6	MgCe	100
B.3.7	MgZr	103
B.3.8	Ce	106
B.3.9	Al(insol) _B Zr	108
B.4	X-ray diffraction (XRD)	112
B.5	Mechanical test	118
B.6	N ₂ adsorption-desorption analysis	121
B.6.1	Specific surface area, pore volume, pore diameter and porosity	121
B.6.2	Pore size distribution plots	121
B.6.3	Adsorption isotherm	122
B.7	Energy-dispersive x-ray spectrometry	125
C	Other	129
C.1	Specialisation project	129
C.1.1	Synthesis of sorbents	129
C.1.2	Thermogravimetric analysis (TGA)	130

List of Tables

1	List of symbols.	xviii
5.1	The precursors, desired weight percent of dopants in the final sorbent, indicated as D wt% i , and a sample name for the sorbents are given below. The sample name is given on the form AB where A and B are the introduced element. Al(sol) and Al(insol) corresponds to the soluble precursor aluminium nitrate and the insoluble precursor cement, respectively. Two sorbents are labelled with the subscripts A and B since the difference between them are the weight percent aluminium from cement.	25
6.1	The precursors used, the desired and nominal weight percent dopants in the sorbents, denoted by D wt% i and N wt% i , respectively, and the sample name. The theoretical maximum capturing capacity is given as C_{\max}	30
6.2	C_1 , C_{14} , C_{28} , C_{42} and C_{68} of the sorbents. The loss in CO_2 capacity for cycle j relative to cycle i , $L_{i,j}$, is also presented.	33
6.3	Average particle diameter calculated based on 50 particles in SEM pictures. It was assumed that the particles are spherical.	41
6.4	The crystallite sizes (cs) of the crystalline phases.	45
6.5	Specific surface area, pore volume, average pore diameter and porosity of the sorbents.	48
B.1	The amount of precursors and distilled H_2O used for preparation of impregnation solutions, the total amount of impregnation solution used for impregnation and amount of distilled H_2O used for granulation.	87
B.2	The melting temperature, T_m , and Tammann temperature, T_T , of the stabilizing phases.	88
B.3	The crystallite size, given as cs_j for peak j , of CaO calculated from six peaks in the diffraction diagram.	117
B.4	The crystallite size, given as cs_j for peak j , of MgO calculated from four peaks in the diffraction diagram.	118

B.5	The crystallite size, given as cs_j for peak j , of CaZrO_3 calculated from four peaks in the diffraction diagram.	118
B.6	The crystallite size, given as cs_j for peak j , of CeO_2 calculated from four peaks in the diffraction diagram.	118
B.7	The mass of sorbent with size 250-500 μm used in each drop and the mass of residue with size $< 250 \mu\text{m}$	118
B.8	The mass of sorbent with size 500-850 μm used in each drop, the mass of residue with size $< 500 \mu\text{m}$	120
B.9	The result from two N_2 adsorption-desorption measurements. Single point surface area calculated when $p/p_0 = 0.20$, BJH desorption cumulative pore volume, BJH desorption average pore diameter and the porosity.	121
C.1	The precursors used, the desired weight percent dopant in the sorbent and the actual weight percent dopant in the sorbent, denoted by $D \text{ wt\% } i$ and $N \text{ wt\% } i$, respectively, and the defined sample name that is used as identification.	130
C.2	An overview of the CO_2 capacity of all the sorbents in C_1 , C_{38} , C_{60} and C_{122} . The loss in CO_2 capacity for cycle j relative to cycle i , $L_{i,j}$, is also presented.	130

List of Figures

1.1	Schematic diagram of Ca looping.	3
4.1	Adsorption isotherms. (a) Type I, (b) Type II, (c) Type III, (d) Type IV, (e) Type V, (f) Type VI. The figures are adapted based on existing images [1].	16
4.2	Hysteresis loops. (a) H1, (b) H2, (c) H3, (d) H4. The figures are adapted based on existing images [1].	17
4.3	(a) The relation between conversion and porosity of pellets. (b) The relation between crush strength and porosity of pellets. The pictures are adapted based on existing images [2].	19
6.1	The CO ₂ capacity plotted as a function of cycle number for the sorbents Al(sol)Mg, Al(insol)Mg, Al(sol)Ce and Al(insol)Ce.	32
6.2	The CO ₂ capacity plotted as a function of cycle number for the sorbents Al(insol) _A Zr, MgCe, MgZr, Ce and Al(insol) _B Zr.	32
6.3	The CO ₂ capacity of Al(sol)Mg and Al(sol)Ce in C ₁ , C ₁₄ , C ₂₈ , C ₄₂ and C ₆₈	34
6.4	The CO ₂ capacity of Al(insol)Mg, Al(insol)Ce, Al(insol) _A Zr and Al(insol) _B Zr in C ₁ , C ₁₄ , C ₂₈ , C ₄₂ and C ₆₈	34
6.5	The CO ₂ capacity of Al(sol)Mg, Al(insol)Mg, MgCe and MgZr in C ₁ , C ₁₄ , C ₂₈ , C ₄₂ and C ₆₈	35
6.6	The CO ₂ capacity of MgZr and Al(insol) _B Zr in C ₁ , C ₁₄ , C ₂₈ , C ₄₂ and C ₆₈	36
6.7	The CO ₂ capacity of Al(sol)Ce, Al(insol)Ce, MgCe and Ce in C ₁ , C ₁₄ , C ₂₈ , C ₄₂ and C ₆₈	37
6.8	SEM picture of fresh and spent Al(sol)Mg.	38
6.9	SEM picture of fresh and spent Al(insol)Mg.	38
6.10	SEM picture of fresh and spent Al(sol)Ce.	38
6.11	SEM picture of fresh and spent Al(insol)Ce.	39
6.12	SEM picture of fresh and spent Al(insol) _A Zr.	39
6.13	SEM picture of fresh and spent MgCe.	39
6.14	SEM picture of fresh and spent MgZr.	40
6.15	SEM picture of fresh and the spent sorbent Ce.	40

6.16	SEM picture of fresh and spent Al(insol) _B Zr.	40
6.17	Raw data from the CO ₂ capturing experiment performed in Linseis TGA for the sorbent Al(insol)Mg. The picture shows C ₁ to C ₁₇	42
6.18	Diffraction diagram of calcined dolomite, Al(sol)Mg and Al(insol)Mg. . .	43
6.19	Diffraction diagram of Al(sol)Ce, Al(insol)Ce and Al(insol) _A Zr.	44
6.20	Diffraction diagram of MgCe, MgZr, Ce and Al(insol) _B Zr.	44
6.21	The total relative percentage weight loss as a function of drops during the falling test.	46
6.22	C ₁ plotted against specific surface area.	49
6.23	C ₁ plotted against pore volume.	49
6.24	The weight loss in the first fall of the falling test plotted against porosity. .	50
6.25	Pore size distribution of calcined dolomite, Al(sol)Mg, Al(insol)Mg, Al(sol)Ce, Al(insol)Ce, MgCe, MgZr, Ce and Al(insol) _B Zr generated using the desorption branch.	51
6.26	Pore size distribution of Al(insol) _A Zr generated using the desorption branch.	51
6.27	The pore size distribution of calcined dolomite and the fresh sorbents Al(insol)Ce and Al(insol) _A Zr from the mercury intrusion measurement. . .	52
6.28	The adsorption isotherms for calcined dolomite, Al(sol)Mg and Ce from the N ₂ adsorption-desorption measurement.	53
6.29	Elemental mapping of calcined dolomite. The first picture shows an overview of the area, while the second, third and fourth picture show an elemental mapping of Ca, Mg and O, respectively.	55
6.30	Elemental mapping of Fondu cement. The first picture shows an overview of the area, while the second, third, fourth, fifth and sixth picture show an elemental mapping of Ca, O, Al, Fe and Si, respectively.	56
6.31	Elemental mapping of fresh Al(sol)Mg.	58
6.32	Elemental mapping of fresh Al(insol)Mg.	59
6.33	Elemental mapping of fresh Al(insol)Zr.	61
6.34	Elemental mapping of fresh MgZr.	62
A.1	The top image shows the calcination file for Al(insol)Mg where the points m ₁ and m ₂ are included as an example for calculation of $\sum_M^k m_{MO}$. The bottom image shows the cyclic CO ₂ capture and regeneration of Al(insol)Mg where the points m _{T,i} and m _{B,i} are included as an example for calculation of m _{CO₂,i}	81
B.1	Raw data, without correction, from calcination of the sorbent Al(sol)Mg in Linseis TGA.	88
B.2	Raw data, without correction, from the CO ₂ capturing experiment performed in Linseis TGA for the sorbent Al(sol)Mg. The picture shows C ₁ to C ₁₇	89
B.3	The correction curve used for all measurements of cyclic CO ₂ capture and regeneration. The values in this correction curve was used together with values from Figure B.2 to find corrected values for C ₁ to C ₁₇	89
B.4	Raw data from the CO ₂ capturing experiment performed in Linseis TGA for the sorbent Al(sol)Mg. The picture shows C ₁₈ to C ₃₄	90

B.5	Raw data from the CO ₂ capturing experiment performed in Linseis TGA for the sorbent Al(sol)Mg. The picture shows C ₃₅ to C ₅₁	90
B.6	Raw data from the CO ₂ capturing experiment performed in Linseis TGA for the sorbent Al(sol)Mg. The picture shows C ₅₂ to C ₆₈	91
B.7	Raw data, without correction, from calcination of the sorbent Al(insol)Mg in Linseis TGA.	91
B.8	Raw data from the CO ₂ capturing experiment performed in Linseis TGA for the sorbent Al(insol)Mg. The picture shows C ₁ to C ₁₇	92
B.9	Raw data from the CO ₂ capturing experiment performed in Linseis TGA for the sorbent Al(insol)Mg. The picture shows C ₁₈ to C ₃₄	92
B.10	Raw data from the CO ₂ capturing experiment performed in Linseis TGA for the sorbent Al(insol)Mg. The picture shows C ₃₅ to C ₅₁	93
B.11	Raw data from the CO ₂ capturing experiment performed in Linseis TGA for the sorbent Al(insol)Mg. The picture shows C ₅₂ to C ₆₈	93
B.12	Raw data, without correction from calcination of the sorbent Al(sol)Ce in Linseis TGA.	94
B.13	Raw data from the CO ₂ capturing experiment performed in Linseis TGA for the sorbent Al(sol)Ce. The picture shows C ₁ to C ₁₇	94
B.14	Raw data from the CO ₂ capturing experiment performed in Linseis TGA for the sorbent Al(sol)Ce. The picture shows C ₁₈ to C ₃₄	95
B.15	Raw data from the CO ₂ capturing experiment performed in Linseis TGA for the sorbent Al(sol)Ce. The picture shows C ₃₅ to C ₅₁	95
B.16	Raw data from the CO ₂ capturing experiment performed in Linseis TGA for the sorbent Al(sol)Ce. The picture shows C ₅₂ to C ₆₈	96
B.17	Raw data, without correction, from calcination of the sorbent Al(insol)Ce in Linseis TGA.	96
B.18	Raw data from the CO ₂ capturing experiment performed in Linseis TGA for the sorbent Al(insol)Ce. The picture shows C ₁ to C ₁₇	97
B.19	Raw data from the CO ₂ capturing experiment performed in Linseis TGA for the sorbent Al(insol)Ce. The picture shows C ₁₈ to C ₃₄	97
B.20	Raw data from the CO ₂ capturing experiment performed in Linseis TGA for the sorbent Al(insol)Ce. The picture shows C ₃₅ to C ₅₁	98
B.21	Raw data, without correction, from calcination of the sorbent Al(insol) _A Zr in Linseis TGA.	98
B.22	Raw data from the CO ₂ capturing experiment performed in Linseis TGA for the sorbent Al(insol) _A Zr. The picture shows C ₁ to C ₁₇	99
B.23	Raw data from the CO ₂ capturing experiment performed in Linseis TGA for the sorbent Al(insol) _A Zr. The picture shows C ₁₈ to C ₃₄	99
B.24	Raw data from the CO ₂ capturing experiment performed in Linseis TGA for the sorbent Al(insol) _A Zr. The picture shows C ₃₅ to C ₅₁	100
B.25	Raw data from the CO ₂ capturing experiment performed in Linseis TGA for the sorbent Al(insol) _A Zr. The picture shows C ₅₂ to C ₆₈	100
B.26	Raw data, without correction, from calcination of the sorbent MgCe in Linseis TGA.	101

B.27	Raw data from the CO ₂ capturing experiment performed in Linseis TGA for the sorbent MgCe. The picture shows C ₁ to C ₁₇	101
B.28	Raw data from the CO ₂ capturing experiment performed in Linseis TGA for the sorbent MgCe. The picture shows C ₁₈ to C ₃₄	102
B.29	Raw data from the CO ₂ capturing experiment performed in Linseis TGA for the sorbent MgCe. The picture shows C ₃₅ to C ₅₁	102
B.30	Raw data from the CO ₂ capturing experiment performed in Linseis TGA for the sorbent MgCe. The picture shows C ₅₂ to C ₆₈	103
B.31	Raw data, without correction, from calcination of the sorbent MgZr in Linseis TGA.	103
B.32	Raw data from the CO ₂ capturing experiment performed in Linseis TGA for the sorbent MgZr. The picture shows C ₁ to C ₁₇	104
B.33	Raw data from the CO ₂ capturing experiment performed in Linseis TGA for the sorbent MgZr. The picture shows C ₁₈ to C ₃₄	104
B.34	Raw data from the CO ₂ capturing experiment performed in Linseis TGA for the sorbent MgZr. The picture shows C ₃₅ to C ₅₁	105
B.35	Raw data from the CO ₂ capturing experiment performed in Linseis TGA for the sorbent MgZr. The picture shows C ₅₂ to C ₆₃	105
B.36	Raw data from the CO ₂ capturing experiment performed in Linseis TGA for the sorbent MgZr. The picture shows C ₆₄ to C ₆₈	106
B.37	Raw data, without correction, from calcination of the sorbent Ce in Linseis TGA.	106
B.38	Raw data from the CO ₂ capturing experiment performed in Linseis TGA for the sorbent Ce. The picture shows C ₁ to C ₁₇	107
B.39	Raw data from the CO ₂ capturing experiment performed in Linseis TGA for the sorbent Ce. The picture shows C ₁₈ to C ₃₄	107
B.40	Raw data from the CO ₂ capturing experiment performed in Linseis TGA for the sorbent Ce. The picture shows C ₃₅ to C ₅₁	108
B.41	Raw data from the CO ₂ capturing experiment performed in Linseis TGA for the sorbent Ce. The picture shows C ₅₂ to C ₆₈	108
B.42	Raw data, without correction, from calcination of the sorbent Al(insol) _B Zr in Linseis TGA.	109
B.43	Raw data from the CO ₂ capturing experiment performed in Linseis TGA for the sorbent Al(insol) _B Zr. The picture shows C ₁ to C ₁₇	109
B.44	Raw data from the CO ₂ capturing experiment performed in Linseis TGA for the sorbent Al(insol) _B Zr. The picture shows C ₁₈ to C ₂₈	110
B.45	Raw data from the CO ₂ capturing experiment performed in Linseis TGA for the sorbent Al(insol) _B Zr. The picture shows C ₂₉ to C ₃₄	110
B.46	Raw data from the CO ₂ capturing experiment performed in Linseis TGA for the sorbent Al(insol) _B Zr. The picture shows C ₃₅ to C ₄₀	111
B.47	Raw data from the CO ₂ capturing experiment performed in Linseis TGA for the sorbent Al(insol) _B Zr. The picture shows C ₄₀ to C ₅₁	111
B.48	Raw data from the CO ₂ capturing experiment performed in Linseis TGA for the sorbent Al(insol) _B Zr. The picture shows C ₅₂ to C ₆₈	112
B.49	Diffraction diagram of calcined dolomite.	112

B.50	Diffraction diagram of Al(sol)Mg.	113
B.51	Diffraction diagram of Al(insol)Mg.	113
B.52	Diffraction diagram of Al(sol)Ce.	114
B.53	Diffraction diagram of Al(insol)Ce.	114
B.54	Diffraction diagram of Al(insol) _A Zr.	115
B.55	Diffraction diagram of MgCe.	115
B.56	Diffraction diagram of MgZr.	116
B.57	Diffraction diagram of the sorbent Ce.	116
B.58	Diffraction diagram of Al(insol) _B Zr.	117
B.59	Pore size distribution of Al(sol)Mg, Al(insol)Mg, Al(sol)Ce, Al(insol)Ce, Al(insol) _A Zr, MgCe and MgZr generated using the desorption branch.	122
B.60	Pore size distribution of calcined dolomite, Ce and Al(insol) _B Zr generated using the desorption branch.	122
B.61	The adsorption isotherms for Al(sol)Mg from two N ₂ adsorption-desorption measurements.	123
B.62	The adsorption isotherms for Al(insol)Mg from two N ₂ adsorption-desorption measurements.	123
B.63	The adsorption isotherms for Al(sol)Ce from two N ₂ adsorption-desorption measurements.	123
B.64	The adsorption isotherms for Al(insol)Ce from two N ₂ adsorption-desorption measurements.	124
B.65	The adsorption isotherms for Al(insol) _A Zr from two N ₂ adsorption-desorption measurements.	124
B.66	The adsorption isotherms for MgCe from two N ₂ adsorption-desorption measurements.	124
B.67	The adsorption isotherms for MgZr from two N ₂ adsorption-desorption measurements.	125
B.68	The adsorption isotherms for the sorbent Ce from two N ₂ adsorption-desorption measurements.	125
B.69	The adsorption isotherms for Al(insol) _B Zr from two N ₂ adsorption-desorption measurements.	125
B.70	EDS pictures of the Fondu cement and calcined dolomite.	126
B.71	SEM pictures giving an overview of the area analyzed by EDS for Al(sol)Mg.	126
B.72	EDS pictures of Al(sol)Mg.	126
B.73	SEM pictures giving an overview of the area analyzed by EDS for Al(insol)Mg.	127
B.74	EDS pictures of Al(insol)Zr.	127
B.75	SEM pictures giving an overview of the area analyzed by EDS for Al(insol) _A Zr.	127
B.76	EDS pictures of Al(insol) _A Zr.	128
B.77	SEM pictures giving an overview of the area analyzed by EDS for MgZr.	128
B.78	EDS pictures of MgZr.	128

List of symbols

Table 1: List of symbols.

Symbol	Unit	Description
A	m ²	The total area
A ₀	m ² /Molecule	The area each molecule covers on the surface
C	g CO ₂ /g sorbent	The CO ₂ capacity
C	-	The BET constant
C _i	g CO ₂ /g sorbent	The CO ₂ capacity in cycle <i>i</i>
C _{max}	%	The theoretical maximum CO ₂ capacity
cs _i	nm	The crystallite size of compound <i>i</i>
cs _j	nm	The crystallite size for peak <i>j</i>
d	m	The distance between two lattice planes
d _{fresh}	nm	The average particle diameter of fresh sorbents
d _p	nm	The pore diameter
d _{spent}	nm	The average particle diameter of spent sorbents
K	-	A constant
L	m	The crystallite size
L _{i,j}	%	Loss in CO ₂ capacity of the sorbent after j cycles relative to cycle <i>i</i>
M _{CO₂}	g/mol	The molecular weight of CO ₂
M _i	g/mol	Molecular weight of element <i>i</i>
M _{i,precursor}	g/mol	Molecular weight of the precursor for element <i>i</i>
M _{MO}	g/mol	Molecular weight of the oxide MO
M _{N₂}	g/mol	The molecular mass of N ₂
m _{B,i}	g	The mass of the sorbent at complete regeneration in cycle <i>i</i>
m _{B,i,correction}	g	The mass at complete regeneration in cycle <i>i</i> in the correction file
m _{B,i,raw}	g	The mass at complete regeneration in cycle <i>i</i> in the correction file
m _{B,1}	g	The mass of sorbent at complete regeneration in C ₁
m _{calcined dolomite}	m	Mass of calcined dolomite
m _{CO₂}	g	The mass of captured CO ₂
m _{CO₂,i}	g	The mass of captured CO ₂ in cycle <i>i</i>
m _{CO₂,max}	g	The theoretical maximum mass of CO ₂ the sorbent can capture
m _{H₂O}	g	Weight of H ₂ O added to the precursors

$m_{H_2O,granulation}$	g	The mass of water used during granulation
$m_{H_2O,impregsol}$	g	The mass of water used to prepare the impregnation solutions
m_i	g	Mass of element i in the sorbent
$m_{impregsol,used}$	g	The mass of the impregnation solution used under impregnation of calcined dolomite
$m_{IS+beaker,tot}$	g	Total weight of the impregnation solution and the beaker
$m_{IS,tot}$	g	Total weight of the impregnation solution
$m_{IS,used}$	g	Amount of impregnation solution used for the impregnation
$m_{MO,sorbent}$	g	Mass of oxide MO formed in sorbent
$m_{N_2(l)}$	g	The mass of $N_2(l)$ in the pores
$m_{precursor,i}$	g	Mass of the precursor for element i
$m_{precursor\ i}$	g	The mass of precursor i used during synthesis
$m_{precursor,i,sorbent}$	g	Mass of precursor introduced into dolomite through impregnation
$m_{prior\ to\ cal}$	g	The mass of the sorbent loaded into the TGA prior to calcination
$m_{remains\ of\ IS+beaker,tot}$	g	Weight of the remains of impregnation solution and the beaker
$m_{res<250\mu m,5}$	g	The mass of residue produced when dropping $m_{250-500\mu m,5}$ down the tube
$m_{res<500\mu m,5}$	g	The mass of residue produced when dropping $m_{500-850\mu m,5}$ down the tube
$m_{sorbent\ after\ cal}$	g	The mass of sorbent after the pre-calcination procedure
$m_{T,i}$	g	The mass of the sorbent at maximum CO_2 sorption in cycle i
$m_{T,i,correction}$	g	The mass at maximum CO_2 capture in cycle i in the correction file
$m_{T,i,raw}$	g	The mass at maximum CO_2 capture in cycle i in the raw file
$m_{tot,i}$	g	The total mass of sorbents being dropped down the tube in drop i
m_1	g	The initial mass of sorbent prior to calcination recorded by the TGA
m_2	g	The mass of completely calcined sorbent recorded by the TGA
$m_{250-500\mu m,i}$	g	The mass of sorbents with size 250-500 μm
$m_{500-850\mu m,i}$	g	The mass of sorbents with size 500-850 μm
N_A	Molecules/mol	Avogadro constant
N_0	Molecules	The number of molecules adsorbed on the surface

n	-	An integer
$n_{\text{calcined dolomite}}$	mol	The molar amount of calcined dolomite
n_{CaO}	mol	The molar amount of CaO in the sorbents
n_i	mol	Molar amount of element i in the sorbent
$n_{i,\text{precursor}}$	mol	Molar amount of the precursor of element i in the sorbent
$n_{i,\text{sorbent}}$	mol	Molar amount of element i in dolomite as a result of impregnation
$n_{\text{MO,sorbent}}$	mol	Molar amount of MO formed in calcined dolomite
$n_{\text{N}_2,\text{ads}}$	mol	The number of moles N_2 adsorbed
n_{N_2}	mol	The number of moles $\text{N}_2(\text{l})$ filling the pores
$n_{\text{precursor},i,\text{sorbent}}$	mol	Molar amount of precursor introduced into dolomite through impregnation
p	Pa	Pressure of adsorbed gas (BET)
p_0	Pa	Saturation pressure of adsorbed gas (BET)
R	J/K mol	The universal gas constant
r_k	m	The Kelvin radius
r_p	m	The pore radius
SA	m^2/g	Specific surface area
T	K	The temperature
T_m	$^\circ\text{C}$	The melting temperature
T_T	$^\circ\text{C}$	The Tammann temperature
t	m	The thickness of the layer of adsorbed N_2 present prior to condensation
V	m^3	Volume of gas adsorbed (BET)
V_{liq}	m^3/mol	The molar volume of N_2
V_m	m^3	Volume of gas adsorbed at monolayer adsorption (BET)
V_{N_2}	m^3	The volume of $\text{N}_2(\text{l})$ filling the pores
V_p	m^3	The pore volume
V_s	m^3	The volume of compact solid
V_t	m^3	The total volume of the porous material
x_i	-	The mole fraction of compound i in calcined dolomite
α	-	Stoichiometric coefficient
β	m	The width of the diffraction peak
β	-	The purity of the precursor
γ	N/m	The surface tension
θ	%	The porosity
θ	$^\circ$	The contact angle
θ	$^\circ$	The angle between the incoming x-rays and the lattice plane
λ	m	The wavelength of x-rays

ρ_i	kg/m ³	The density of compound <i>i</i>
ρ_{N_2}	kg/m ³	The density of N ₂
ρ_{sorbent}	kg/m ³	The density of the sorbent
$\sum_i^N m_i$	g	The total mass of calcined dolomite
$\sum_M^k m_{MO}$	g	The total mass of sorbent consisting of the metal oxides MO
$\sum_k^N m_{MO, \text{sorbent}, k}$	g	The sum over mass of oxide k, ..., N present in the sample
$\sum_M^k n_{CaMO}$	g	The molar amount of CaO-capturing inert phases
v_{ads}	cm ³ /g STP	The quantity adsorbed N ₂ (g)
ω_i	-	Fractional weight percent of element <i>i</i> in the sorbent
ω_j	-	Fractional weight percent of element <i>i</i> in the sorbent
$\omega_{i, \text{sorbent}}$	-	Correct weight percent dopant in the sorbent
$\omega_{\text{precursor}, i, IS}$	-	Weight percent of the precursor for element <i>i</i> in the impregnation solution

Abbreviations

IS	=	Impregnation solution
XRD	=	X-ray diffraction
TGA	=	Thermogravimetric analysis
BET	=	Brunauer-Emmett-Teller
SEM	=	Scanning electron microscopy
IWI	=	Incipient wetness impregnation
EDS	=	Energy-dispersive x-ray spectrometry
TEM	=	Transmission electron microscopy
GHG	=	Green house gas
CCS	=	Carbon capture and storage
MEA	=	Monoethanolamine

LIST OF FIGURES

Introduction

1.1 Introduction

People's way of living have changed significantly during the last hundred years. This development can be attributed to the discovery and exploitation of the fossil fuels oil, coal and natural gas. Fossil fuels were first utilized in industrial applications during the mid 19th century, and the use have increased rapidly ever since [3]. However, the many benefits originating from utilization of petroleum are accompanied by severe downsides as well. Combustion of fossil fuels leads to emission of green house gases (GHGs). CO_2 , CH_4 , N_2O and fluorinated gases are considered the main GHGs, of which CO_2 is of greatest importance [4, 5].

As the emission of GHGs has escalated, the global average temperature is $0.8\text{ }^\circ\text{C}$ higher than it was at the late 1800s, and this temperature increase is related to the increased concentrations of GHGs in the atmosphere [6]. The release of GHGs into the atmosphere has never been higher, and will proceed if no countermeasurements are implemented [4]. The main goal of United Nations Framework Convention on Climate Change, which was signed by 195 countries in 1992, is to decelerate the global increase of temperature and keep it below $2\text{ }^\circ\text{C}$, preferably less than $1.5\text{ }^\circ\text{C}$, relative to pre-industrial time. The Intergovernmental Panel on Climate Change (IPCC) has stated that the global release of GHGs must be brought down with 40-70 % during the time period 2012-2050 in order to succeed. Considering that 81 % of the world's energy consumption in 2016 was derived from petroleum, the center of interest must be shifted towards renewable energy sources, and coupling the production and use of energy with Carbon Capture and Storage technology (CCS) [7, 4].

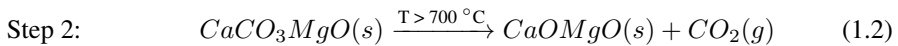
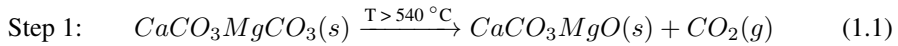
The capture, transportation and indefinite storage of CO_2 arising from petroleum and biomass is called CCS [8, 9]. CCS can be put into practice as pre-combustion CO_2 capture, post-combustion CO_2 capture or as an oxyfuel process, but the merging of an existing

plant and CCS is least complicated when choosing post-combustion CO₂ capture [8, 10]. The state of the art technology for post-combustion CO₂ capture is chemical absorption using amines as an absorptive solvent. CO₂ becomes captured by reaction with the absorptive solvent, which often is the primary amine monoethanolamine (MEA), and the solvent is then regenerated for further capture [10].

Chemical absorption using MEA is the current state of the art technology since it has highest capturing efficiency, selectivity and is the most energetically and economically feasible alternative when comparing the available post-combustion CO₂ removal technologies [8]. The solvent MEA is a cheaper alternative and this CO₂ capturing technology is well developed [11, 10]. Disadvantages of this technology is degeneration of the solvent when it comes in contact with SO₂ and O₂, which may be present in the flue gas, corrosion of equipment and high costs because of the high energy demand for restoring and regenerating the amine [8].

Because there are some downsides with this technology, research is being performed to explore if solid sorbents is a viable substitute [12]. Solid sorbents constitute a wide group of compounds that can be used for CO₂ capturing purposes [13]. Four main groups are physisorbents, chemisorbents, organic sorbents and organic-inorganic sorbents. The sorbent CaO, which belongs to the group of chemisorbents, has appealing qualities such as high theoretical maximum capturing capacity. Naturally occurring sources of CaO exist which are both abundant and cheap and the environmental consequences of utilization of CaO-based sorbents are small [14, 13]. Naturally occurring resources of CaO are dolomite (CaMg(CO₃)₂) and limestone (CaCO₃) [15, 16]. These raw materials are transformed to the CO₂ capturing material through the thermal processing step calcination [14]. Dolomite is transformed to CaOMgO, while limestone is transformed to CaO.

Calcination of dolomite takes place through the following two steps [14, 13],



CaO captures CO₂ by this reaction [17],



This sorption reaction is exothermic which means that the CO₂ removal takes place at lower temperatures compared to the regeneration. In compliance with Le Chateliers principle a high partial pressure of CO₂ is favourable for the capture [12]. The capacity for sorbents to capture CO₂ according to reaction 1.3 is defined as,

$$C = \frac{m_{CO_2}}{\sum_M^k m_{MO}} \quad (1.4)$$

°C, as seen in reaction 1.5, MgO is an inert compound in calcined dolomite with regards to CO₂ capture.

A crucial and well-known disadvantage with the use of CaO-based sorbents for CO₂ removal is a noteworthy decrease in capturing capacity during the initial cycles [14, 13]. A sorbent with high capturing capacity is desirable, but the aim is also a sorbent with stability over several carbonation-calcination cycles. Also, a sorbent able to maintain a capturing capacity at approximately the same level for several cycles is normally preferred over a sorbent with high starting capacity [2]. The deactivation mechanism in CaO-based sorbents is attributed to sintering [21]. The theoretical maximum CO₂ capturing capacity of calcined limestone is significantly higher than for calcined dolomite. Despite that, dolomite may be a better choice as CaO-source. Calcined dolomite has proven to withstand sintering more effectively than calcined limestone, and this high-quality property is attributed to the presence of naturally occurring MgO in calcined dolomite [14].

Due to the mentioned disadvantage, the goal of this work is to synthesize high-temperature solid CaO-based sorbents for CO₂ capture by incorporation of dopants in calcined dolomite, and to determine the optimal sorbent composition that leads to the highest stability over several carbonation-calcination cycles.

Moving Bed Carbonate-Looping (MBCL) Technology for Post-Combustion CO₂ capture

2.1 Moving Bed Carbonate-Looping (MBCL) Technology for Post-Combustion CO₂ capture

This thesis is written in collaboration with Gassnova for their project Moving Bed Carbonate-Looping (MBCL) Technology for Post-Combustion CO₂ capture, and therefore, some aspects of the laboratory work was determined as a result of this collaboration. The project investigates the possibility of using CO₂ capturing sorbents in post combustion CO₂ removal in a natural gas combined cycle power plant. The part of the project relevant for this thesis consists of a moving bed carbonator and a moving bed calciner. CaO enables CO₂ removal from a combustion exhaust gas by transformation to CaCO₃, and the solid sorbents are then transported to the calciner. The calciner is operated at a higher temperature, and thereby regenerating the sorbents.

Dolomite was chosen as the raw material due to high theoretical capturing capacity, the presence of MgCO₃ which helps stabilize sorbents against sintering when transformed to MgO, high abundance in nature and low cost. However, due to the well-known decrease in capacity during the first carbonation-calcination cycles, dolomite will be modified by introducing metal oxides where the aim is to make the solid sorbent more resistant to sintering. Incipient wetness impregnation has been chosen as the synthesis technique, and the elements Mg, Zr, Al and Ce is being introduced to form an oxide form to assure better structural stabilization. The sorbents will be in the form of granules with a diameter of 500 μm . Carbonation and calcination is run at 570 °C with 10 % CO₂ and 8 % steam balanced

by Ar and 950 °C with 100 % CO₂, respectively.

Literature review

3.1 Deactivation of sorbents

It is reported in literature that the cause for deactivation of CaO-based sorbents is sintering which results in pore blockage [14, 22, 23]. Sintering occurs when exposing the sorbent to high temperatures, usually $T > 500\text{ }^{\circ}\text{C}$, which leads to growth of crystals and more compact packing of the active material due to pore collapse [2, 23]. The rate of sintering and operation temperature are exponentially related [2]. As a result of sintering, the surface area of the sorbent shrinks. Since sintering affects both the capturing capacity of sorbents and the surface area, the CO_2 sorption reaction is structure sensitive [2]. The typical temperature range in carbonation-calcination cycles is $640\text{-}900\text{ }^{\circ}\text{C}$, as mentioned in section 1.1, so sintering has the strongest effect during calcination. The Tammann temperature of a compound marks the upper temperature limit for when the effect of sintering becomes noteworthy [24]. This temperature is roughly 0.52 times the melting temperature of the compound. Other factors influencing the rate of sintering are atmosphere, type and dispersion of metal, promoters, contamination, surface area and porosity [2]. Inclusion of steam in the atmosphere also magnifies the rate of sintering. Reestablishing the original material after sintering is difficult, therefore it is desirable to counteract the deactivation instead.

3.2 Pelletization

The application of solid sorbents in industrial reactors sets requirements for the shape and size of the sorbent [25]. Using sorbents in the form of fine powders leads to practical problems such as pressure drops and challenges related to the transportation of the sorbent through the reactor [25, 26, 27]. To overcome these challenges, the sorbent can be developed into larger pellets.

3.3 Mechanical strength

Pellets used in catalytic industrial reactors need to have sufficient mechanical strength in order to withstand the mechanical stress the pellets experience during operation of the reactor [2, 19]. Mechanical strength is measured as crushing strength of the pellet and tolerance for attrition [2]. The crushing strength of a pellet is defined as the force required to deform the radial or axial axis of the pellet, while the tolerance for attrition is defined as the reduction in mass of the pellet per time as a result of formation of fine powder. For the reactor system presented in Figure 1.1, pellets would also be exposed to a series of carbonation-calcination cycles with temperature alternation from around 640 °C to above 900 °C, and thus, thermal stress [19].

Several different methods for exploring mechanical strength of a material exist [2, 27, 19]. A straightforward way of obtaining a rough overview of the strength of pellets is to drop pellets down a vertical tube with a height of one meter [19]. This gives an understanding of the possible outcome of collision between pellets and the reactor.

3.4 Pre-calcination

Calcination is a thermal processing step which enables reactions due to exposure to high temperatures [14]. Calcination is used to transform carbonates in dolomite to its oxide form, and is also often the last synthesis step of an oxide catalyst due to the requirement of decomposition and evaporation of precursor compounds [2]. The material must be free from moisture prior to calcination, and a modest temperature ramping is required to steer clear of rupture of the material due to elevated steam pressure in micropores. This thermal treatment should be carried out in a non-reactive atmosphere if the precursor contains nitrates or amines.

For the synthesis of CaO-based sorbents for CO₂ capture, pre-calcination has yet another function. It has been reported that thermal pre-treatment of sorbents may be a supplemental procedure to improve sorbent performance in addition to incorporation of metal oxides [23, 28]. This is explained by a proposed pore-skeleton model. As pre-calcination is carried out prior to the carbonation-calcination cycling, sintering is intentionally triggered. The result is a sorbent more resistant towards sintering due to formation of a solid framework of particles which helps maintain the structural arrangement of particles.

3.5 Introduction of dopant to improve cyclic performance of calcined dolomite

Several different processing steps and treatments of dolomite have been carried out in an attempt to maintain a high CO₂ capturing capacity over several carbonation-calcination cycles. The positive impact of naturally occurring MgO in calcined dolomite has been

noticed, so one approach is the incorporation of metal oxides with the intention to create an improved structural support that can withstand sintering to a larger degree [23]. Literature describes various approaches for incorporation of metal oxides in CaO-based sorbents for CO₂ sorption. It has been conducted research on natural sources for CaO (limestone, dolomite) [17, 19, 22, 29] and synthetic CaO-sources (calcium acetate) [30, 31, 32]. Different metal precursors have been utilized, and different synthesis techniques have been applied (incipient wetness impregnation, wet mixing, spray drying) [31, 17, 19, 22, 29]. These factors matter for the theoretical maximum capturing capacity and the formation of an inert stabilizing phase, and hence, the performance of the sorbent [30, 29, 32]. The following paragraphs give an overview of research performed regarding the dopants Zr, Al and Ce.

Bjørnar Arstad et al. (2013) have synthesized sorbents using dolomite as the raw material and Zr and Al as dopants [22]. Calcined dolomite was used as reference. Calcined dolomite was doped with the soluble precursors zirconium dioxide (ZrO₂) and aluminium oxide (Al₂O₃) using incipient wetness impregnation, followed by another calcination step. The final weight percent of the dopants in the sorbents were 10 %. A cyclic stability test was performed running the carbonation at 600 °C for 120 min in an atmosphere of 9.15 % CO₂ balanced with N₂. Calcination took place at 850 °C in 100 % N₂. The carbonation-calcination cycling showed that the reference sorbent calcined dolomite had the highest overall capacity, but also the steepest decline in capacity during the first cycles. The Zr-containing sorbent had the third highest starting capacity, but managed to preserve a higher capacity for the remaining cycles compared to the other modified sorbent. The Al-containing sorbent had the second highest starting capacity, but also had the highest initial loss of capacity of the modified sorbents. XRD revealed that the modified sorbents had formed stabilizing phases during synthesis, and CaZrO₃ and CaAl₂O₄ were detected.

Bjørnar Arstad et al. (2014) have performed a follow-up study and continued the study of Zr-stabilized sorbents [17]. Dolomite was calcined at 900 °C for 12 hours and then doped with the liquid precursor zirconium nitrate (ZrN₂O₇) using incipient wetness impregnation. The sorbents were calcined at 900 °C for 15 hours. The final weight percent Zr in the sorbents were 0.5 wt%, 1 wt%, 5 wt% and 10 wt%. The sorbents were calcined at 900 °C for 15 hours. The CO₂ capacity and cyclic stability of the sorbents were tested in TGA during 60 cycles. First, the sorbents were calcined in TGA at 900 °C for 3 hours in 100 % N₂. Then carbonation was run at 600 °C for 20 minutes in 10 vol% CO₂ and 1 vol% steam balanced with N₂, and calcination took place at 900 °C for 30 minutes in 100 % N₂. The carbonation-calcination cycling revealed that different loadings of Zr affected the capturing performance. Sorbents with 5 wt% and 10 wt% Zr had insufficient performance, and they suspected that it was due to pore blocking. The 0.5 wt% sorbent had a capacity of 33 % and 22 % in the first and last cycle, respectively, while the 1 wt% sorbent had a capacity of 21 % and 19 wt% in the first and last cycle, respectively. Thus, the former had an overall higher capturing capacity and less cyclic stability than the 1 wt% sorbent. XRD identified CaZrO₃ as the stabilizing phase.

Another study synthesized pellets using wet mixing as the synthesis technique, limestone as the raw material and cement as the precursor [19]. The pellets contained 10 % cement, and were tested in 35 carbonation-calcination cycles in the TGA. The carbonation was run

at 750 °C with 15 % CO₂ balanced by N₂ and calcination took place at 850 °C with 100 % N₂. The experiment showed that the pellets had a capturing capacity of 40 % and 37 % in the first and last cycle, respectively. XRD revealed that Ca₁₂Al₁₄O₃₃ was formed as the stabilizing phase.

In a doctoral thesis the synthesis of sorbents based on synthetic CaO was performed, with the incorporation of an inert supporting phase [31]. The calcium source and precursors used was calcium acetate (C₄H₆O₄Ca), cerium nitrate (Ce(NO₃)₃·6H₂O), zirconium nitrate, magnesium nitrate (Mg(NO₃)₂·6H₂O) and aluminium nitrate (Al(NO₃)₃·9H₂O). Sorbents with only one additive (Ce, Zr and Al in separate sorbents) and with two additives (Ce coupled with Zr, and Al coupled with Mg) were synthesized with different molar ratios of metal oxides. The CO₂ capturing capacity and cyclic stability were investigated using TGA. The cyclic experiment showed that sorbents with one additive (Ce and Zr) had a capturing capacity close to theoretical maximum and complete stability over 20 cycles. The capacities lie in the range 45-55 % and 40-56 %, respectively. The stabilizing phase was CeO₂ and CaZrO₃, respectively. Three sorbents contained both Ce and Zr, where the difference was different amounts of additives, and these sorbents had an initial capacity close to theoretical maximum and 20 %, 4 % and 0 % loss in capacity over 20 cycles. The sorbent containing only Al had quite low capturing capacity, below half of the theoretical maximum during all cycles and also a 20 % loss in capacity over 20 cycles. Coupling Al with Mg lead to increased overall capacity, but lower stability from cycle 1 to cycle 20.

3.6 Choice of precursor

H.R. Radfarnia, M.C. Iliuta have synthesised sorbents based on limestone which were doped with Al, Zr, Mg and Y [29]. The precursors used were aluminium nitrate, zirconium nitrate, magnesium acetate tetrahydrate (C₄H₆O₄Mg·4H₂O), zirconium hydroxide (Zr(OH)₄), aluminium oxide, aluminium acetate (Al(OH)(C₂H₃O₂)₂) and yttrium oxide (Y₂O₃), where the first three are soluble precursors and the last four are insoluble precursors. The synthesis technique used was wet mixing. The CO₂ capacity and cyclic stability over 25 cycles were investigated using TGA. Carbonation was run at 650 °C for 30 minutes in an atmosphere of 15 % CO₂ balanced with Ar. Two different experimental conditions were used for the calcination, termed mild and severe. Calcination was conducted at 750 °C for 30 minutes in 100 % Ar and 930 °C for 10 minutes in 50 vol% CO₂ and 50 vol% Ar, respectively.

During the TGA experiment using mild calcination conditions, it was found that sorbents based on insoluble precursors had a lower sorption of CO₂ over several cycles compared to the other sorbents, except use of the insoluble precursor aluminium acetate which had stabilizing phase Ca₉Al₆O₁₈ [29]. It was suspected that this was due to the difficulty of incorporating the inert phase uniformly among CaO-particles when the precursor was insoluble. It was found that the sorbents with precursors zirconium nitrate and aluminium nitrate with a molar ratio of 0.1 between dopant and Ca had the best performance under mild conditions, both sorbents were able to carry 0.29 g CO₂/g sorbent at cycle 25. The sorbents with best performance under mild conditions were also tested under severe con-

ditions. Of the tested sorbents, the sorbent synthesized using soluble zirconium nitrate and insoluble aluminium acetate, both with a molar ratio of 0.1 between dopant and Ca, had the highest and second highest CO₂ sorption in the last cycle, respectively. However, the cost of these synthesised sorbents must be taken into account. It is desirable with a low amount of additives to the Ca-source and also it is an advantage if low-cost precursors can be used [29, 32, 33]. Therefore, H.R. Radfarnia, M.C. Iliuta mention that sorbents doped with Al should be considered in stead of sorbents doped with Zr despite a lower cyclic performance since it is less expensive.

3.7 Factors affecting sorbent performance

3.7.1 Dispersion of inert support, Tammann temperature and surface area

Y. Hu et al. have synthesized 12 sorbents using calcium acetate monohydrate as Ca-source and the wet-mixing technique to introduce 12 different dopants (Y, Al, Mn, Mg, La, Yb, Nd, Ti, Ce, Zr, Si, Pr) [30]. Three factors were highlighted as particularly important with regards to CO₂ capturing performance; the dispersion of inert support, the melting temperature of the inert support and the specific surface area of the sorbent. A good dispersion of inert support is important to achieve the stabilizing effect among active particles that prevents sintering. It is desirable with a high melting temperature due to the correlation with Tammann temperature. In addition, a high specific surface area assists the carbonation reaction by exposing more active sites. H. R. Radfarnia, A. Sayari also mention that a high melting temperature of the inert support could counteract deactivation through sintering [32].

3.7.2 Pore volume

K. S. Sultana, D. Chen have synthesized sorbents based on a synthetic CaO-source and with the incorporation of Ce and Zr using cerium nitrate and zirconium nitrate [34]. They suggested that a higher performance of sorbents can be credited to not only a stabilizing inert phase and high specific surface area, as already mentioned, but also a large pore volume. This was explained by comparing the molar volumes of CaO and CaCO₃, which is 16.9 cm³/g and 36.9 cm³/g, respectively [34, 35]. Thus, as the carbonation-calcination cycling proceeds, volumetric changes for the particles arises since CaCO₃ occupies a significantly larger volume compared to CaO. Therefore, a large pore volume is desirable to prevent closure of pores due to particle growth as the carbonation reaction proceeds.

3.8 The impact of steam

A significant amount of work has been performed investigating the capturing capacity of CaO-based sorbents in a dry atmosphere. However, a realistic atmosphere for a CO₂ capturing system contains steam [36]. Therefore, studies have also been performed to investigate how the presence of steam in the carbonator and/or calciner affects the sorbent performance.

Experiments were carried out in a fluidized bed reactor using limestone as the raw material [36]. 10 carbonation-calcination cycles were executed in an atmosphere of N₂, CO₂ and 10 % steam. It was found that the presence of 10 % steam in both the carbonator and calciner had an enhanced effect on the capacity over 10 cycles [36]. Experiments using no steam, steam in both carbonator and calciner, and steam in only carbonator and calciner have also been performed. It was found that presence of steam in both the carbonator and the calciner gave the best overall performance, while steam present only in carbonator gave the second highest capacity. The authors mention that a synergistic effect could be observed when steam was present both during capture and regeneration. This means that the resulting effect of steam present in both carbonator and calciner is greater than the sum of partial effects of each component. The study revealed that having steam present during calcination promoted sintering which produced pores with a size of 50 nm. A positive effect of this was that the pores were more stable compared to the structure that evolved without any steam in the process. The presence of steam could reduce the diffusion resistance in the carbonation step.

Another work has tested sorbents based on limestone in wet carbonation conditions in TGA [37]. Experiments were performed at different carbonation temperatures, 400 °C, 450 °C and 550 °C. It was found that the addition of steam enhanced the conversion of CaO to CaCO₃ at the two lower carbonation temperatures, while the inclusion of steam at carbonation temperature 550 °C, which is the relevant temperature for this thesis, lowered the conversion.

Theory

4.1 Synthesis

Several different synthesis techniques exist for the preparation of catalytic materials, and the choice of technique may affect some qualities of the resulting material, such as dispersion of introduced compounds and the surface area [38]. The incipient wetness impregnation method was chosen as synthesis technique for the MBCL project, so section 4.1.1 gives a brief introduction to this method.

4.1.1 Incipient wetness impregnation (IWI)

Impregnation methods are straightforward synthesis techniques that are frequently used to produce a supported catalyst, and consist of the two subcategories incipient wetness impregnation, also called dry impregnation, and wet impregnation [38, 39]. The difference between these two methods is the volume of impregnation solution used. For wet impregnation the volume of solution added exceeds the pore volume.

For incipient wetness impregnation, the impregnation solution is prepared by dissolving a precursor in a volume which is approximately equal to the pore volume [2, 39]. The solution is added to the support at a slow pace, and the solution is dragged into the pores by capillary forces. The impregnation proceeds until the pores are saturated. The surplus liquid is eliminated through drying, and the rate of drying influences how the introduced material is positioned inside the pores. Slow and fast drying rates results in positioning of the introduced material at the bottom of the pore and in the pore opening, respectively. Impregnation methods are quick and uncomplicated. Nevertheless, a downside is the risk for variable positioning of introduced material throughout the pore system.

4.2 Characterisation

The characteristics of catalysts and sorbent materials are grouped into three categories; dynamic, physical and chemical [2]. Dynamic characteristics describes the activity and selectivity of the catalyst and sorbent material, physical characteristics comprise surface area, pore diameter, type of pore, pore size distribution, porosity and mechanical strength, among others, and chemical characteristics describe chemical conditions in the bulk matter and on the surface. The following sections will give a short introduction to these characteristics and characterisation methods relevant for this thesis.

4.2.1 Thermogravimetric analysis (TGA)

Thermogravimetric analysis (TGA) records variations in the sample mass as a function of temperature and time [40]. The CO₂ sorption capacities of the sorbents are found by assuming that the change in mass of sorbents during TGA experiments is due to sorption and desorption of CO₂. The instrumental setup consists of purge and balance gas, a thermobalance and a sample holder. Sample holders are available in different materials dependent on the nature of the material being characterised. A platinum sample holder is used for high-temperature characterisation, where the temperature goes beyond 800 °C. A ceramic sample holder is used for samples containing phosphorus since it reacts with platinum at temperatures above 900 °C. An expendable sample holder made of aluminium is used for low-temperature characterisation when the sample may leave permanent residue on the holder. The instrument can be operated with an inert, reducing, oxidizing, dry or wet atmosphere. Characterisation in a wet atmosphere includes use of steam in the apparatus.

4.2.2 N₂ adsorption-desorption measurement

The physical characteristics surface area, pore diameter, type of pore, pore size distribution and porosity can be found using a gas adsorption-desorption setup [41]. The adsorptive gas is often nitrogen at 77 K for evaluation of nonporous, mesoporous and macroporous materials. Micro-, meso- and macroporous materials are distinguished from one another by the pore diameter, which is < 2 nm, 2-50 nm and > 50 nm, respectively. An amount of 50-100 mg sample is pretreated with degassing. Degassing involves heating the sample under vacuum to eliminate physisorbed components, and thus, to ensure the samples have the same condition prior to the experiment [42]. It is recommended to perform two measurements in order to verify the results [1].

Specific surface area

The Brunauer-Emmett-Teller (BET) isotherm is extensively used for the determination of specific surface area [41]. As the isothermally N₂ adsorption-desorption experiment proceeds, the quantity adsorbed N₂ on the surface of the sample is recorded as a function

of pressure of the adsorbing gas. These adsorption isotherm data are further evaluated using the linear BET isotherm which is given by,

$$\frac{p}{V(p_0 - p)} = \frac{1}{V_m C} + \frac{(C - 1)p}{V_m C p_0} \quad (4.1)$$

where V is the amount of gas adsorbed, p and p_0 are the pressure and saturation pressure of the adsorptive gas, respectively, V_m is the volume of gas adsorbed at monolayer coverage and C is the BET constant.

The validity of the BET equation is based upon six assumptions; (i) the rate of adsorption and desorption are equivalent in each adsorption layer, (ii) the heat of adsorption is constant throughout the whole first layer, (iii) adsorption of molecules in subsequent layers takes place at adsorbed molecules in the previous layer, (iv) the adsorbed gas molecules have no impact on each other, (v) the heat of all layers, except the first one, are identical, and (vi) the width of the multilayer becomes infinitely thick as p approaches p_0 [26].

The BET equation is used to determine V_m [26]. Further, the adsorptive gas is assumed to be ideal. Then the number of gas molecules adsorbed on the surface is found by,

$$N_0 = \frac{pV_m}{RT} N_A \quad (4.2)$$

where N_A is Avogadro constant, T is the adsorption temperature and R is the universal gas constant. The specific surface area of the material is found by,

$$A = N_0 A_0 \quad (4.3)$$

where A_0 is the area occupied by the individual nitrogen molecules.

Type of pore

The shape of the adsorption isotherms differs dependent on the nature of the analyzed material, and six different isotherms are shown in Figure 4.1 [1]. Microporous materials give rise to the adsorption isotherm of type I. Type II is generated for non-porous or macroporous materials. Type III is uncommon. Type IV is common for mesoporous materials and is typically recognized by its hysteresis loop. Type V is also uncommon. Type VI is generated for a uniform non-porous material where multilayer adsorption takes place step by step.

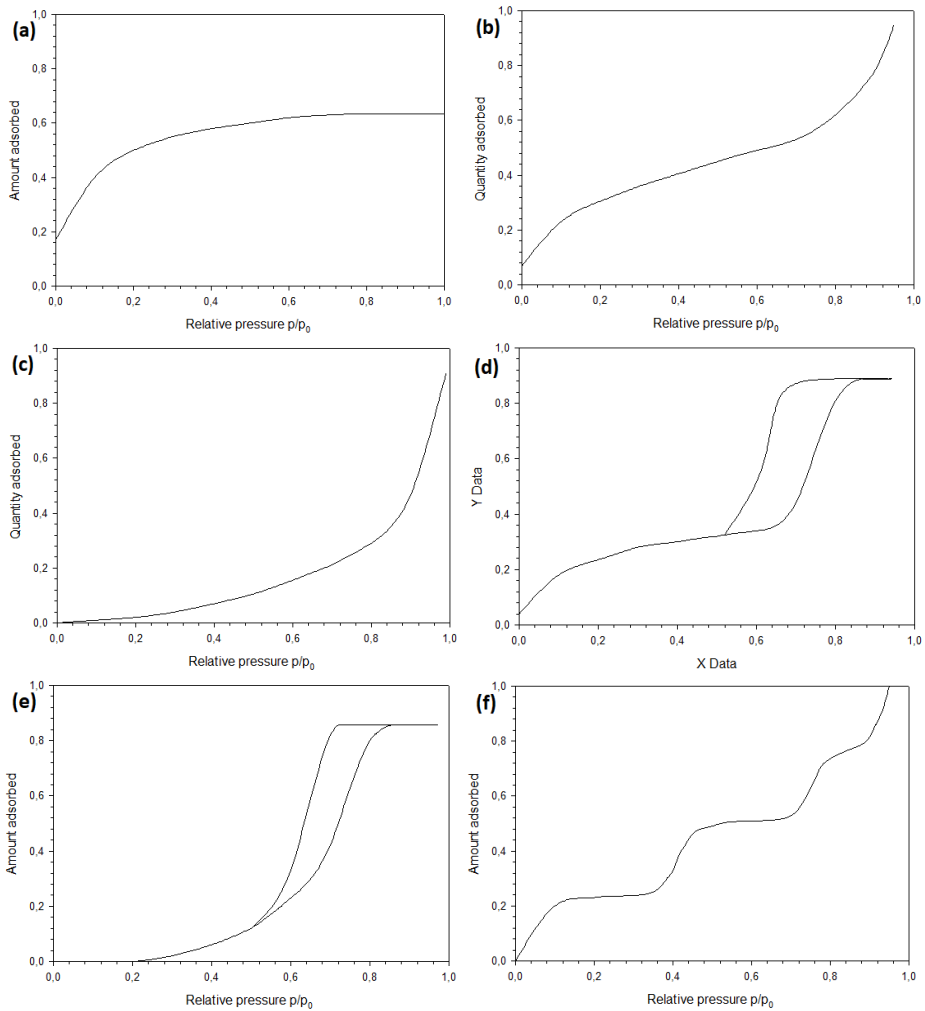


Figure 4.1: Adsorption isotherms. (a) Type I, (b) Type II, (c) Type III, (d) Type IV, (e) Type V, (f) Type VI. The figures are adapted based on existing images [1].

As mentioned, the adsorption isotherm of type IV is recognized by its hysteresis loops [1]. These loops arise due to capillary condensation in mesopores. Four different loops are generated based on the nature of the material, these are shown in Figure 4.2. Loop H1 and H4 are extreme cases, while loop H2 and H3 are considered as transitional cases. The cause for the different shapes of the loops is not fully comprehended, but can give indications about the pore structure. Loop H1 is often generated for materials consisting of spherical agglomerates positioned in a matrix-like structure. As a result, the pore size distribution of these materials is typically slim. The generation of loop H2 gives an unclear understanding of the pore structure. Hysteresis loops of type H3 and H4 are generated

when the material contains plate-shaped particles positioned so that pores are slit-shaped. The difference between H3 and H4 is that the latter shows tendencies of microporosity due to the similarity to isotherm I.

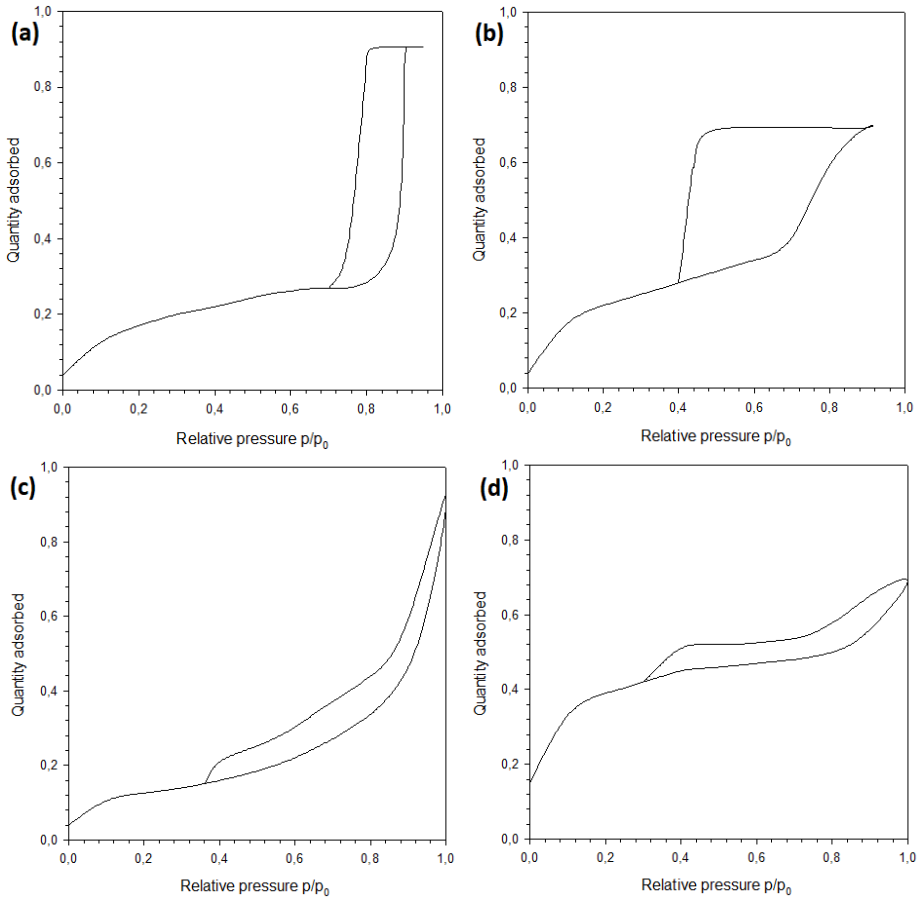


Figure 4.2: Hysteresis loops. (a) H1, (b) H2, (c) H3, (d) H4. The figures are adapted based on existing images [1].

Pore width and pore volume

The pore volume and pore diameter are found using the Barrett-Joyner-Halenda (BJH) method [41]. The validity of this method is based on five assumptions; (i) the Kelvin equation is valid through the mesoporous range, (ii) the pore diameter and pore shape determine the meniscus curvature, (iii) the pores are inelastic and have identical shapes (iv) the pore size distribution lie within the mesoporous range and (v) no pores are clogged. The Kelvin equation is given by,

$$\ln\left(\frac{p}{p_0}\right) = \frac{-2\gamma V_{\text{liq}} \cos\theta}{r_k RT} \quad (4.4)$$

where γ is the surface tension of liquid N_2 , V_{liq} is the molar volume of liquid N_2 , θ is the contact angle between liquid N_2 and the solid material and r_k is the Kelvin radius [2]. The Kelvin radius corresponds to the radius of a wetted pore and marks the beginning of the condensation in the pore [43]. The radius of the pore is found by,

$$r_p = r_k \cos\theta + t \quad (4.5)$$

where θ is the contact angle between liquid N_2 and solid and t is the thickness of the layer of adsorbed N_2 present prior to condensation [2, 43]. Normally it is assumed that liquid nitrogen completely wets the solid, and hence, $\theta = 0^\circ$.

The total pore volume is found from the adsorption isotherm generated in the N_2 adsorption-desorption measurement [1, 41]. The adsorption isotherm gives information about quantity $\text{N}_2(\text{g})$ adsorbed as a function of relative pressure, p/p_0 . When the relative pressure approaches 1, $p/p_0 \approx 1$, the pores are completely filled. Since the adsorption isotherm provides the amount adsorbed $\text{N}_2(\text{g})$ at p/p_0 , the total pore volume can be found by converting the gaseous volume to liquid volume.

Pore size distribution

The pore size distribution gives information about the contribution each pore diameter has to the total pore volume and is normally presented as $\Delta V_p/\Delta r_p$ as a function of r_p where V_p and r_p is the pore volume and mean pore radius, respectively [1, 44]. It is possible to use data from both the adsorption and desorption branch when presenting the pore size distribution [1]. Data from the desorption branch may be inaccurate if clogging of pores takes place in the analyzed material. Nevertheless, data from this branch is preferred by the majority of researches.

Porosity

Porosity is defined as the fraction of the pore volume constituting the total volume [45],

$$\theta = \frac{V_p}{V_t} = \frac{V_p}{V_s + V_p} \quad (4.6)$$

where θ is the porosity, V_p is the pore volume, V_s is the volume of compact solid and V_t is the total volume of the porous material.

Figure 4.3 (a) describes a relation between the activity of a catalytic pellet and its porosity [2]. An increase in porosity results in an increase in catalytic activity. Also a higher specific surface area gives increasing catalytic activity. The reasoning for this is that higher

porosity and specific surface area give better access to both available reactants and reaction sites. Figure 4.3 (b) shows a relation between crushing strength and porosity of a pellet; Increasing porosity leads to lower resistance to crushing.

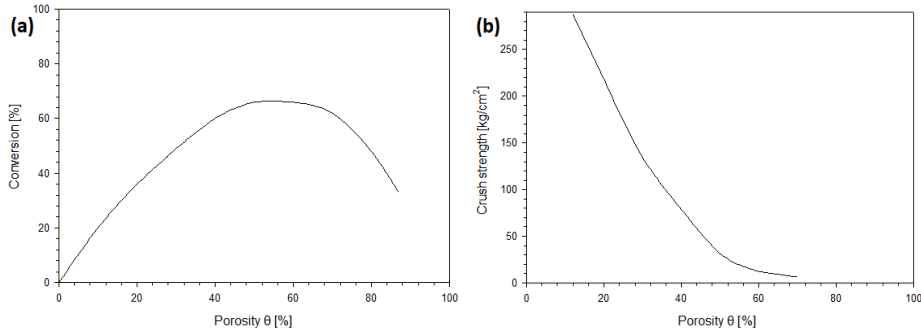


Figure 4.3: (a) The relation between conversion and porosity of pellets. (b) The relation between crush strength and porosity of pellets. The pictures are adapted based on existing images [2].

4.2.3 Mercury intrusion

Mercury intrusion is another method for assessing parameters of porous materials, such as specific surface area, pore volume, porosity and pore size distribution [45]. The difference between N₂ adsorption-desorption measurement and mercury intrusion is the detectable range of pore sizes. N₂ adsorption-desorption can effectively measure micro- and mesopores, while mercury intrusion can also detect macropores [2].

This technique is based on the intrusion of a non-wettable liquid into pores due to applied pressure [2, 45]. For a non-wettable liquid, the contact angle is above 90°, and the surface tension will hinder the fluid from being pushed into the pores. Application of enough pressure overrides this resistance. The correlation between the parameters mentioned above is given by Washburn's equation,

$$r_p = \frac{-2\gamma \cos\theta}{P} \quad (4.7)$$

where r_p is the pore radius, θ is the contact angle, γ is the surface tension and P is the applied pressure [2].

4.2.4 Analysis methods based on x-rays and beams of electrons

Characteristic X-rays

Characteristic x-rays are an essential part of the analysis methods; x-ray diffraction and energy-dispersive x-ray spectrometry, so the following describes the generation of these

[46].

An atom which is initially in its ground state may be bombarded with particles with high energy [47, 46]. The collision of these particles and an electron located in one of the inner shells of the atom may result in removal of the mentioned electron. As a consequence, the atom is in an excited state [47]. The atom returns to its ground state when an electron located in an outer shell moves down and fills the electron opening. This releases x-ray photons, also called characteristic x-rays.

The characteristic x-rays are defined as either K, L or M lines based on which shell is being refilled after electron removal [46]. Thus, x-rays belong to K, L or M lines if the electron opening is located in the K, L or M shell. In addition, the different x-ray lines can be divided into subgroups based on which shell the replacing electron comes from [48]. The movement of an electron from L_1 to K, from L_2 to K and from M to K generates $K\alpha_1$, $K\alpha_2$ and $K\beta$, respectively. The energy of the characteristic x-rays is equal to the energy difference between the removed electron and the replacing electron, and this energy is related to the different atoms through the atomic number.

Scanning electron microscopy (SEM)

Electron microscopes are apparatuses which are able to examine the nature of samples on nanometer scale, unlike optical microscopes which only detect details down to $1\ \mu\text{m}$ [49]. Therefore, electron microscopes have wide applications since it can be used to study surface morphology, the nature of primary particles and the whole range of pore sizes. Scanning electron microscopy (SEM) is a subcategory of electron microscopes, and is most extensively used [50].

The instrumental setup of a typical SEM comprises an electron gun, condenser lenses and an objective lens [50]. The intention of these instrumental parts is to provide a beam of free electrons and sharpen the beam. The sharpened beam is swept over the sample surface. The system is evacuated prior to analysis. The interaction between electrons and sample surface leads to transportation of electrons through the sample or back-bouncing [49]. The latter category contains backscattered electrons and secondary electrons. If electrons from the electron beam strike atoms in the specimen, these electrons are spread back in the opposite direction, and hence, they are called backscattered electrons. Secondary electrons are produced when an incoming electron strikes an electron of the sample atom which removes the sample electron. Backscattered electrons and secondary electrons have different functions; the former gives information about composition in the sample and the latter gives information about the surface of the sample [49, 50].

Energy-dispersive x-ray spectrometry (EDS)

X-ray spectrometry is a group of methods for determining chemical elements in a sample by analyzing characteristic x-rays [46]. Energy-dispersive x-ray spectrometry (EDS) is a subunit of x-ray spectrometry which utilizes x-ray energy for identification. EDS is often a

part of a scanning or transmission electron microscope, SEM or TEM, respectively. Thus, the method is also known as microanalysis since the method detects chemical elements on a restricted area on nanometer scale.

The three essential components of an EDS apparatus is the x-ray source, a sensor system and a system for gathering and analyzing data [46]. An x-ray tube is often used as the x-ray source and a Si(Li) diode is often used in the sensor system. When EDS is part of a SEM or TEM, an electron beam is used in stead of the x-ray tube. The analysis can take place in an atmosphere of air, helium or vacuum. Operating the instrument in vacuum enables the detection of light elements like carbon.

As mentioned in the beginning of section 4.2.4, characteristic x-rays are generated by exposing the area of interest to x-rays, and thus, the elemental composition is revealed. The result from EDS analysis is a spectrum showing the intensity of the characteristic x-rays as a function of their energy levels [46]. The $K\alpha_1$ and $K\alpha_2$ are often merged into $K\alpha$ since their energy levels are similar, and this merger is known as the $K\alpha$ doublet [46, 48]. Also, the EDS analysis generates an elemental chart where the location of different elements in the area of interest is shown using different colours.

X-ray diffraction (XRD)

X-ray diffraction (XRD) is a method used for structural analysis of a material, and provides information about crystalline phases and crystallite sizes [51]. The analysis requires monochromatic x-rays, which is radiation at one certain wavelength [48, 52]. This monochromatic x-ray originates from characteristic x-rays produced by a x-ray tube [48]. As mentioned, the radiations $K\alpha_1$ and $K\alpha_2$ is often known as the $K\alpha$ doublet. The $K\alpha$ doublet produced from Cu is most often utilized as monochromatic x-ray for x-ray diffraction. The x-rays travel through *Soller slits*, where the intention is to parallel the x-rays, before it hits the sample. A Bragg-Brentano arrangement is common, which means that the position of the x-ray beam is anchored while the sample platform and detector revolve around the axis perpendicular to the x-ray beam, and thus, ensuring that the sample is being irradiated at the specified range of angle 2θ .

Irradiation of the sample with monochromatic x-rays leads to diffraction in a grid and reflection of the beam [53]. X-rays reflected from two parallel planes may interfere constructively when leaving the grid. This occurs if Bragg's law is fulfilled. Bragg's law is,

$$n\lambda = 2d\sin\theta, \quad n = 1, 2, .. \quad (4.8)$$

where λ is the wavelength of the x-rays, d is the distance between two parallel lattice planes, n is an integer and θ is the angle between the incoming x-rays and lattice plane [51]. The characteristic distance between the two parallel lattice planes is then found, and is used to analyze the crystalline compound.

The result from a XRD analysis is a spectrum showing diffraction intensity as a function of 2θ [48]. Thus, the appearance of peaks in the diffraction diagram is due to the presence of a crystal where incoming x-rays have been diffracted by two lattice planes and the diffracted x-rays have experienced constructive interference. The peaks in the diffraction diagram may have different intensities and different width. The width of the peak is related to the crystallite size through the Scherrer equation,

$$L = \frac{K\lambda}{\beta \cos\theta} \quad (4.9)$$

where L is the crystallite size, λ is the wavelength of the x-ray, β is the width of the diffraction peak, θ is the angle between incoming x-rays and lattice wall and K is a constant which often has a value of 1 [51]. This analysis method only identifies the existence of crystalline compounds, and is not able to discover amorphous phases or well-dispersed particles. The two latter are either non-attending in the diffraction diagram or manifest itself as broad peaks which are not sharply defined.

Experimental procedure

5.1 Synthesis of sorbents

Calcined dolomite was doped with the elements Mg, Zr, Al and Ce, referred to as dopants in subsequent sections, using the precursors aluminium nitrate ($\text{Al}(\text{NO}_3)_3 \cdot 9\text{H}_2\text{O}$, purity 99.997 %), magnesium nitrate ($\text{Mg}(\text{NO}_3)_2 \cdot 6\text{H}_2\text{O}$, purity 99 %), zirconium nitrate (ZrN_2O_7 , purity 35 %) and cerium nitrate ($\text{Ce}(\text{NO}_3)_3 \cdot 6\text{H}_2\text{O}$, purity 99 %), all provided from Sigma Aldrich. Zirconium nitrate was given as a solution. Aluminium was also introduced into calcined dolomite using the precursor CaAl_2O_4 , also called Fondu cement. The product data sheet for Fondu cement is given in Appendix C. The latter precursor is insoluble in water, while the first four precursors are soluble. The following subsections describe the one-pot granulation procedure that was performed which consisted of incipient wetness impregnation and subsequent granulation.

5.1.1 Preparation of raw material

Dolomite was provided as AGRI Hagekalk supplied by Franzefoss Miljøkalk. The raw material was prepared by calcination at 800 °C for 6 hours in a high-temperature oven. Six heat-tolerant containers were filled with approximately 35 g dolomite in total. The dolomite was spread evenly in the bottom of the containers. Calcination took place with a temperature ramp of 10 °C/min from room temperature to 800 °C, then an isothermal period of 6 hours at 800 °C. The material was not taken out before the oven had cooled down to room temperature again.

5.1.2 Preparation of impregnation solutions

Impregnation solutions with the different precursors, except Fondu cement, were prepared in cylindrical glass containers (diameter 3 cm and height 10 cm). The amount of precursor needed for the impregnation solutions were found using the calculation presented in Appendix A.1. The precursors and distilled water were added to the containers which were placed into an Ultrasonic cleaner from VWR. The cleaner was run at 60 °C and with supersonic strength 9 in order for the precursors to dissolve completely. The final volume of the impregnation solutions was approximately the same, 9.0-12.5 mL. The amount precursors and distilled water used for preparation of the impregnation solutions are given in Table B.1 in Appendix B.1.

5.1.3 Incipient wetness impregnation

20 g of calcined dolomite was milled in a mortar (diameter 13 cm) for 10 minutes. Fondu cement was added when CaAl_2O_4 was used as the Al-source. The necessary amount of Fondu cement was found using the same calculation as for the soluble precursors, see Appendix A.1. It was assumed that Fondu cement only consists of CaAl_2O_4 in the calculation. The amount CaAl_2O_4 added is given in Table B.1 in Appendix B.1. Fondu cement was milled together with calcined dolomite for approximately 2 minutes to ensure a homogeneously mixture. Next, the calcined dolomite was impregnated using incipient wetness impregnation.

The same procedure was performed for each impregnation. Approximately 0.8 ml impregnation solution was added in 8 rounds. After each addition the mixture of solid powder and solution was milled thoroughly. Powder that was attached to the wall of the mortar during milling was scraped off. The milling and scraping was performed twice. Next, a smaller amount of impregnation solution was added, approximately 0.5 ml solution added in 2-4 rounds. Milling and scraping was also here performed twice. The duration of the impregnation was roughly 60 minutes. The total amount of impregnation solution used for impregnation is given in Table B.1 in Appendix B.1.

5.1.4 Granulation

The calcined dolomite was granulated immediately after being impregnated. Approximately 1.2 mL distilled water was added in 3-4 rounds. Milling of the mixture and scraping powder off walls was performed twice. After that, distilled water was added drop by drop while performing milling and scraping until granules were formed. The amount of water used for granulation is given in Table B.1 in Appendix B.1. The granulated mixture was transferred to a sift with mesh size $< 70 \mu\text{m}$. A spatula was used to split large granules into smaller pieces. The granules were dried in the sift covered by aluminium foil for three days in room temperature under ventilation. The sorbents were then sifted to separate granules into the ranges $< 250 \mu\text{m}$, $250\text{-}500 \mu\text{m}$, $500\text{-}850 \mu\text{m}$ and $> 850 \mu\text{m}$.

5.1.5 Pre-calcination

All sorbents within the size ranges 250-500 μm , 500-850 μm and $> 850 \mu\text{m}$ were calcined at 800 °C for 3 hours in 0.5 L/min N_2 and at 950 °C for 3 hours in an atmosphere of air, hereby referred to as pre-calcination. The first calcination had a temperature ramp of 5 °C/min, and the second calcination had a temperature ramp of 10 °C/min. The ovens were cooled without a cooling system.

Table 5.1 presents the precursors, desired weight percent of dopants and sample names.

Table 5.1: The precursors, desired weight percent of dopants in the final sorbent, indicated as D wt% i , and a sample name for the sorbents are given below. The sample name is given on the form AB where A and B are the introduced element. Al(sol) and Al(insol) corresponds to the soluble precursor aluminium nitrate and the insoluble precursor cement, respectively. Two sorbents are labelled with the subscripts A and B since the difference between them are the weight percent aluminium from cement.

Precursor i	Precursor j	D wt% i	D wt% j	Sample name
$\text{Al}(\text{NO}_3)_3 \cdot 9\text{H}_2\text{O}$	$\text{Mg}(\text{NO}_3)_2 \cdot 6\text{H}_2\text{O}$	3.0	3.1	Al(sol)Mg
CaAl_2O_4	$\text{Mg}(\text{NO}_3)_2 \cdot 6\text{H}_2\text{O}$	3.0	3.1	Al(insol)Mg
$\text{Al}(\text{NO}_3)_3 \cdot 9\text{H}_2\text{O}$	$\text{Ce}(\text{NO}_3)_3 \cdot 6\text{H}_2\text{O}$	3.0	2.9	Al(sol)Ce
CaAl_2O_4	$\text{Ce}(\text{NO}_3)_3 \cdot 6\text{H}_2\text{O}$	3.0	2.9	Al(insol)Ce
CaAl_2O_4	ZrN_2O_7	3.0	2.1	Al(insol) _A Zr
$\text{Mg}(\text{NO}_3)_2 \cdot 6\text{H}_2\text{O}$	$\text{Ce}(\text{NO}_3)_3 \cdot 6\text{H}_2\text{O}$	3.1	2.9	MgCe
$\text{Mg}(\text{NO}_3)_2 \cdot 6\text{H}_2\text{O}$	ZrN_2O_7	3.1	2.1	MgZr
$\text{Ce}(\text{NO}_3)_3 \cdot 6\text{H}_2\text{O}$		2.9		Ce
CaAl_2O_4	ZrN_2O_7	6.0	2.0	Al(insol) _B Zr

5.2 Thermogravimetric Analysis (TGA)

The CO_2 capacity and cyclic stability of all sorbents with size 500-850 μm were investigated in Linseis TGA. An amount of 15-20 mg of sample was loaded into a sample holder (diameter 6 mm and height 4 mm). The sorbents were first calcined at 950 °C for 3 hours in the instrument, which acted as a pre-calcination step, followed by 68 carbonation-calcination cycles. Carbonation was run at 570 °C in an atmosphere of 10 % CO_2 and 8 % steam balanced with Ar. Calcination was run at 950 °C in 100 % CO_2 . The calculation of CO_2 capacity in each cycle is presented in Appendix A.3. The sorbents are called fresh and spent prior to and after the CO_2 capturing experiment in Linseis TGA, respectively.

The sorbents were tested in 68 carbonation-calcination cycles, divided into 4 intervals, each consisting of 17 cycles. Interval 4 for sorbent MgZr was divided in two (12+5 cycles), and interval 2 and 3 for sorbent Al(insol)_BZr was also divided in two (11+6 cycles and 6+11 cycles, respectively) due to practical reasons. The experiment with pre-calcination and 68 carbonation-calcination cycles lasted for one week.

5.3 Scanning electron microscope (SEM)

The nature of primary particles of fresh and spent sorbents were investigated using a SEM APREO located in a cleanroom area with ISO class 6. The instrument had the detectors ETD, T1, T2 and Directional Backscattered Detector (DBS), acceleration voltage 0.2-30 kV and maximum beam current 400 nA, and was operated under vacuum.

Fresh sorbents with size $> 850 \mu\text{m}$ were milled in a mortar (diameter 13 cm) for 5 minutes. One granule of spent sorbent was transferred to a glass container and crushed with a spatula. Carbon tape was attached to a metal holder, and a small amount of fresh and spent sorbent powder grains were attached to the carbon tape using a swab. Pictures were taken with 0° tilt, 0° rotation, 2 kV voltage, 13 pA current, approximately 4 mm working distance, in immersion mode and T2 detector.

The average particle size observed in one SEM picture of fresh and spent sorbents was determined using the analysis program Fiji. 50 particles (30 and 32 for some sorbents due to few particles) were manually marked, and the program calculated the area of the marked particles. The particles were assumed to be spherical.

5.4 X-ray diffraction (XRD)

The crystalline phases and crystallite sizes were investigated in a Bruker D8 A25 DaVinci (XRD) with $\text{CuK}\alpha$ radiation with a LynxEyeTM SuperSpeed Detector. The diffractometer had Bragg-Brentano geometry, θ - θ operating mode, 2.5° primary and secondary Soller slits and a variable divergence slit. All sorbents size $> 850 \mu\text{m}$ were milled in a mortar (diameter 13 cm) for 5 minutes. The milled sorbents were then transferred to the sample container. A flat powder surface was achieved using a glass slide. The sorbents were analyzed as a crystalline sample for 30 minutes with angles $2\theta = 20$ - 80° . A constant length of 6 mm of the sample was illuminated at all angles by choosing V6. Bruker EVA and the database PDF -4+ 2012 RDB were used to analyze the diffraction diagram.

5.5 Falling test

Sorbents with size 250-500 μm and 500-850 μm were tested with a falling test in order to get a rough overview of the mechanical strength. The two different size ranges were tested separately. Approximately 1 g of the sorbent was dropped into a vertical tube with a length of 1.5 m. The sorbent landed on a concrete surface covered by a piece of paper. The granules with size 250-500 μm were then sifted in a sift with mesh size 250 μm for 10 seconds. The granules with size 500-850 μm was sifted in sifts with mesh sizes 250 μm and 500 μm for 10 seconds. The mass of the residue after the fall with size $< 250 \mu\text{m}$ and $< 500 \mu\text{m}$ were recorded. The remaining sorbent with size 250-500 μm and 500-850 μm was then dropped once more down the tube.

5.6 N₂ adsorption-desorption measurement

All sorbents with granule size 500-850 μm were characterised twice in a N₂ adsorption-desorption measurement in order to investigate type of pore, specific surface area, pore volume, pore width and pore size distribution. Approximately 85 g sample was used in each measurement. The samples were degassed overnight at 300 °C under vacuum using the VacPrep 061 from Micromeritics. N₂ at T = 77 K was used as adsorptive gas. The measurement was carried out in the Tristar II from Micromeritics. The sample weight was recorded before and after degassing, and after the gas adsorption experiment. Cotton gloves was used when handling the sample tube in order to prevent inaccuracy in the weight measurement.

5.7 Mercury intrusion

Calcined dolomite, Al(insol)Ce and Al(insol)_AZr were analyzed in a mercury porosimetry experiment which was performed by the laboratory technician Lars Erik Mollan Parnas from SINTEF AS Industry.

5.8 Energy-dispersive x-ray spectrometry (EDS)

The elemental composition of Fondu cement and calcined dolomite, as well as the fresh sorbents Al(sol)Mg, Al(insol)Mg, Al(insol)_AZr and MgZr was investigated using EDS Oxford which is part of the SEM APREO. The instrument has the properties X_{max} 80 mm², solid angle (10mm WD), 0.03409 srad, 127 eV. The elemental mapping was performed at 0 ° tilt, 0 ° rotation, 5.00 kV voltage, 0.4 nA current, 10 mm working distance, the standard mode and ETD detector in SE mode. The sample preparation was identical to the one described in section 5.3.

Results and discussion

6.1 Synthesis

This work has investigated how introduction of various combinations of dopants affects the capturing capacity and cyclic stability of dolomite-based sorbents. The elements used for this purpose were Mg, Zr, Al and Ce. Literature has shown that magnesium is an interesting additive due to the positive impact naturally occurring MgO has on cyclic stability in calcined dolomite, and thus, additional magnesium could possibly further enhance stability. Literature has reported good performance of sorbents doped with zirconium from different precursors (zirconium dioxide, zirconium nitrate), raw materials (dolomite, limestone, calcium acetate) and synthesis techniques (incipient wetness impregnation, wet mixing, spray drying) [31, 17, 22, 29]. Al-based sorbents have also shown relatively good results using limestone as raw material, wet mixing as synthesis technique and different precursors (aluminium acetate, aluminium nitrate, cement) [19, 29]. Sorbents incorporated with cerium have been synthesized using calcium acetate as the raw material, spray drying as the synthesis technique and cerium nitrate as the precursor, and have shown extremely stable capturing capacities over 20 cycles in dry conditions [31]. Thus, it would be interesting to further investigate the incorporation of these dopants in dolomite.

Mostly soluble precursors have been used in this work (aluminium nitrate, cerium nitrate, zirconium nitrate, magnesium nitrate) since it was suspected that the homogeneously incorporation of metal oxides is more difficult when using an insoluble precursor. However, the insoluble Al-precursor cement is cheaper and easier to handle during synthesis, since it is simply mixed together with dolomite instead of being introduced through an impregnation solution. Thus, Fondu cement has also been investigated as a possible Al-precursor. A sorbent containing 2.3 wt% Al and 1.5 wt% Zr, using the precursors aluminium nitrate and zirconium chloride, had a relatively high capturing capacity and showed the highest cyclic stability of the dolomite-based sorbents tested in dry TGA conditions [54]. This is

shown in Table C.2 in Appendix C.1. It showed to be more difficult to work with zirconium chloride as precursor than zirconium nitrate. Thus, only the latter has been utilized for the new sorbents. The combination of Al and Zr gave an overall better performance compared to Zr and Mg. Thus, the coupling of Al and Zr has been further investigated, together with other new combinations of dopants. Research has shown that a lower weight percent Zr (0.5 wt% and 1 wt%) gave higher performance of the sorbent compared to higher concentrations (5 wt% and 10 wt%) [17]. This has been taken into account when deciding weight percent Zr in the sorbents. It was found that the maximum weight percent additional Mg possible to incorporate into calcined dolomite is 3.3 wt% [54]. This is due to relatively low solubility of magnesium nitrate and the saturation limit of the pores in calcined dolomite. This has been taken into account when deciding weight percent additional Mg in the newly synthesized sorbents. The final important factor for deciding the weight percents dopants is the theoretical maximum capturing capacity. It was assumed that Al and Zr form inert phases together with CaO when calculating theoretical maximum capacity, and it was desirable with approximately the same theoretical maximum capacity for all sorbents.

The synthesis of sorbents is described in section 5.1. and Table 6.1 presents the desired and nominal weight percent dopants in the sorbents and the sample name. The nominal weight percent dopants in the final sorbent was found using the calculation given in Appendix A.2. The table also presents the calculated theoretical maximum capacity of the sorbents. This calculation is given in Appendix A.4.

Table 6.1: The precursors used, the desired and nominal weight percent dopants in the sorbents, denoted by D wt% i and N wt% i , respectively, and the sample name. The theoretical maximum capturing capacity is given as C_{\max} .

Precursor i	Precursor j	D wt% i	D wt% j	N wt% i	N wt% j	Sample name	C_{\max} [%]
$\text{Al}(\text{NO}_3)_3 \cdot 9\text{H}_2\text{O}$	$\text{Mg}(\text{NO}_3)_2 \cdot 6\text{H}_2\text{O}$	3.0	3.1	2.9	3.0	Al(sol)Mg	38.7
CaAl_2O_4	$\text{Mg}(\text{NO}_3)_2 \cdot 6\text{H}_2\text{O}$	3.0	3.1	2.8	2.9	Al(insol)Mg	38.6
$\text{Al}(\text{NO}_3)_3 \cdot 9\text{H}_2\text{O}$	$\text{Ce}(\text{NO}_3)_3 \cdot 6\text{H}_2\text{O}$	3.0	2.9	2.9	2.8	Al(sol)Ce	39.2
CaAl_2O_4	$\text{Ce}(\text{NO}_3)_3 \cdot 6\text{H}_2\text{O}$	3.0	2.9	2.9	2.7	Al(insol)Ce	39.2
CaAl_2O_4	ZrN_2O_7	3.0	2.1	2.8	2.0	Al(insol) _A Zr	38.6
$\text{Mg}(\text{NO}_3)_2 \cdot 6\text{H}_2\text{O}$	$\text{Ce}(\text{NO}_3)_3 \cdot 6\text{H}_2\text{O}$	3.1	2.9	2.9	2.7	MgCe	41.8
$\text{Mg}(\text{NO}_3)_2 \cdot 6\text{H}_2\text{O}$	ZrN_2O_7	3.1	2.1	2.8	1.9	MgZr	41.1
$\text{Ce}(\text{NO}_3)_3 \cdot 6\text{H}_2\text{O}$		2.9		2.9		Ce	44.1
CaAl_2O_4	ZrN_2O_7	6.0	2.0	5.7	1.8	Al(insol) _B Zr	33.5

There is a minor deviation between desired and nominal weight percent, and there are two reasons for this. First, when calculating the amount of precursor needed to achieve the desired weight percent dopant in the final sorbent, it was assumed that the final sorbent consists of only calcined dolomite and the dopant, as seen in Appendix A.1. Then, when calculating the nominal weight percent dopant in the final sorbent, it is assumed that the final sorbent consists of calcined dolomite and metal oxides, as seen in Appendix A.2. Second, small amounts of the impregnation solution remain in the beaker and pipette after performing incipient wetness impregnation. This explains the observed deviation between the desired and obtained weight percent dopant in the final sorbent.

The rate of drying of granules after impregnation and granulation was relatively slow since the sorbents were dried in room temperature while covered by aluminium foil. Theoreti-

cally, this means that the precursor was deposited at the bottom of the pore rather than at the pore opening which would be the case for fast drying, as mentioned in section 4.1.1.

The sorbents were subject to pre-calcination after impregnation, granulation and drying. The first pre-calcination step was carried out at 800 °C for 3 hours with the intention to decompose and evaporate nitrates arising from the precursors. This was performed in a non-reactive atmosphere, N₂, which is recommended for nitrate-based precursors, as mentioned in section 3.4. The second pre-calcination step took place at 950 °C for 3 hours in air atmosphere where the purpose was to create the solid framework of particles, as mentioned in section 3.4.

6.2 Thermogravimetric Analysis (TGA)

The CO₂ capacity and cyclic stability were investigated using the TGA, as described in section 5.2. The capacity for capturing CO₂ in each cycle, C_i for cycle i , was calculated using the approach presented in Appendix A.3. The capacity as a function of cycle i is presented in Figure 6.1 for the sorbents Al(sol)Mg, Al(insol)Mg, Al(sol)Ce and Al(insol)Ce, and in Figure 6.2 for the sorbents Al(insol)_AZr, MgCe, MgZr, Ce and Al(insol)_BZr.

All sorbents have an obvious initial decrease in CO₂ capturing capacity, and this behaviour is also well-known in literature [22, 23, 14]. Figure 6.1 and 6.2 show that the capacity values fluctuate, but the overall trend is a decreasing capacity as a function of cycle number. The reason for the fluctuation is most likely that the change in mass of the sorbent is lower than the sensitivity of the balance. The sorbents were tested in four intervals of 17 cycles, except sorbent MgZr and Al(insol)_BZr where some intervals had to be interrupted due to practical reasons. It can be observed that cycle 3 in every interval (C_{20} , C_{37} , C_{54} , and C_{66} for MgZr, and C_{31} and C_{43} for Al(insol)_BZr) has an elevated capacity. This is shown as peaks in Figure 6.1 and 6.2. This is most likely an instrumental curiosity caused by interrupted capturing experiments. The capacities stabilize and continue to follow the expected pattern after the peak in C_{20} , C_{37} and C_{54} , and this decreasing trend is the important feature.

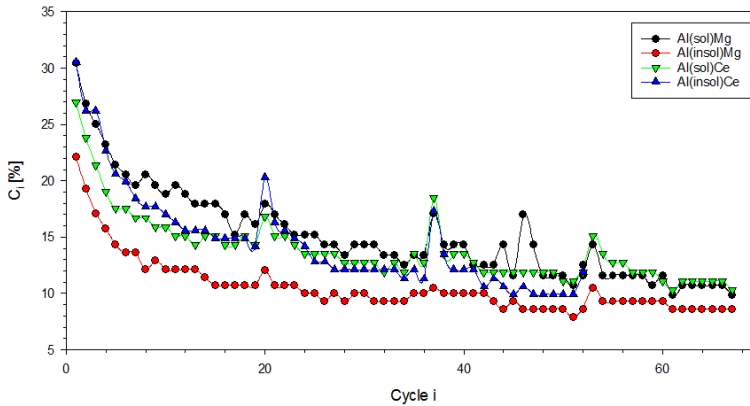


Figure 6.1: The CO₂ capacity plotted as a function of cycle number for the sorbents Al(sol)Mg, Al(insol)Mg, Al(sol)Ce and Al(insol)Ce.

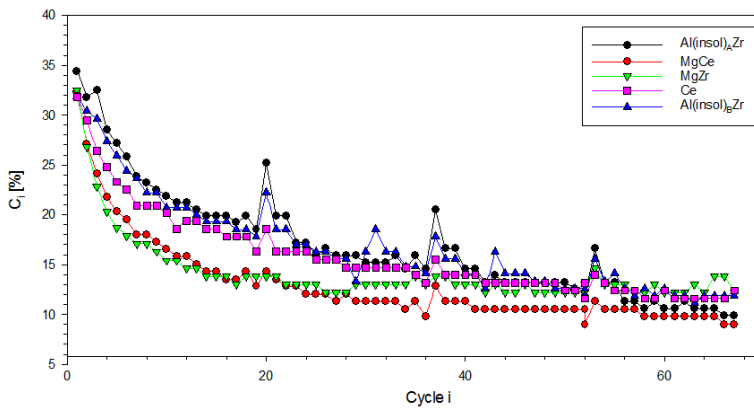


Figure 6.2: The CO₂ capacity plotted as a function of cycle number for the sorbents Al(insol)_AZr, MgCe, MgZr, Ce and Al(insol)_BZr.

The theoretical maximum CO₂ capturing capacity for calcined dolomite is 46 %, while the theoretical maximum capacity for the modified sorbents are presented in Table 6.1. As seen in Figure 6.1 and 6.2, the capacities of the modified sorbents in the initial cycles lay well below the theoretical maximum of calcined dolomite. This behaviour was expected, and also reported in literature, since unimpregnated calcined dolomite has a higher amount of active CaO-particles available for capturing CO₂ [30, 22]. During impregnation with different dopants, it is possible that the introduced element formed an inert phase together with Ca. Thus, some active CaO became part of an inert phase and was no longer able to participate in the capturing reaction. This lead to a reduced theoretical maximum capacity for the modified sorbents. The initial capacities were slightly below the calculated theoretical maximum for the individual sorbents. It is speculated that the reason for the deviation is due to the pre-calcination step which have caused sintering when forming the

solid framework.

Table 6.2 presents C_1 , C_{14} , C_{28} , C_{42} and C_{68} of the sorbents. These capacity values are representative for the sorbent performance during the carbonation-calcination cycling, and will be used to compare the sorbent performance. The relative loss in capacity from cycle i to cycle j , given as $L_{i,j}$, was calculated using Equation A.21 in Appendix A.5. The relative loss from C_1 to C_{14} , and the relative loss from C_{14} to C_{28} , C_{42} and C_{68} are presented in Table 6.2. These numbers give an indication of the stability of the sorbents over several cycles. A lower number for $L_{i,j}$ means higher stability. Table 6.2 shows that C_1 for most of the sorbents lay in the same range, around a value of 30 %. The exceptions are the sorbents Al(insol)Mg and Al(insol)_AZr which had the lowest and highest initial capacity, 23.3 % and 36.1 %, respectively. Regardless of the initial capacity of the sorbents, one can observe that the values of final capacities are much closer, they lay in the range 9.0-12.4 %.

Table 6.2: C_1 , C_{14} , C_{28} , C_{42} and C_{68} of the sorbents. The loss in CO₂ capacity for cycle j relative to cycle i , $L_{i,j}$, is also presented.

Sorbent	C_1 [%]	C_{14} [%]	C_{28} [%]	C_{42} [%]	C_{68} [%]	$L_{1,14}$ [%]	$L_{14,28}$ [%]	$L_{14,42}$ [%]	$L_{14,68}$ [%]
Al(sol)Mg	32.4	19.0	14.3	13.3	10.5	41.2	25.0	30.0	45.0
Al(insol)Mg	23.3	12.0	9.8	10.5	9.0	62.8	18.8	12.5	25.0
Al(sol)Ce	28.6	16.0	13.4	12.6	10.9	50.7	15.8	21.1	31.6
Al(insol)Ce	32.3	16.5	12.8	11.3	-	48.9	22.7	31.8	-
Al(insol) _A Zr	36.1	20.8	16.7	13.9	10.4	35.7	20.0	33.3	50.0
MgCe	34.1	15.1	12.7	11.1	9.5	53.4	15.8	26.3	36.8
MgZr	32.5	13.8	12.2	12.2	12.2	57.3	11.8	11.8	11.8
Ce	31.8	18.6	14.7	13.2	12.4	42.5	20.8	29.2	33.3
Al(insol) _B Zr	31.9	19.3	15.6	12.6	11.9	40.5	19.2	34.6	38.5

Calcined dolomite was doped with aluminium from nitrate, aluminium from cement, magnesium, zirconium and cerium, and this gives rise to five main groups of sorbents. A comparison of the sorbents within these five main groups are given in Figure 6.3, 6.4, 6.5, 6.6 and 6.7. The intention is to observe how the coupling of different dopants affects the sorbent performance. As mentioned in section 1.1, a high cyclic stability is preferred over high initial capacity, so this will be the focus in the following discussion.

Figure 6.3 shows a bar plot of the selected CO₂ capturing values given in Table 6.2 for the two sorbents with aluminium from a soluble precursor as additive, Al(sol)Mg and Al(sol)Ce. The figure shows that Al(sol)Mg had the lowest initial loss in capacity, where initial loss means relative loss in CO₂ capturing capacity from C_1 to C_{14} . It is also observed that addition of Al and Ce lead to higher stability from C_{14} to C_{68} compared to the sorbent with Al and Mg as additives.

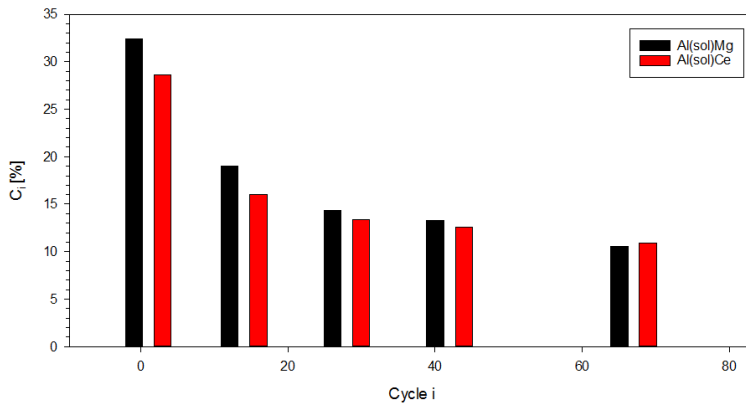


Figure 6.3: The CO₂ capacity of Al(sol)Mg and Al(sol)Ce in C₁, C₁₄, C₂₈, C₄₂ and C₆₈.

Capturing capacities of sorbents containing aluminium from cement as additive is shown in Figure 6.4. It can be seen that Al(insol)_AZr had the lowest initial loss in capacity. The sorbent Al(insol)Mg had a starting capacity that was noticeably lower than the other sorbents, and also had the overall lowest capacities. However, after a rather high decrease of initial capacity, the capacity stabilized, and the sorbent had the highest stability from C₁₄ to C₆₈. Literature has reported that C₁ and C₃₅ are 40 % and 37 % for a limestone-based sorbent doped using cement as precursor [19]. These results are higher than the sorption capacities for cement-based sorbents in this work, but the sorption capacities are not directly comparable due to different raw materials and number of additives. The limestone-based sorbent showed good cyclic stability. However, the regeneration of sorbents took place at 850 °C unlike the calcination in this work which was run at 950 °C. As mentioned in section 3.1, the rate of sintering and temperature have an exponentially relation, so this may explain the differences in stability.

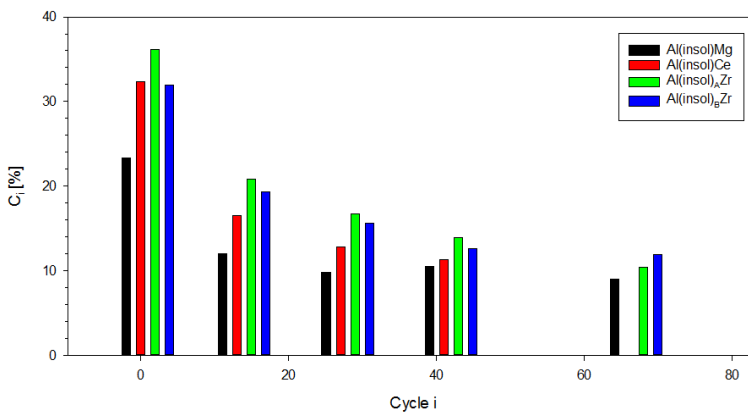


Figure 6.4: The CO₂ capacity of Al(insol)Mg, Al(insol)Ce, Al(insol)_AZr and Al(insol)_BZr in C₁, C₁₄, C₂₈, C₄₂ and C₆₈.

Figure 6.5 shows a comparison of the sorbents containing magnesium as additive. The sorbent Al(sol)Mg had the lowest initial loss, while the sorbent MgZr showed excellent cyclic stability from C_{14} to C_{28} . It should be mentioned that the sorbent Al(insol)Mg, which had highest stability from C_{14} to C_{28} among sorbents containing Al from cement, has the second highest cyclic stability among sorbents containing Mg. However, the overall capturing capacity lay at a lower level than for MgZr.

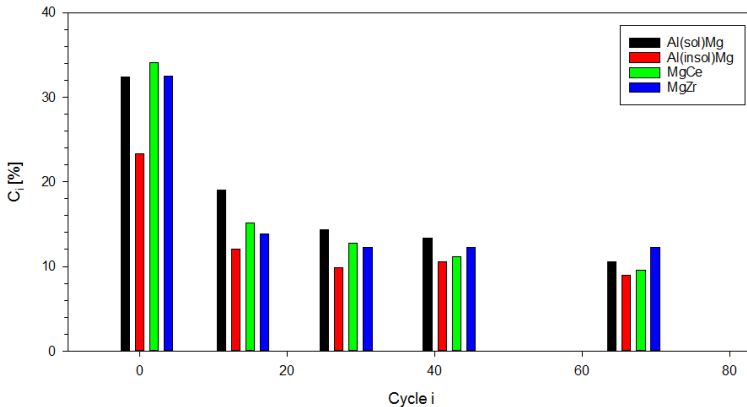


Figure 6.5: The CO₂ capacity of Al(sol)Mg, Al(insol)Mg, MgCe and MgZr in C_1 , C_{14} , C_{28} , C_{42} and C_{68} .

Figure 6.6 shows a comparison of the sorbents containing zirconium as additive. The sorbent with lowest initial capacity loss was Al(insol)_AZr. The sorbent MgZr had a significant loss of initial capacity, but showed excellent stability in the remaining cycles. This sorbent was most stable from C_{14} to C_{68} , like the case for sorbents containing magnesium.

Literature reported that sorbents based on dolomite were synthesized using zirconium nitrate as precursor and IWI as the synthesis technique [17]. The sorbents contained 0.5 wt% and 1 wt% Zr and had initial capacities of 33 % and 22 %, respectively, and final capacities of 21 % and 19 % after 60 cycles. As seen in Table 6.2, the capacities in the first cycle for the Zr-doped sorbents were 36.1 %, 32.5 % and 31.9 % for Al(insol)_AZr, MgZr and Al(insol)_BZr. Thus, the capacities in the first cycle are comparable to the sorbent containing 0.5 wt% Zr and higher than the one with 1 wt% Zr. The sorbents synthesized in this work had higher weight percent Zr, in addition to presence of another dopant. The initial capacity was therefore expected to be lower than the ones reported. It is suspected that the reason for the opposite behaviour is the more comprehensive calcination procedure. The sorbents were calcined at 900 °C for 15 hours prior the the cyclic experiment and then calcined at 950 °C for 3 hours in the TGA, as opposed to the sorbents synthesized in this work which was calcined for 3 hours at 950 °C. The reported results indicated a significantly lower decline in sorption capacity compared with the ones in this work. Besides the fact that the sorbents contain different dopants and in different amounts, the calcination was run at 900 °C, unlike the calcination in this work which was run at 950 °C. This may have caused some of the difference in cyclic stability. Also, the carbonation was run in an atmosphere of 10 % CO₂ and 1 % steam balanced by N₂, while the steam content

was raised to 10 % in this work. As mentioned in section 3.8, literature has reported both enhancing and descending performance of limestone-based sorbents when adding steam to the carbonation atmosphere. Presence of steam will likely affect the sorption capacity, but the direction of the influence is uncertain since dry sorption experiments have not been performed in this research, and because of the contradictory results reported in other research. Thus, it is speculated that the difference in these factors have caused varying cyclic stability of the reported sorbents and the sorbents in this work.

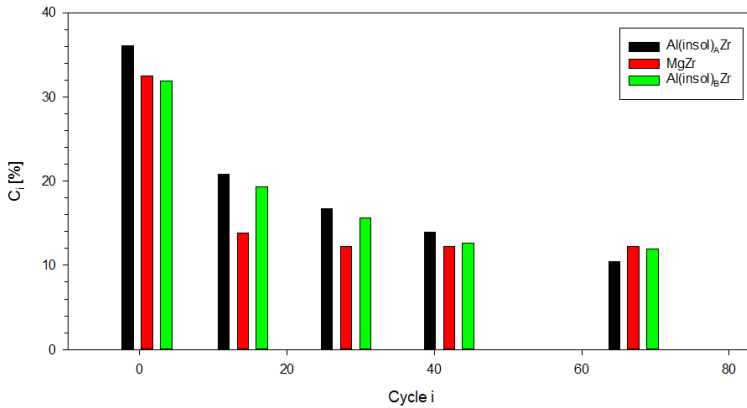


Figure 6.6: The CO₂ capacity of MgZr and Al(insol)_BZr in C₁, C₁₄, C₂₈, C₄₂ and C₆₈.

Figure 6.7 shows a comparison of the sorbents containing Ce as additive. The sorbent containing only Ce as additive had the lowest initial capacity loss, while Al(sol)Ce had the highest cyclic stability from C₁₄ to C₆₈. A doctoral thesis also synthesized three sorbents containing only Ce as the additive [31]. The sorbents had capacities in the range 45-55 % and complete stabilization over 20 cycles. However, the direct comparison of the Ce-doped sorbents with these sorbents is imprecise since the raw material, synthesis technique, amount of additives and TGA conditions differs.

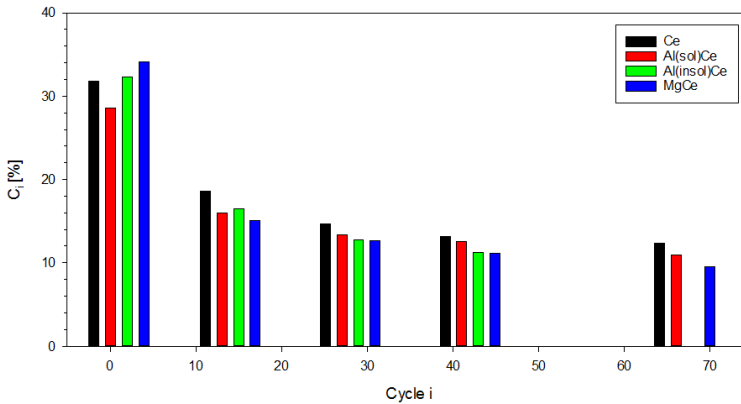


Figure 6.7: The CO₂ capacity of Al(sol)Ce, Al(insol)Ce, MgCe and Ce in C₁, C₁₄, C₂₈, C₄₂ and C₆₈.

Three sorbents stood out as the most stable ones during the initial phase of operation. The sorbent Al(sol)Mg within the groups containing aluminium from nitrate and magnesium, the sorbent Al(insol)_AZr for the groups containing aluminium from cement and zirconium and the sorbent Ce among the sorbents with cerium as additive. Three sorbents displayed the overall highest stability from C₁₄ to C₆₈. The sorbent Al(sol)Ce among the sorbents with aluminium from nitrate and cerium as additive, the sorbent Al(insol)Mg for sorbents using aluminium from cement as precursor and the sorbent MgZr among the group of sorbents containing magnesium and zirconium. Thus, it is also observed that no sorbents have both the lowest decline in sorption capacity and overall lowest loss in capacity from C₁₄ to C₆₈. By comparing the obtained results from the carbonation-calcination cycling and results reported in literature, it is evident that the obtained capacities were slightly lower. As mentioned, the direct comparison becomes incorrect due to differences during the synthesis and testing in the TGA.

The following sections present results and discussions about the characterisation methods SEM, XRD, falling test, N₂ adsorption-desorption, mercury intrusion and EDS. It is emphasized that these characterisations were performed on fresh sorbents, except SEM where pictures of both fresh and spent sorbents were taken.

6.3 Scanning electron microscope (SEM)

Pictures were taken of both fresh and spent sorbents with SEM, as described in section 5.3. Several pictures were taken of the same area at different magnifications. These pictures are not included in this thesis, but are available for the project Moving Bed Carbonate-Looping (MBCL) Technology for Post-Combustion CO₂ capture. One selected picture of each fresh and spent sorbent taken with magnification 100 000x is given in Figure 6.8-6.16.

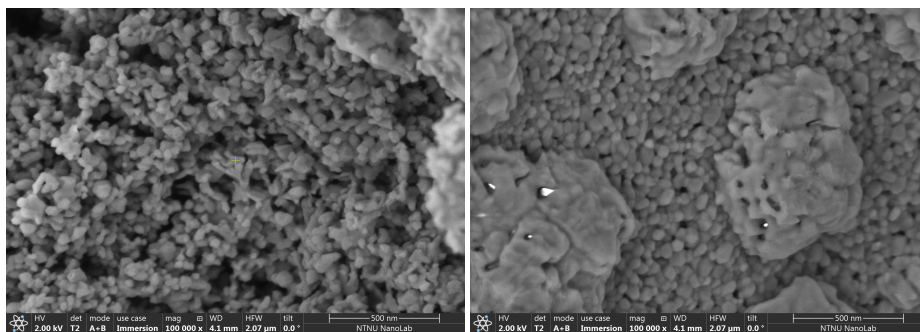


Figure 6.8: SEM picture of fresh and spent Al(sol)Mg.

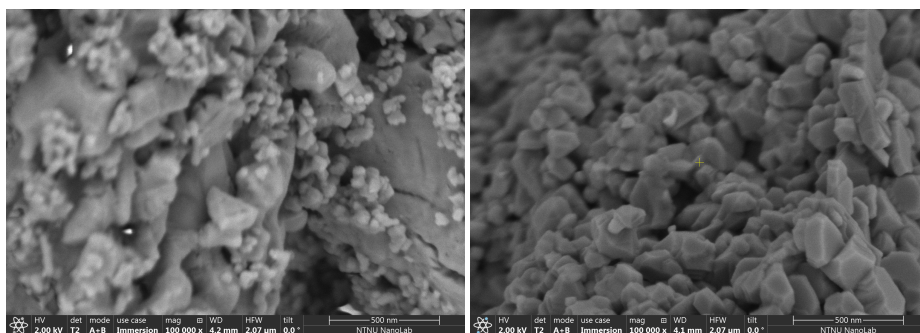


Figure 6.9: SEM picture of fresh and spent Al(insol)Mg.

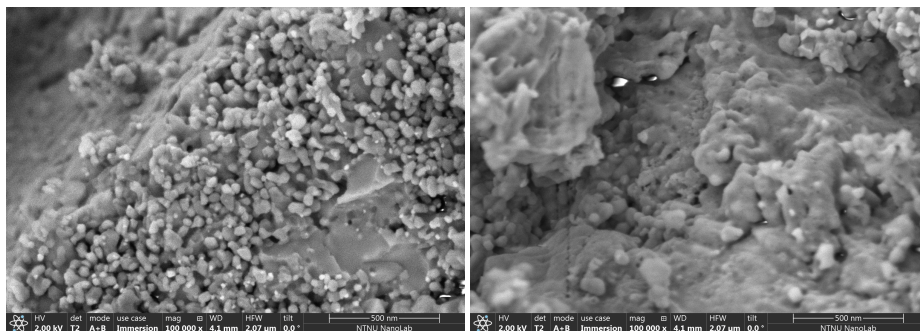


Figure 6.10: SEM picture of fresh and spent Al(sol)Ce.

6.3 Scanning electron microscope (SEM)

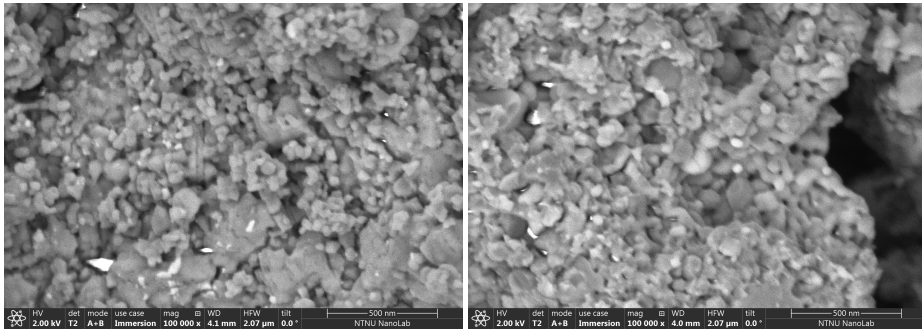


Figure 6.11: SEM picture of fresh and spent Al(insol)Ce.

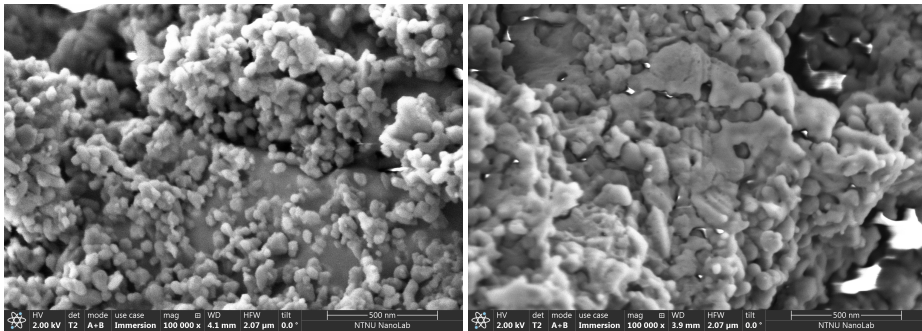


Figure 6.12: SEM picture of fresh and spent Al(insol)_AZr.

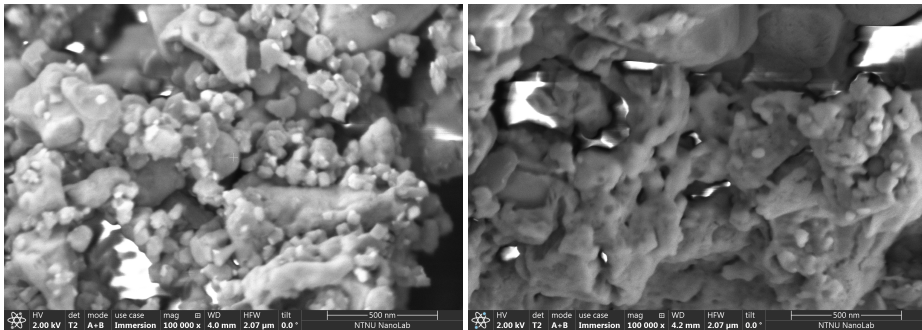


Figure 6.13: SEM picture of fresh and spent MgCe.

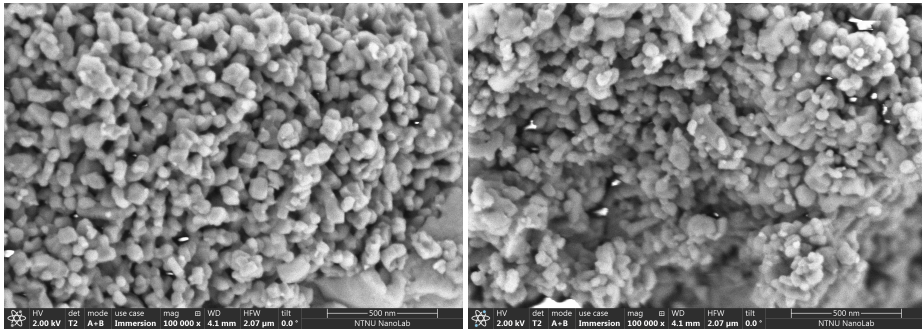


Figure 6.14: SEM picture of fresh and spent MgZr.

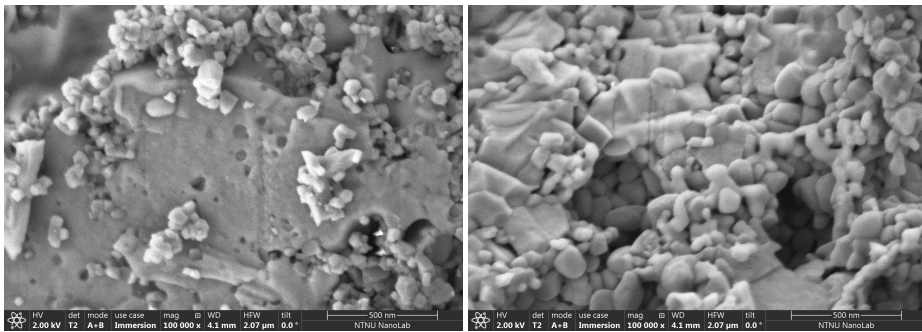


Figure 6.15: SEM picture of fresh and the spent sorbent Ce.

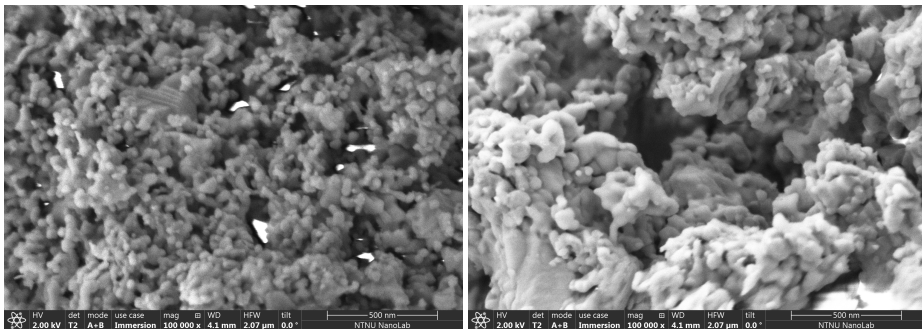


Figure 6.16: SEM picture of fresh and spent Al(insol)_BZr.

Literature reports that sintering is a well-known deactivation mechanism for CaO-based sorbents, as mentioned in section 3.1 [14, 22, 23]. Thus, the pictures were taken with the intention to investigate if any structural changes on nanoscale could be detected before and after the carbonation-calcination cycling. It is assumed that the pictures are representative for the overall condition of the sorbent. The average particle diameter observed in these SEM pictures was determined, and are given in Table 6.3. These average particle

sizes were calculated assuming spherical particles, but as seen in the pictures, some particles also had various non-spherical shapes. Also, the number of particles used during the calculation varies between 30, 32 and 50 particles. Therefore, these numbers are not exact, but rather give an indication of the particles sizes. The overall trend is an increasing average particle size when comparing fresh and spent sorbents. Observation of the SEM pictures shows a clear difference between the nature of primary particles of the fresh and spent sorbents. The fresh sorbents generally had a more open structure. The pictures of spent sorbents reveal a more compact structure, and it seems like the primary particles have fused to form larger particles, and this is also indicated by the average particle diameters in Table 6.3. The observed compact structure in spent sorbents indicates pore break-down, and thus, concealing of active CaO. However, it is hard to observe considerable differences between the primary particles of the spent sorbents. This observation is consistent with C_{68} , given in Table 6.2, since the capacities in the last cycle were comparable.

Table 6.3: Average particle diameter calculated based on 50 particles in SEM pictures. It was assumed that the particles are spherical.

Sorbent	d_{fresh} [nm]	d_{spent} [nm]
Al(sol)Mg	52	62
Al(insol)Mg	70**	112*
Al(sol)Ce	56	60**
Al(insol)Ce	46	62*
Al(insol) _A Zr	56	76*
MgCe	74	90**
MgZr	64	106
Ce	64	80
Al(insol) _B Zr	60	70*

*Average particle diameter based on 30 particles.

**Average particle diameter based on 32 particles.

As mentioned in section 3.7.2, the molar volume of CaCO_3 is significantly higher than for CaO. Therefore, it was suspected that some permanent pore blocking was due to the formation of CaCO_3 during carbonation which then became trapped in pores causing the lowering in capturing capacity. However, the weight of sorbents in the regenerated state in different cycles during the TGA experiments varies with 0-0.2 mg. This is evident by exploring the raw data files from the experiments given in Appendix B.3. Figure B.8 is given as an example, and the trend was the same for all other raw files. This small variation in weight is assumed to be caused by the sensitivity of the balance. This means that all the captured CO_2 was released during the calcination step, and the permanent pore blocking was most likely not due to trapped CaCO_3 , but rather, sintering of CaO-particles.

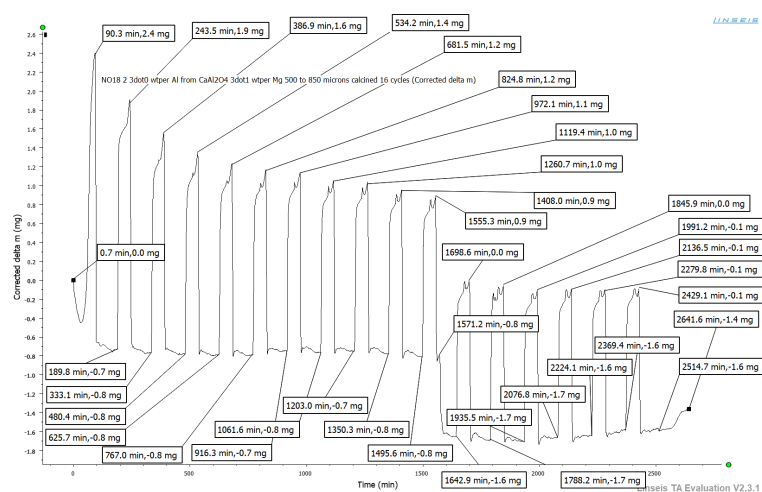


Figure 6.17: Raw data from the CO₂ capturing experiment performed in Linseis TGA for the sorbent Al(insol)Mg. The picture shows C₁ to C₁₇.

6.4 X-ray diffraction (XRD)

The diffraction diagrams for calcined dolomite and the sorbents are presented in Figure 6.18, 6.19 and 6.20. The diffraction diagram for calcined dolomite is given as a reference. The analysis confirmed that calcined dolomite and all the sorbents contained CaO and MgO. The analysis also revealed that calcined dolomite contained CaCO₃ and Ca(OH)₂, and this can be explained by incomplete calcination of dolomite and exposure to humidity, respectively. The incomplete calcination only leads to presence of CaCO₃, and not MgCO₃, and this was because calcination of MgCO₃ takes place at a lower temperature than CaCO₃, as mentioned in section 1.1.

A comparison of the diffraction diagrams of calcined dolomite and the sorbents revealed the absence of CaCO₃ and Ca(OH)₂. This was most likely due to the pre-calcination step which completed the calcination and evaporated water, respectively. Introduction of the elements Mg, Zr, Al and Ce lead to the formation of the phases MgO, CaZrO₃, Ca₁₂Al₁₄O₃₃ and CeO₂ which is inert with respect to CO₂ capture. All diffraction diagrams had one peak at approximately 26.7° which could not be associated with a crystalline phase. It is suspected that this is an impurity phase originating from dolomite.

The detection of CaZrO₃ has also been reported in literature when using the liquid precursors zirconium dioxide and zirconium nitrate [31, 17, 22, 29]. The formation of CeO₂ is also in agreement with literature, it was reported that this phase was formed when using cerium nitrate as precursor. Several different possibilities of stabilizing phases exist for the addition of aluminium to CaO-based sorbents. It has been reported that CaAl₂O₄ was formed using aluminium oxide and aluminium nitrate [31, 22], Ca₉Al₆O₁₈ was formed using aluminium acetate and aluminium nitrate as precursor [29] and Ca₁₂Al₁₄O₃₃ was

formed using cement as precursor [19]. Thus, it is evident that that different precursors and synthethis techniques affects which inert Al-phase is formed during heat treatment. It was investigated if any of the Al-based phases mentioned in literature was present in the synthesized sorbents. It was found that $\text{Ca}_{12}\text{Al}_{14}\text{O}_{33}$ was present in the sorbents based on the correspondance between intensities of peaks and phase lines. The peak with highest intensity also had the highest phase line.

The presence of these phases are likely to affect the CO_2 capturing capacity and the cyclic stability. First of all, formation of the phases $\text{Ca}_{12}\text{Al}_{14}\text{O}_{33}$ and CaZrO_3 lead to reduced theoretical capturing capacity since the dopant had reacted with CaO , and thus, captured some active CaO into an inert phase making it unavailable for incoming CO_2 . In addition, the formation of additional metal oxides lead to decreased theoretical capturing capacity according to Equation 1.4 given in section 1.1 due to increasing value of the denominator. Despite lower theoretical maximum capturing capacity, the intention of introducing these phases was to achieve sorbents with higher performance due to structural stabilization of CaO -particles to prevent sintering.

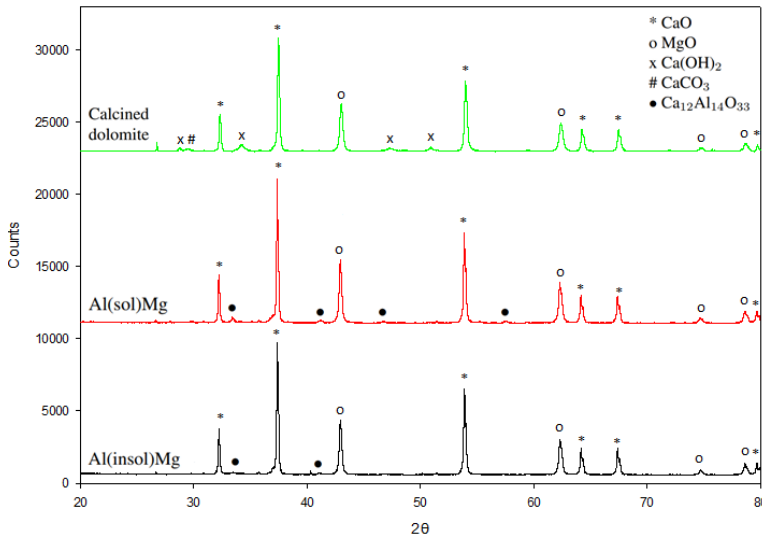


Figure 6.18: Diffraction diagram of calcined dolomite, Al(sol)Mg and Al(insol)Mg.

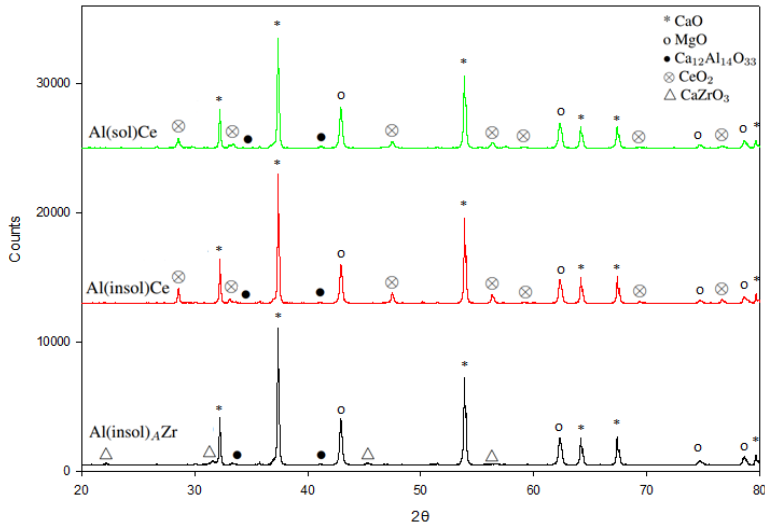


Figure 6.19: Diffraction diagram of Al(sol)Ce, Al(insol)Ce and Al(insol)_AZr.

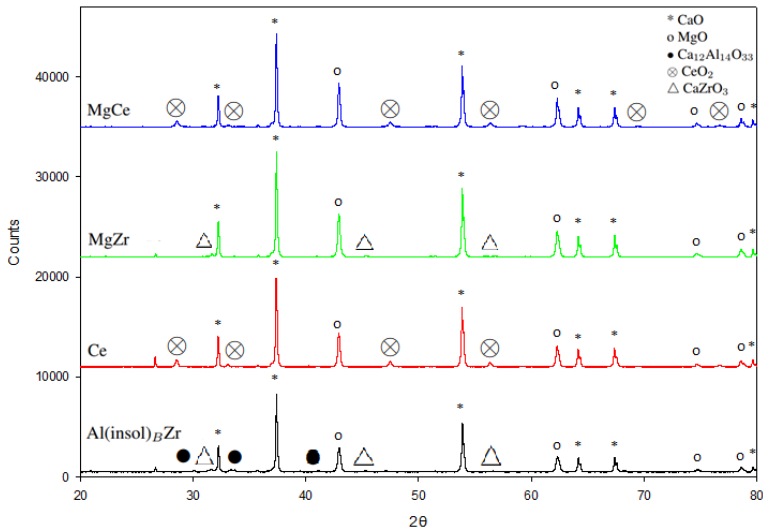


Figure 6.20: Diffraction diagram of MgCe, MgZr, Ce and Al(insol)_BZr.

The average crystallite sizes of the detected crystalline phases are presented in Table 6.4. Background noise and contamination in the diffraction diagrams caused by $K\alpha_2$ radiation were extracted to achieve correct measurements. The crystallite sizes were calculated using Scherrer equation given in Equation 4.9 in section 4.2.4, and the values are an average based on the crystallite size of six, four, two and four peaks for the phases CaO, MgO, CaZrO₃ and CeO₂, respectively. It was not possible to calculate the crystallite size of

$\text{Ca}_{12}\text{Al}_{14}\text{O}_{33}$ due to undefined peaks. The crystallite size of CaO and MgO in the sorbents lay in the range of 71-91 nm and 40-62 nm, respectively, while the crystallite size of the same phases for the raw material was 59 nm and 36 nm. Thus, the trend is a larger size for these two phases in the sorbents, and this was most likely due to the pre-calcination step after impregnation, granulation and drying which caused sintering, and thus, crystallite growth. This theory is in agreement with the results from the analysis of SEM pictures which indicated larger particles in spent sorbents compared to fresh sorbents as a result of sintering during the carbonation-calcination cycling.

It was suspected that the additional formed phase MgO would affect the crystallite size of naturally occurring MgO. This would apply to the sorbents Al(sol)Mg, Al(insol)M, MgCe and MgZr which contain additional MgO. As seen in Table 6.4, the crystallite size of MgO in these sorbents was not noteworthy higher than any other sorbents, except MgCe. It was also suspected that the crystallite size of CaO would be lower for the sorbents containing a CaO-capturing phase. This applies to all sorbents, except MgCe and Ce. The crystallite size of CaO in these sorbents was not remarkable lower. Therefore, it is speculated that the crystallite sizes of MgO and CaO would be affected by additional Mg and formation of CaO-capturing phases if the concentration of added material was higher.

Table 6.4: The crystallite sizes (cs) of the crystalline phases.

Sorbent	cs_{CaO} [nm]	cs_{MgO} [nm]	$cs_{\text{Ca}_{12}\text{Al}_{14}\text{O}_{33}}$ [nm]	cs_{CaZrO_3} [nm]	cs_{CeO_2} [nm]
Calcined dolomite	59	36	-	-	-
Al(sol)Mg	77	48	-	-	-
Al(insol)Mg	78	48	-	-	-
Al(sol)Ce	71	44	-	-	36
Al(insol)Ce	91	48	-	-	63
Al(insol) _A Zr	82	46	-	36	-
MgCe	83	62	-	-	36
MgZr	83	47	-	40	-
Ce	79	54	-	-	42
Al(insol) _B Zr	81	40	-	52	-

As mentioned in section 3.7.1, a higher Tammann temperature of the stabilizing phase has proven to be advantageous. The Tammann temperatures of MgO, CaZrO_3 , $\text{Ca}_{12}\text{Al}_{14}\text{O}_{33}$ and CeO_2 are 1483 °C, 1275 °C, 744 °C and 1352 °C, respectively. These are listed in Table B.2 in Appendix B.2. There are small variations in the Tammann temperatures of the phases, except for the phase $\text{Ca}_{12}\text{Al}_{14}\text{O}_{33}$. It was observed that the three sorbents Al(sol)Ce, Al(insol)Mg and MgZr had the highest stability from C₁₄ to C₆₈. Since all four stabilizing phases are present in the three most stable sorbents, it is difficult to observe a relation between stability and Tammann temperature.

6.5 Falling test

The mechanical strength of the fresh sorbents was investigated using a falling test, as described in section 5.5. The result is given in Figure 6.21 where the total relative percentage

weight loss is plotted as a function of number of drops. Two different size ranges were tested for each sorbent, 250-500 μm and 500-850 μm , and this constitutes the total mass of sorbents being dropped. Weight loss means the residue formed after the fall which had size below the tested size range. For example, the residue after dropping granules with size 500-850 μm had size $< 500 \mu\text{m}$ while the residue after dropping granules with size 250-500 μm had size $< 250 \mu\text{m}$. The calculation of total relative percentage weight loss during the falling test is presented in Appendix A.7.

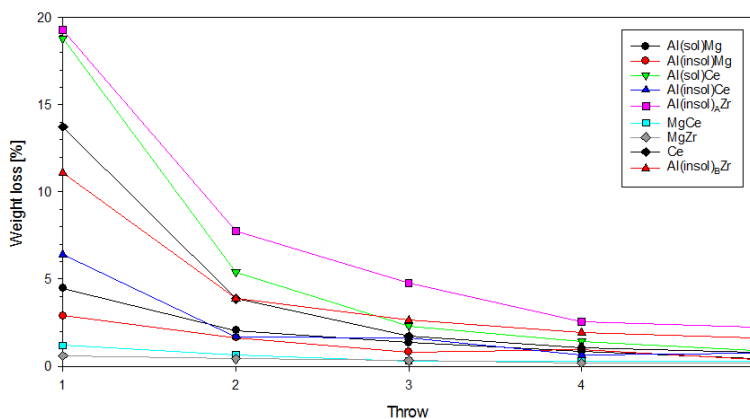


Figure 6.21: The total relative percentage weight loss as a function of drops during the falling test.

From the figure it is observed that the relative weight loss stabilizes at a relatively low level from drop four for all sorbents. Thus, the major difference between the sorbents is during the first drop. The figure shows that the sorbents Al(insol)_AZr, Al(sol)Ce, Ce and Al(insol)_BZr have a relatively high weight loss during the first drop. The weight losses are 19 %, 19 %, 14 % and 11 %, respectively. The weight losses during the first drop for the remaining sorbents, Al(insol)Ce, Al(sol)Mg, Al(insol)Mg, MgCe and Mg_AZr, are on the other hand 6.4 %, 4.5 %, 2.9 %, 1.2 % and 0.59 %, respectively.

It is desirable with a low weight loss of sorbent material during the carbonation-calcination cycles for two reasons. First, it is economically unfeasible to produce sorbents for large-scale industrial application and then suffer the loss of up to 20 % of fully functioning sorbent material with respect to CO₂ capture during the initial phase of operation [19]. Second, the loss of sorbent material is synonymous with formation of fine powders in this case. As mentioned in section 3.2, fine powders in reactors cause problems such as pressure drop and transportation issues.

Both the performance during capturing experiments and the falling test are important with regards to determining an optimal sorbent composition. It is desirable to determine which sorbent that gives a good trade-off between high capturing performance and low material loss. As mentioned, the sorbent Al(sol)Ce has highest cyclic stability from C₁₄ to C₆₈ amongst the group of sorbents containing aluminium from nitrate and cerium. However, this sorbent also had the second highest material loss in the first drop, making it unsuitable for a realistic CO₂ capturing system. On the other hand, the sorbent Al(insol)Mg

showed highest stability amongst the group of the sorbents containing aluminium from cement, while MgZr had highest stability amongst two groups of sorbents, sorbents containing magnesium and zirconium. These sorbents also have the third lowest and lowest weight loss during the first drop, respectively. However, a good performance of sorbents comprises both high capturing capacity and stability over several cycles. The capacities in C₁₄ are comparable for these two sorbents, but the capacities in C₂₈, C₄₂ and C₆₈ for MgZr is noteworthy higher than those for Al(insol)Mg. The values lay around 12 % and 10 %, respectively. This means that the sorbent MgZr had high CO₂ capturing ability, high cyclic stability and low material loss during the falling test. It is observed that this sorbent was stabilized by MgO and CaZrO₃, both of which have one of the highest Tamman temperatures of the stabilizing phases, as seen in Table B.2 in Appendix B.2.

It is emphasized that the granules tested in the falling test were in its oxide form due to the pre-calcination step, and it is uncertain if this is the relevant condition to simulate material losses due to cycling of the sorbents in the reactors. The relevant condition may be oxide form, carbonate form or a combination of these, and it is unknown how the mechanical strength would be in these conditions. Also, as the sorbents undergo carbonation-calcination cycling, they are exposed to temperatures alternating from 570 °C to 950 °C. It is speculated that the resulting thermal stress has impact on the mechanical strength of the sorbents in a real industrial system. The thermal stress has not been taken into account when performing the falling test.

This work has only performed a mechanical falling test, and not attrition tests to investigate the material losses due to non-sphericity of the granules. The focus of this work is to explore the properties of granules with different compositions, and hence, the shape and form of the granules have not been optimized or investigated on microscale.

6.6 N₂ adsorption-desorption analysis and mercury intrusion

The fresh sorbents were analyzed in a N₂ adsorption-desorption measurement twice, as described in section 5.6. This analysis provided information about the specific surface area, pore volume, average pore diameter and porosity, summarized in Table 6.5. The calculation of porosity is given in Appendix A.6. The raw data from the two measurements is given in Table B.9 in Appendix B.6.

Table 6.5: Specific surface area, pore volume, average pore diameter and porosity of the sorbents.

Sorbent	SA [m^2/g]	V_p [cm^3/g]	d_p [nm]	θ [%]
Calcined dolomite	17.6	0.08	18.9	21.9
Al(sol)Mg	6.9 ± 0.5	0.045 ± 0.005	26.6 ± 3.1	12.9 ± 1.3
Al(insol)Mg	7.0 ± 0.3	0.045 ± 0.005	26.6 ± 1.5	13.7 ± 0.8
Al(sol)Ce	6.4 ± 0.9	0.035 ± 0.005	25.5 ± 1.9	9.9 ± 1.3
Al(insol)Ce	7.7 ± 0.6	0.025 ± 0.005	17.0 ± 0.8	7.5 ± 1.2
Al(insol) _A Zr	7.2 ± 0.6	0.025 ± 0.005	17.7 ± 3.2	8.2 ± 0.6
MgCe	4.3 ± 0.4	0.025 ± 0.005	26.8 ± 1.8	7.0 ± 1.0
MgZr	5.6 ± 0.6	0.020 ± 0.000	19.4 ± 0.7	7.0 ± 0.3
Ce	5.9 ± 0.05	0.020 ± 0.000	14.9 ± 0.8	6.0 ± 0.1
Al(insol) _B Zr	8.7 ± 0.3	0.030 ± 0.000	16.8 ± 0.6	8.7 ± 0.0

By comparing the specific surface area and pore volume of calcined dolomite with the sorbents, the general trend is a reduction. This is most likely due to the pre-calcination step which caused sintering, and thus, pore collapse and shrinkage in surface area. As mentioned at the end of section 4.2.2, there should be a positive correlation between activity of a pellet and specific surface area since higher surface area promotes the reaction by uncovering more reaction sites. Y. Hu et al. proposed the same relation between these two parameters as they found that higher specific surface area resulted in better sorbent performance [30]. P. Lan, S. Wu and K. S. Sultana, D. Chen also refer to this relation [28, 34]. Thus, C_1 is plotted against specific surface area in Figure 6.22. The expectation was to discover a positive correlation, but this can not be observed. For example, the sorbent MgCe had the lowest specific surface area and the second highest C_1 , the sorbent Al(insol)_AZr had the third highest specific surface area and the highest C_1 and the sorbent Al(insol)_BZr had the fourth highest specific surface area and the lowest C_1 . Hence, the points have random positions rather than a systematic placement in the graph. Thus, it can be said that a correlation between CO_2 capturing capacity and specific surface area was expected, but this relation was not observed in the relatively narrow range of surface area that the sorbents lay in.

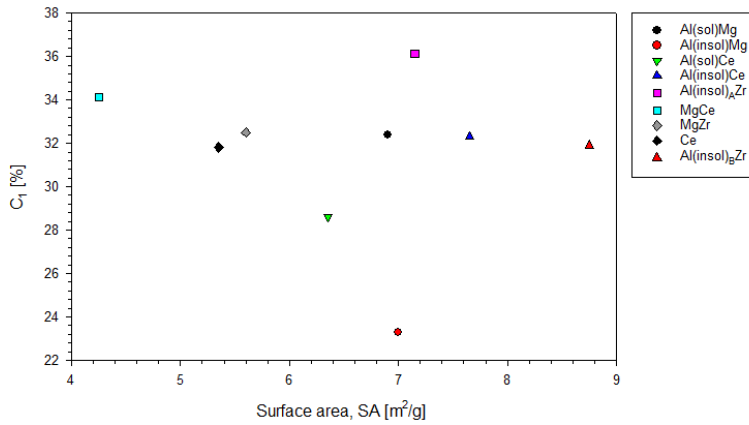


Figure 6.22: C₁ plotted against specific surface area.

A positive correlation was also expected for CO₂ capturing ability and pore volume, as described in section 3.7.2, since a larger pore volume enhances the capturing capacity by providing room for CaCO₃ which have a higher molar volume than CaO. As seen in Table 6.5, the pore volumes lie in the range 0.020-0.045 cm³/g. C₁ is plotted against pore volume in Figure 6.23. As seen in this figure, no correlation exists between these two parameters either. For example, sorbent Al(insol)Mg has the highest pore volume (together with Al(sol)Mg) and the lowest C₁. Thus, it can be said that a positive correlation was expected between these two parameters, but it was not observed for neither surface area or pore volume.

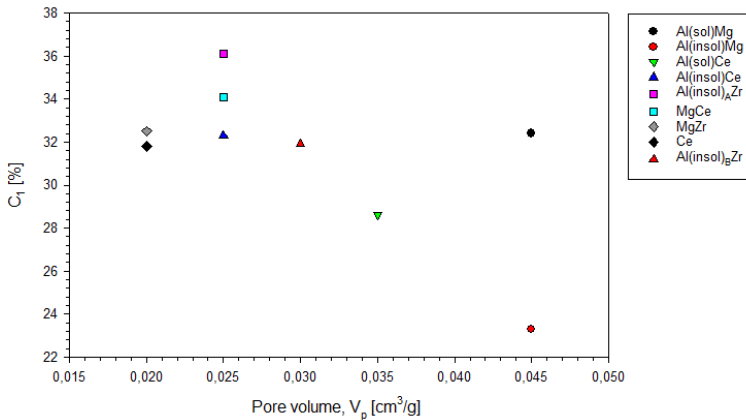


Figure 6.23: C₁ plotted against pore volume.

A positive correlation between relative weight loss during the first drop of the falling test and the porosity of sorbents was expected since a higher porosity generally leads to a lower crushing strength, and hence, a higher weight loss, as mentioned in the last part

of section 4.2.2. Therefore, the relative weight loss in the first drop of the falling test is plotted against porosity in Figure 6.24. Examination of this plot revealed no such relation. For example, the sorbent Ce had the lowest average porosity and the third highest relative weight loss and the sorbent Al(insol)_AZr had the highest relative weight loss and the fifth highest average porosity. Thus, the points in Figure 6.24 are randomly distributed in stead of being located in an orderly manner. Therefore, it can be said that a correlation between the material loss and porosity was expected, but this relation was not observed in the range of porosity that the sorbents belong to. However, it is worth mentioning that the calculated porosity is based on the N₂ adsorption-desorption measurements, and thus, the porosity does not include porosity in the macroporous range. Also, when calculating the porosity, the presence of formed metal oxides was neglected since they are present at a small concentration. The calculated porosity of calcined dolomite was used instead. The sorbents Al(insol)Ce and Al(insol)_AZr were also analyzed using mercury intrusion. The porosity from these measurements accounts for macroporosity. The porosity was 74.9 % and 73.8 %, respectively, which deviates remarkably from the porosity obtained from the N₂ adsorption-desorption measurement which had values in the range 6.0-13.7 %. Thus, the correlation between C₁ and the first drop in the falling test remains uncertain for these sorbents.

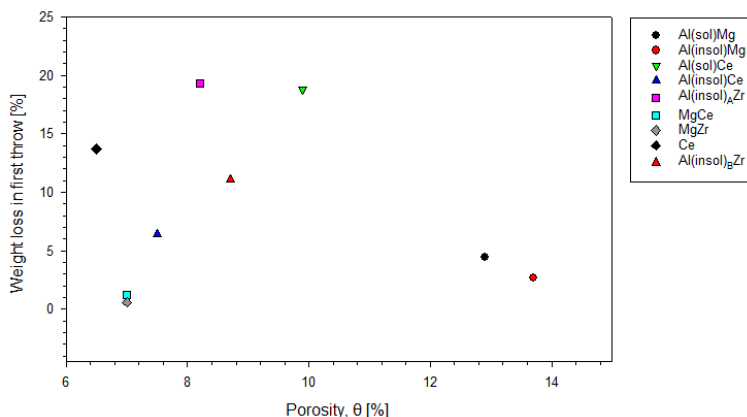


Figure 6.24: The weight loss in the first fall of the falling test plotted against porosity.

The pore size distribution plots for calcined dolomite and the sorbents are presented in Figure 6.25 and 6.26. The shapes of the second pore size distribution plots are similar to the ones mentioned, and are given in Figure B.59 and B.60 in Appendix B.6. The figures have different units for the pore volume, [cm³/g Å] and [cm³/g], due to changes in the analysis program.

Calcined dolomite and the sorbent Ce have slightly bimodal distributions. The peaks are located at a pore diameter of 4 nm and 60 nm with distribution of 3.5-4.5 nm and 25-100 nm for calcined dolomite, while the peaks are located at 4 nm and 50 nm with a distribution of 3-5 nm and 20-100 nm for the Ce-containing sorbent. It is observed that most of the pore volume is related to the larger mesoporous size for these samples. The general feature

of the distribution plots of the remaining sorbents is a monomodal distribution where the maximum peak is located around a pore diameter of 40-60 nm with a distribution within the range 20-100 nm. The pore size distribution can also be observed in SEM pictures of fresh sorbents given in Figure 6.8-6.16. Comparison of the distribution plot for calcined dolomite with the ones for the sorbents shows that no significant shift in maximum have occurred since calcined dolomite have a maximum at pore diameter of 60 nm while the sorbents have a maximum at pore diameters of 40-60 nm. However, the volume associated with this pore diameter is higher for calcined dolomite. The higher volume of calcined dolomite compared with the sorbents is also evident by the values in Table 6.5. Also the micropores present in calcined dolomite disappeared during the synthesis of sorbents. It is suspected that the reason for both these two observations was the pre-calcination step. The reason for the slightly bimodal distribution in the sorbent Ce is uncertain.

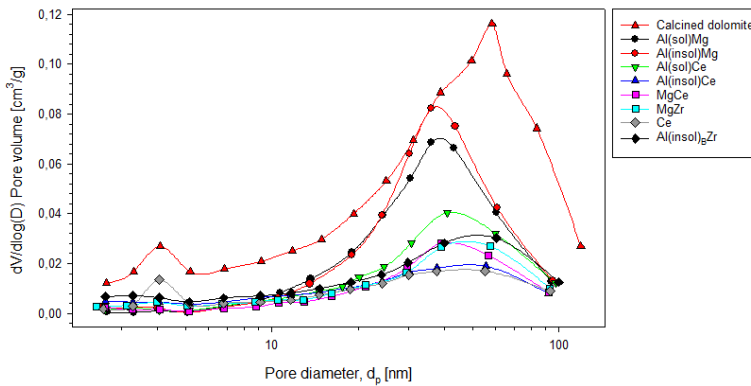


Figure 6.25: Pore size distribution of calcined dolomite, Al(sol)Mg, Al(insol)Mg, Al(sol)Ce, Al(insol)Ce, MgCe, MgZr, Ce and Al(insol)_BZr generated using the desorption branch.

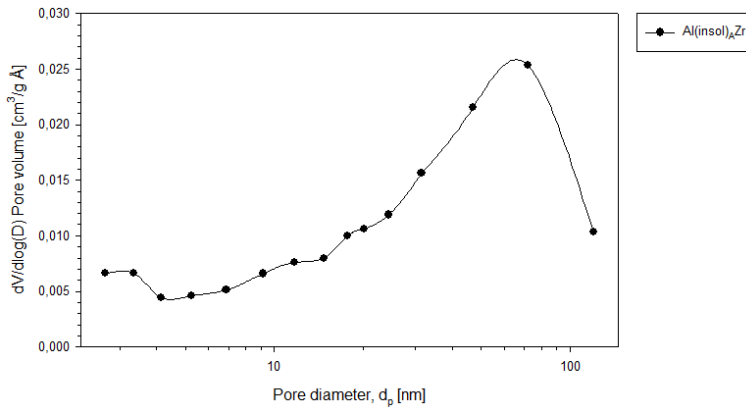


Figure 6.26: Pore size distribution of Al(insol)_AZr generated using the desorption branch.

Calcined dolomite and the fresh sorbents Al(insol)Ce and Al(insol)_AZr were also analyzed

in a mercury intrusion experiment, as mentioned in section 5.7, to investigate the nature of macropores. The pore size distribution plots of these sorbents are presented in Figure 6.27. All samples have a local maximum point at a pore diameter of 4 nm. It is speculated that this was caused by a disturbance in the measurement or pore collapse due to the high pressure applied since mercury intrusion detects macropores, unlike N_2 adsorption-desorption which detects mesopores.

Figure 6.27 shows that calcined dolomite has a global and local maximum at pore diameters of 250 nm and 750 nm. The sorbent Al(insol)Ce has a local and global maximum at pore diameters of 350 nm and 1250 nm. The sorbent Al(insol)₄Zr has a local and global maximum at pore diameters of 400 nm and 1000 nm. Thus, it is observed that the sorbents have a shift in maximum compared to calcined dolomite. It is also observed that the volume associated with these macropores have decreased when comparing calcined dolomite and the sorbents. It is suspected that the general increase in macropore size was caused by the pre-calcination procedure which caused sintering since increasing particle sizes leads to increasing space between the particles [23]. To sum up the results and observations of the pore size distributions from N_2 adsorption-desorption and mercury intrusion, it seems like the pre-calcination step lead to disappearance of micropores, a lower volumetric appearance of mesopores, a lower volumetric appearance of macropores and a shift in pore diameter of macropores.

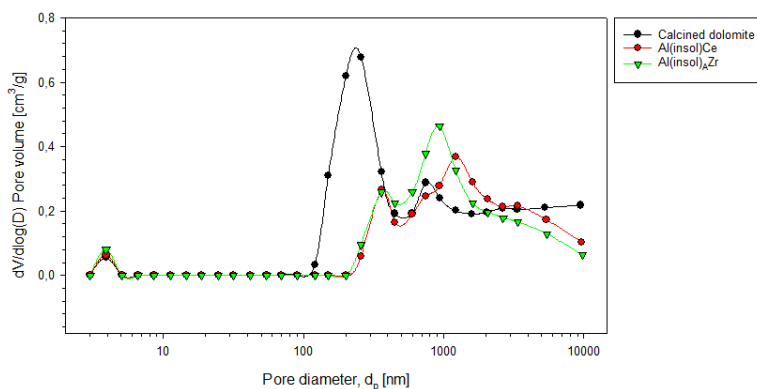


Figure 6.27: The pore size distribution of calcined dolomite and the fresh sorbents Al(insol)Ce and Al(insol)₄Zr from the mercury intrusion measurement.

The N_2 adsorption-desorption measurement also provided the adsorption isotherms. The adsorption isotherms for calcined dolomite and the sorbents Al(sol)Mg and Ce are presented in Figure 6.28. The adsorption isotherms for the remaining sorbents are similar to the one for Al(sol)Mg, so they are presented in Figure B.61-B.69 in Appendix B.6. The unit for adsorbed quantity varies between [cm^3/g STP] and [$mmol/g$]. This was due to changes in the analysis program. However, since the shape of the isotherms is important for the following discussion, and not the values for adsorbed quantity, the unit has not been changed.

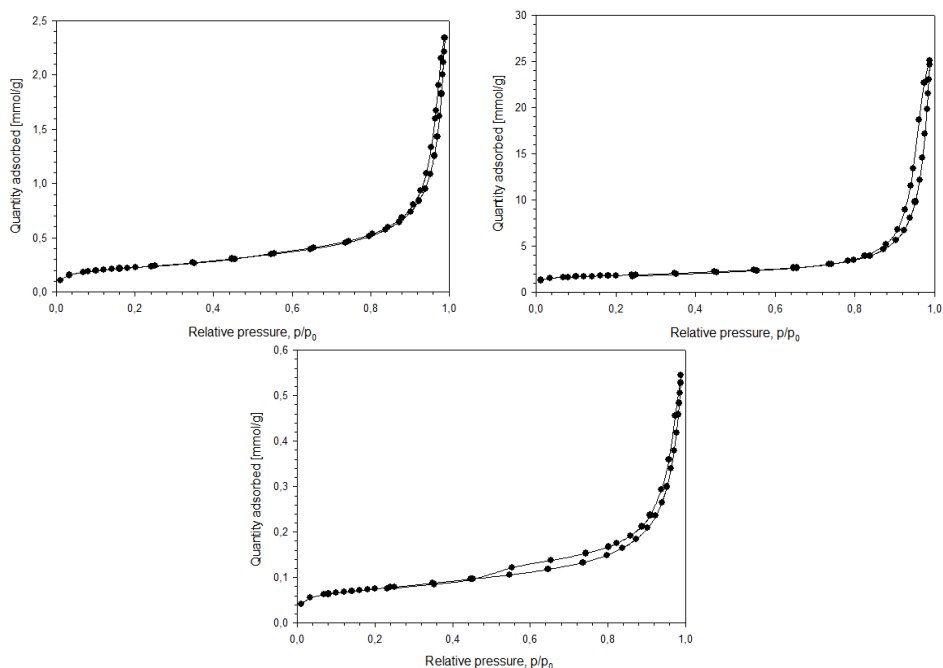


Figure 6.28: The adsorption isotherms for calcined dolomite, Al(sol)Mg and Ce from the N₂ adsorption-desorption measurement.

The experimentally obtained isotherms in Figure 6.28 can be compared with the theoretically isotherms in Figure 4.1. The experimentally obtained isotherms resemble both an isotherm of type II and IV. Due to the presence of a small hysteresis loop, the isotherms were interpreted to be of type IV. This means that the sorbents are mesoporous, and this characterisation is supported by the pore size distribution plots from the N₂ adsorption-desorption measurement and the average pore diameter, which lay in the range 11.2-26.8 nm for the sorbents, presented in Table 6.5.

By comparing the experimentally isotherms with the theoretically hysteresis loops in Figure 4.2, the hysteresis loops were interpreted to be H1 for calcined dolomite and Al(sol)Mg due to the presence of a hysteresis loop at the steep, vertical part of the branch. The hysteresis loop of the sorbent Ce was interpreted to be of type H3 since the loop goes a bit beyond the steep vertical branch towards the more horizontal part.

Theoretically, this analysis indicated that calcined dolomite and all sorbents, except the sorbent Ce, consist of spherical particles which are positioned in a matrix-like structure giving rise to a slim pore size distribution. Also, according to theory, the sorbent Ce contains plate-shaped particles positioned so that the pores are slit-shaped. From the pore size distribution plots in Figure 6.25 and 6.26, it was found that calcined dolomite and the sorbents had a relatively broad pore size distribution, it was in the range 20-100 nm. The deviation from the expected slim pore size distribution may be caused by an interpretation

of the results in this work which deviates from the interpretation other would have made. Examination of the SEM pictures of fresh sorbents in Figure 6.8-6.16 revealed that the sorbents contain both spherical and non-spherical particles in various sizes. However, no plate-shaped particles and slit-shaped pores could be observed in the SEM picture of fresh Ce in Figure 6.15.

6.7 Energy-dispersive x-ray spectrometry (EDS)

EDS pictures were taken for calcined dolomite, Fondu cement, and the sorbents Al(sol)Mg, Al(insol)Mg, Al(insol)₄Zr and MgZr, as described in section 5.8. The pictures are given in Figure 6.29, 6.30, 6.31, 6.32, 6.33 and 6.34. A reoccurring phenomena in these pictures is the overlap between the elements C and Ca and between Al and Br. It is suspected that the detection of carbon was mostly caused by the carbon tape and partly caused by the presence of carbonates. The element Br is not intentionally introduced in any samples, and the detection of this element probably corresponded to the presence of Al since the elemental mapping of Al and Br coincide very well. The elemental map of C and Br is presented in Figure B.70-B.78 in Appendix B.7 since the presence of these elements are irrelevant for the following discussion.

The elemental mapping of calcined dolomite revealed the presence of the elements Ca, C, O and Mg. This was in accordance with the expectation since dolomite and calcined dolomite consist of CaCO₃MgCO₃ and CaOMgO, respectively. The XRD analysis detected both CaO and CaCO₃. The elemental mapping shows a highly homogeneously distribution of the elements.

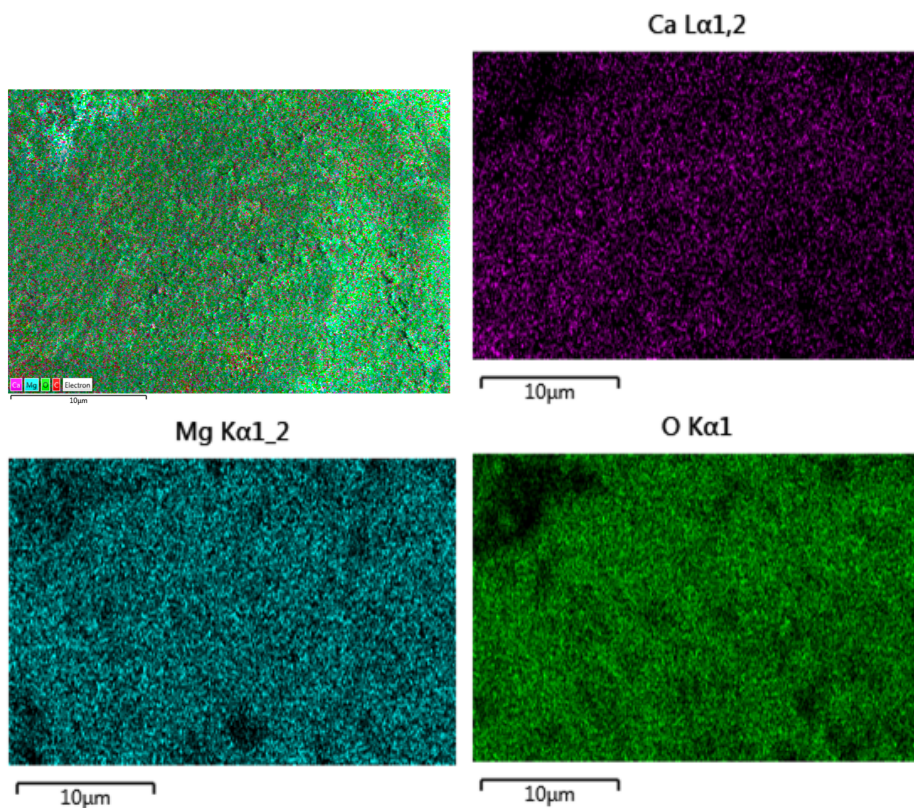


Figure 6.29: Elemental mapping of calcined dolomite. The first picture shows an overview of the area, while the second, third and fourth picture show an elemental mapping of Ca, Mg and O, respectively.

When calculating the amount Fondu cement needed during synthesis to achieve a given weight percent aluminium in the final sorbent, it was assumed that cement only contains CaAl_2O_4 . However, the product data sheet, given in Appendix C, states that the main constituents of Fondu cement are Al_2O_3 , CaO , SiO_2 and Fe_2O_3 . An elemental mapping of Fondu cement was performed to verify the presence of these elements. The elemental mapping detected the elements Ca, C, O, Al, Fe and Si, so this result was in line with the expectation.

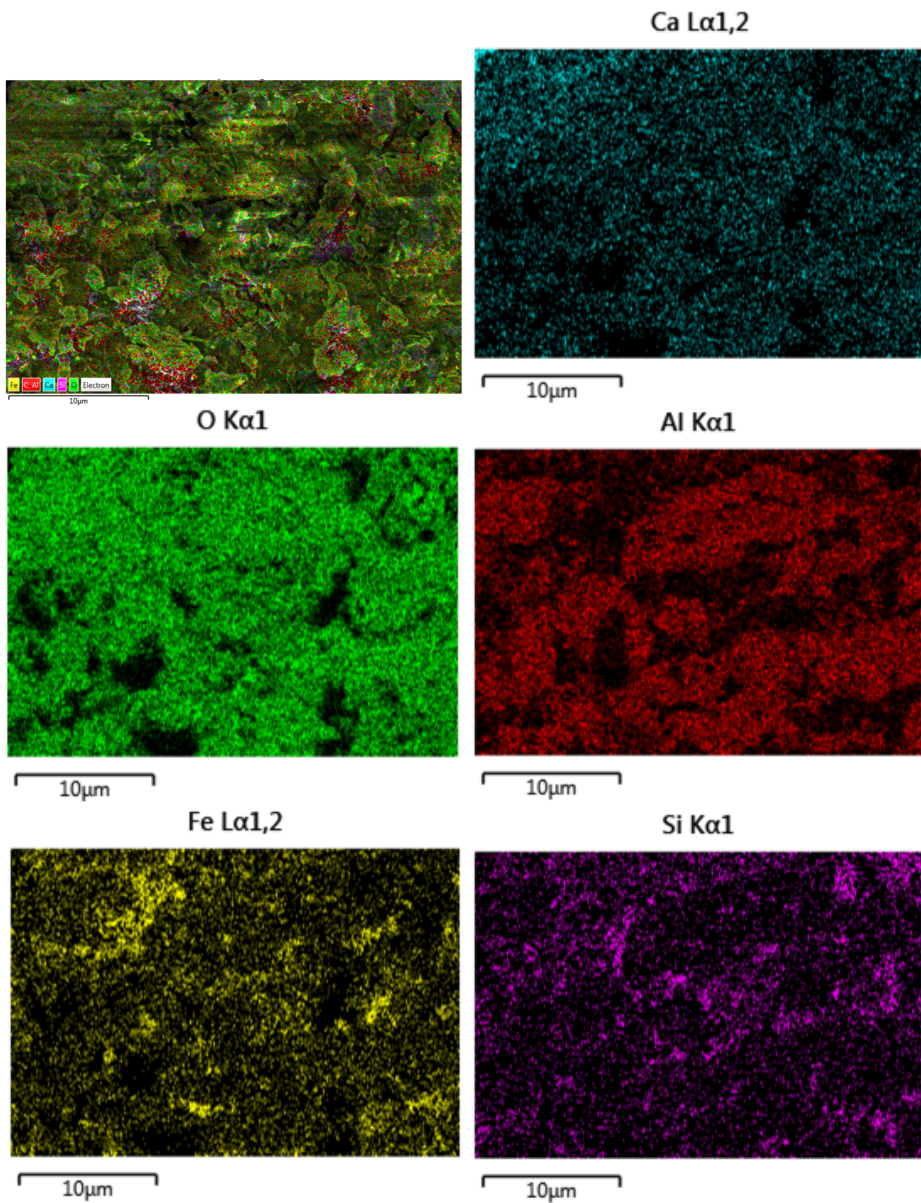


Figure 6.30: Elemental mapping of Fondu cement. The first picture shows an overview of the area, while the second, third, fourth, fifth and sixth picture show an elemental mapping of Ca, O, Al, Fe and Si, respectively.

It has been reported that a well-dispersed inert phase is important to achieve a sorbent with good stability [30, 29]. The uniform distribution would prevent sintering by withstanding crystallite growth and pore collapse. It has been reported that it may be difficult to achieve

a homogeneously distribution of the introduced dopant when using an insoluble precursor [29]. The sorbents Al(sol)Mg and Al(insol)Mg contain the same weight percent of the dopants aluminium and magnesium, but different Al-precursors were utilized during the synthesis. An EDS analysis was performed to explore the distribution of aluminium when using cement and aluminium nitrate.

The elemental mapping of the sorbents Al(sol)Mg and Al(insol)Mg is presented in Figure 6.31 and 6.32. First, the distribution of magnesium was compared to calcined dolomite in Figure 6.29. Calcined dolomite exhibited a highly even distribution of magnesium. The elemental mapping of both Al(sol)Mg and Al(insol)Mg indicated a slightly more uneven distribution of this element. It is observed that the accumulation of magnesium in Al(insol)Mg is somewhat higher than in Al(sol)Mg. The elemental mapping of aluminium in Al(insol)Mg is quite homogeneously, and only small sporadic areas with higher concentration was observed. The elemental mapping of aluminium in Al(sol)Mg revealed that this sorbent had larger areas with higher concentration. A concluding comment to these results and observations is that use of aluminium nitrate actually gave a slightly more uneven distribution of aluminium compared with cement, so this was the opposite of the expectation. Also, comparison of the elemental mapping of the sorbents to calcined dolomite showed that addition of magnesium resulted in a slightly heterogeneously distribution.

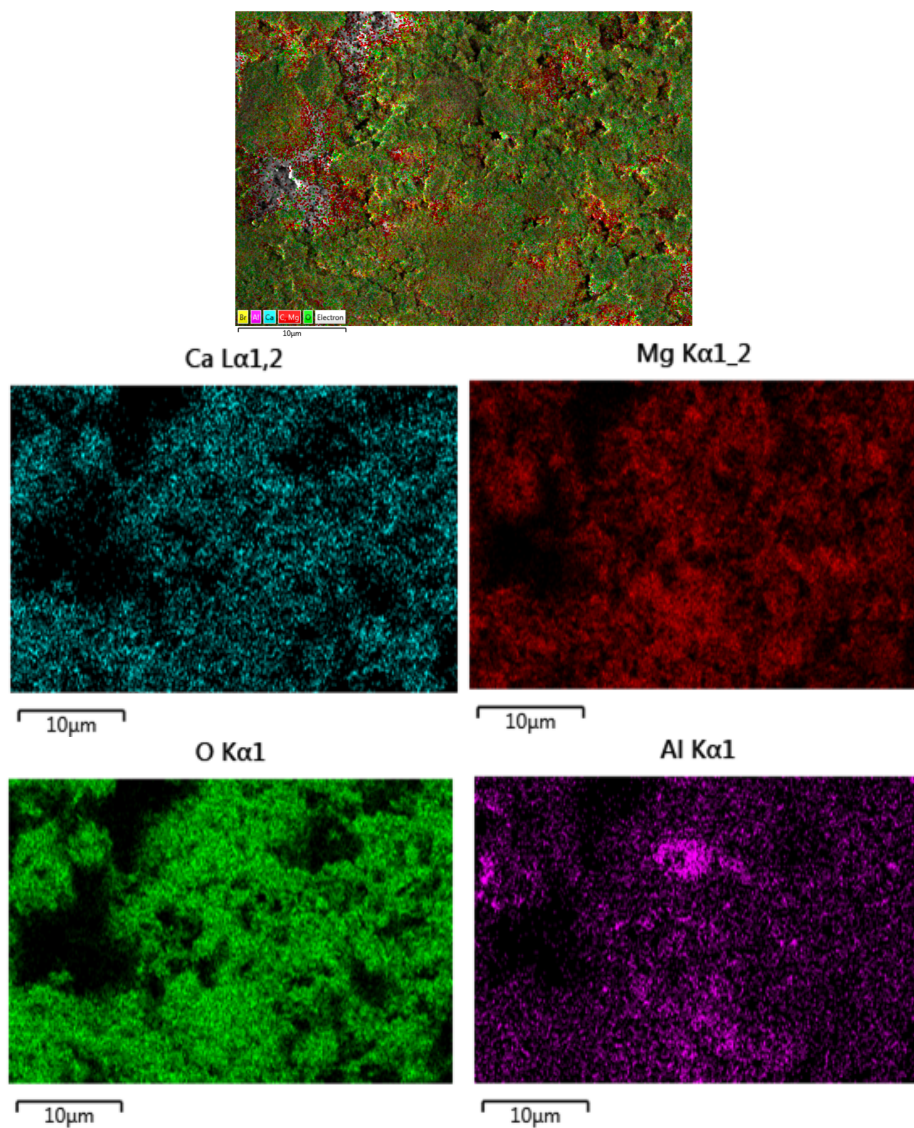


Figure 6.31: Elemental mapping of fresh Al(sol)Mg.

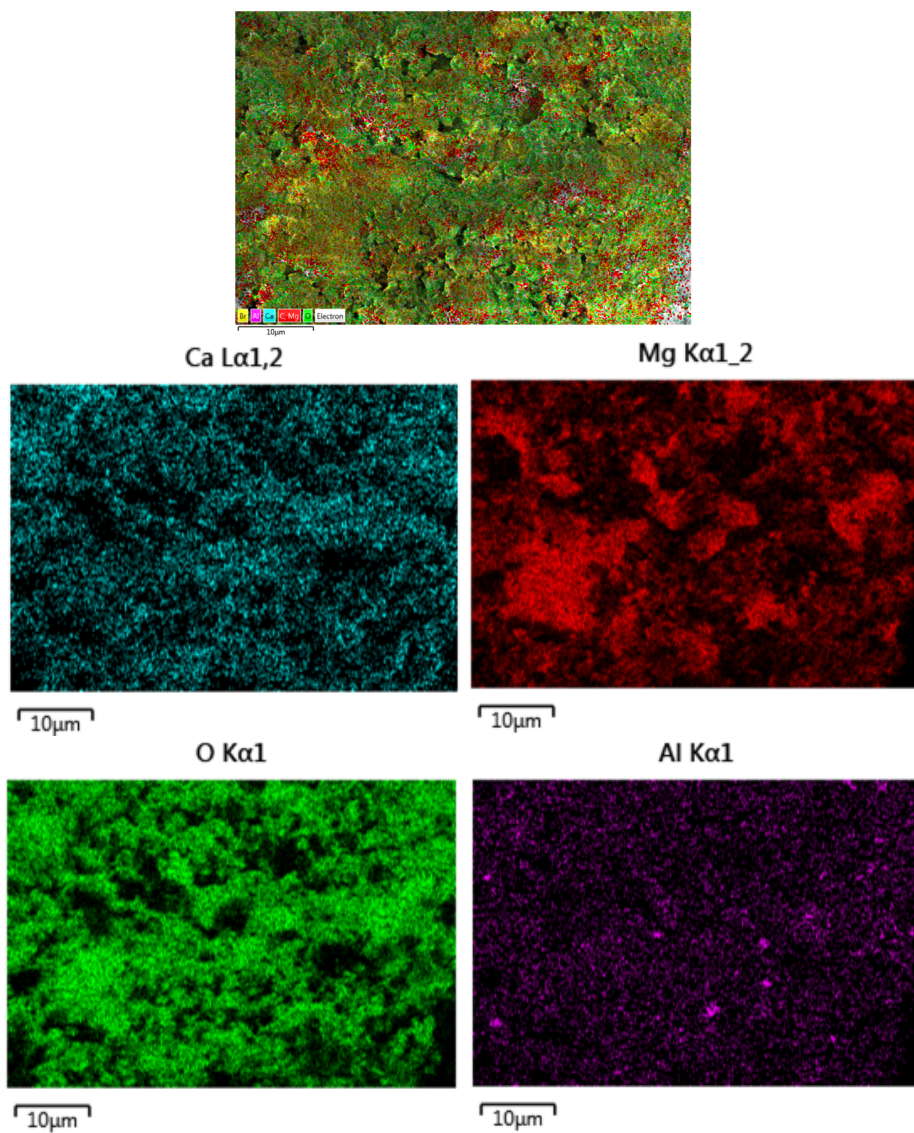


Figure 6.32: Elemental mapping of fresh Al(insol)Mg.

For the same reason as mentioned in the last paragraphs, an elemental mapping of the sorbents Al(insol)_AZr and MgZr were performed since these are the ones with the lowest and highest stability relative to C₁₄, respectively, as can be seen in Table 6.2. It was investigated if the difference in stability could be attributed to the dispersion of dopants. The elemental mapping is presented in Figure 6.33 and 6.34. It is observed from the elemental mapping of the sorbent Al(insol)_AZr that aluminium achieved a homogeneously distribution. This was also the case for the other cement-based sorbent Al(insol)Mg. Zirconium is mostly well-distributed, but the mapping revealed some accumulated areas. The sorbent MgZr had an uniform placement of zirconium throughout the analyzed area. The incorporation of magnesium into this sorbent lead to some areas with higher concentration when compared to the highly even distribution of magnesium in calcined dolomite. Therefore, it was observed that neither the sorbent with lowest or highest cyclic stability had completely homogeneously distributions of the dopants. It is speculated that the difference in cyclic stability is partly affected by the dispersion of dopants and partly by the nature of the stabilizing phase.

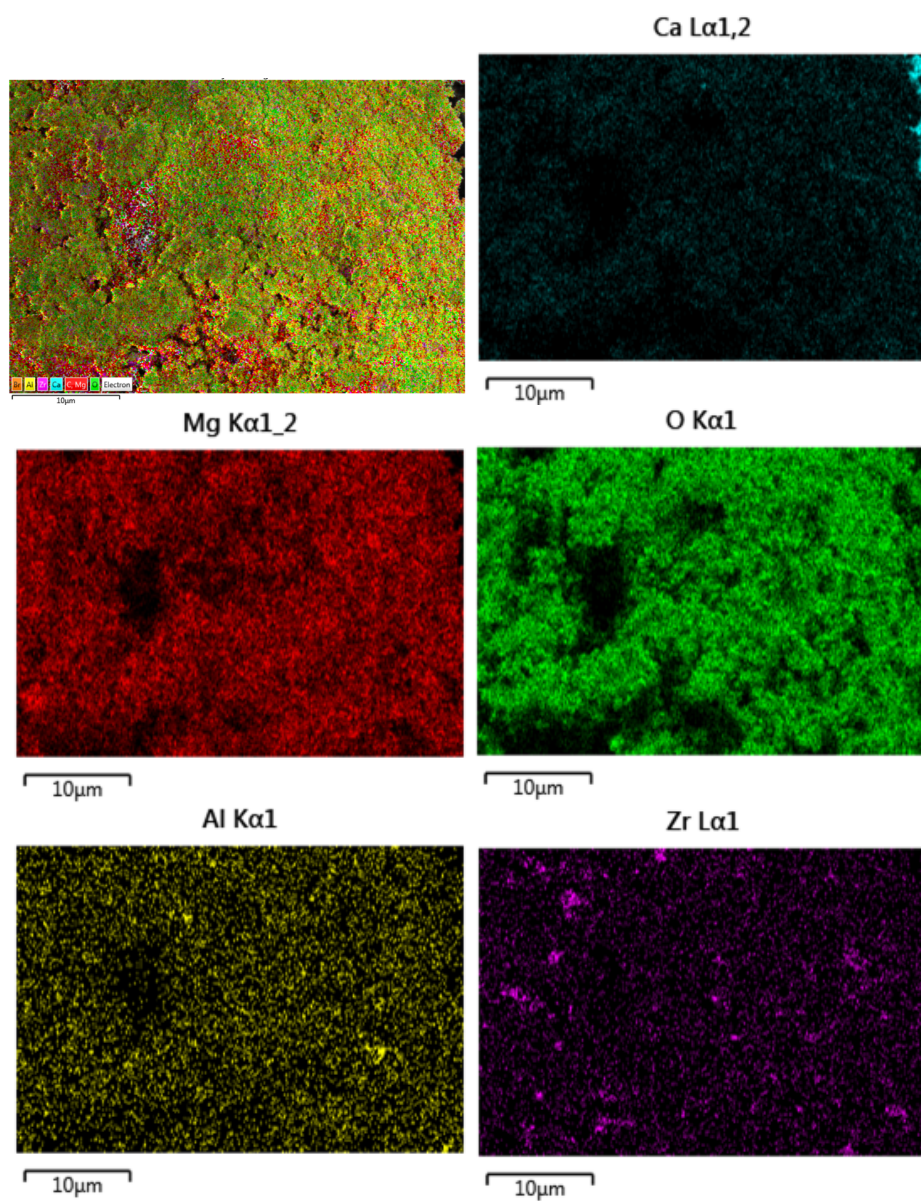


Figure 6.33: Elemental mapping of fresh Al(insol)Zr.

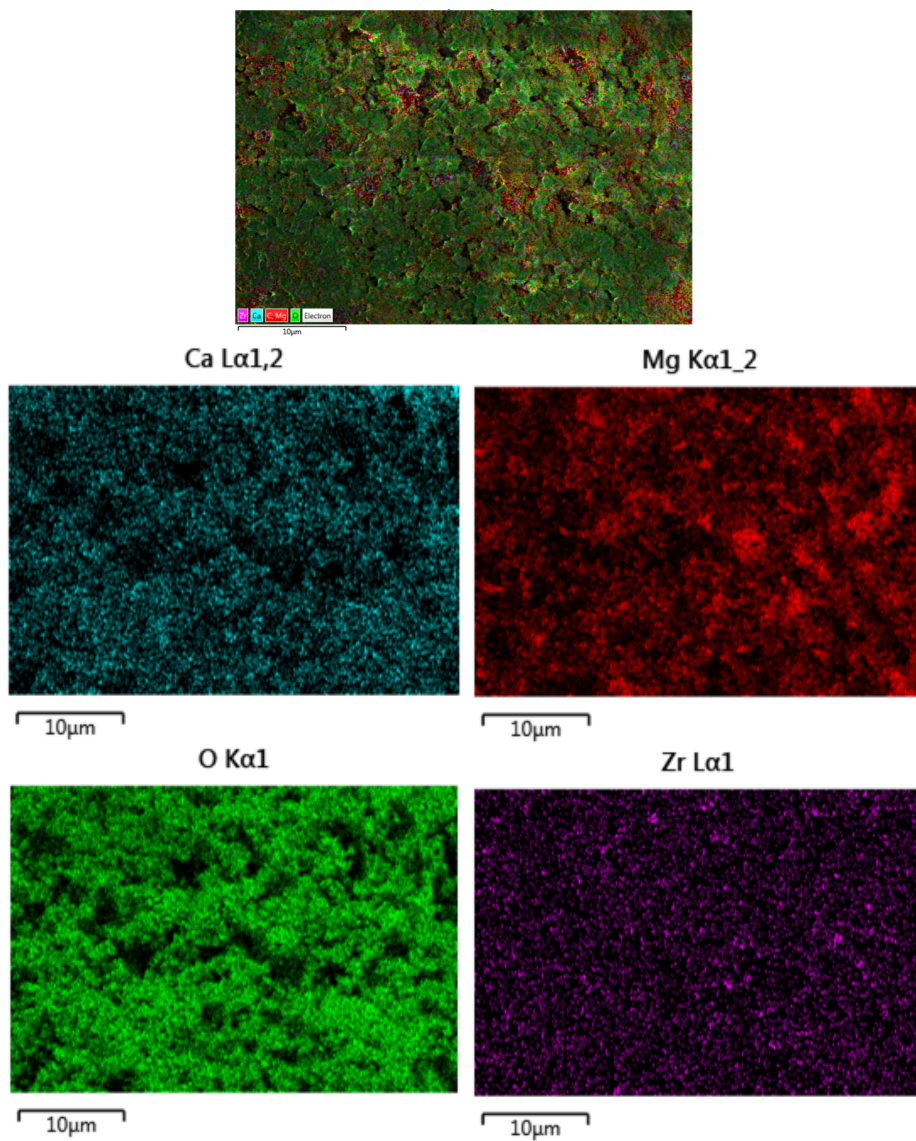


Figure 6.34: Elemental mapping of fresh MgZr.

Fondu cement was utilized as Al-precursor in the sorbents Al(insol)Mg and Al(insol)_AZr. However, the impurities Fe and Si, which was found in the elemental mapping of Fondu cement, could not be detected in these sorbents. The explanation for this may be that Fe₂O₃ and SiO₂ are present in a small amount in Fondu cement (13.0 - 17.5 % Fe₂O₃ and 3.5 - 5.5 % SiO₂ according to the product data sheet). The addition of Fondu cement to calcined dolomite was also small, to the resulting concentration of Fe and Si in the sorbent is small. Thus, the absence of these elements may be due to the sensitivity of the instrument.

Conclusion

During the synthesis of sorbents, it was found that the impregnation of calcined dolomite was not limited by the solubility of the precursors. The precursors zirconium nitrate and powderous cement were easiest to handle during the synthesis since the former was applied as a solution and the latter could be mixed directly with the raw material.

The stabilizing phases formed when introducing Mg, Zr, Al and Ce were MgO, CaZrO₃, Ca₁₂Al₁₄O₃₃ and CeO₂. Comparing the crystallite sizes of CaO and MgO in calcined dolomite with the doped sorbents showed increased sizes in the latter, which indicated sintering in the pre-calcination step. Additional magnesium and CaO-capturing phases in the sorbents did not affect the crystallite sizes of CaO and MgO noteworthy.

The carbonation-calcination cycling in the TGA showed that C₁ for most of the sorbents were comparable since they lay around 30 %. The exception were the sorbents Al(insol)Mg and Al(insol)_AZr which had initial capacity values of 23.3 % and 36.1 %, respectively. It was expected to find a relation between C₁ and specific surface area, and C₁ and pore volume, but it was not observed in the results of this work. It was suspected that this was due to the relatively narrow range both parameters lay in. The pore size distribution plots obtained from the N₂ adsorption-desorption measurements and mercury intrusion revealed that the synthesis of sorbents from calcined dolomite lead to disappearance of micropores, a lower volumetric appearance of both meso- and macropores and a shift in pore diameter of macropores.

The expected correlation between material loss in the first drop of the falling test and porosity could not be observed either. However, the macroporosity of the sorbents were excluded since the porosity was calculated based on the results from the N₂ adsorption-desorption measurement. The porosity of the sorbents Al(insol)Ce and Al(insol)_AZr were 74.9 % and 73.8 % when accounting for the macroporosity as opposed to values in the range 6.0-13.7 % when only the mesoporosity was accounted for. Based on these results, no conclusion can be made regarding correlation between material loss and porosity.

The raw files from the TGA experiments revealed that the captured CO₂ was released during the regeneration step, and the reason for decreasing capacity over several cycles is therefore most likely not because of permanent trapping of CaCO₃ in the pores. SEM pictures revealed differences in the nature of primary particles and pores when comparing fresh and spent sorbents. The pictures showed an increased particle size and a more compact structure for spent sorbents. Therefore, the deactivation mechanism is most likely sintering of CaO-particles which lead to crystallite growth and pore collapse.

The elemental mapping of calcined dolomite showed a highly even distribution of the elements Ca, Mg, O and C, while the elemental mapping of Fondu cement verified the presence of the impurities Fe and Si. An elemental mapping of the sorbents Al(sol)Mg and Al(insol)Mg was performed to investigate the distribution of aluminium when using two different precursors, aluminium nitrate and cement. The elemental mapping showed that the use of the insoluble precursor cement resulted in a slightly more homogeneously distribution of aluminium compared to the soluble precursor aluminium nitrate.

An elemental mapping of the sorbents Al(insol)_AZr and MgZr was performed to investigate if the difference in cyclic stability was attributed to differences in distribution of the dopants. It was found that neither sorbents had a completely homogeneously distribution of dopants. Therefore, it is speculated that the difference in cyclic stability was partly cause by the distribution and partly by the nature of the stabilizing phase.

It is observed that this sorbent was stabilized by MgO and CaZrO₃, both of which have one of the highest Tammann temperatures of the stabilizing phases, as seen in Table B.2 in Appendix B.2.

Three sorbents displayed the overall highest stability from C₁₄ to C₆₈. These three were Al(sol)Ce, Al(insol)Mg and MgZr where the loss in capacity from C₁₄ to C₆₈, L_{14,68}, were 31.6 %, 25.0 % and 11.8 %, respectively. These numbers are relatively low when comparing to the sorbent Al(insol)_AZr which had L_{14,68} = 50.0 %. The Tammann temperatures of the stabilizing phases lay in the range 1275-1483 °C, except for Ca₁₂Al₁₄O₃₃ which has a Tammann temperature of 744 °C. The sorbents with highest stability contain the four stabilizing phases in various combinations, so among these three sorbents it is difficult to see the relation between Tammann temperature and cyclic stability.

It was desirable to determine which sorbent composition that gave a trade-off between sorption performance and material loss. The falling test showed that the material losses stabilized after the fourth drop, and the major difference between the sorbents was during the first drop. Of the three sorbents that exhibited highest stability from C₁₄ to C₆₈, the sorbents Al(insol)Mg and MgZr had the third lowest and lowest material losses during the first drop of the falling test. The material losses were 2.9 % and 0.59 %, as opposed to Al(sol)Ce which had 19 % material loss. By comparing the CO₂ capacities for the sorbents Al(insol)Mg and MgZr, it was observed that C₁₄ was comparable. The capacity of the sorbent MgZr stabilized at 12.2 % in C₂₈, C₄₂ and C₆₈, while the capacities in the same cycles for the sorbent Al(insol)Mg fluctuated at a capacity of 10 %. For these reasons, it was found that the sorbent MgZr exhibited an excellent trade-off between high CO₂ capturing ability, high cyclic stability and low material loss. This sorbent contains 2.8 wt% Mg and 1.9 wt% Zr, so this was found to be the optimal sorbent composition of

the tested sorbents.

Limitations of work

The sorbents were synthesized manually in a mortar. The force and time consume used in the milling process of calcined dolomite and impregnation solution was approximately the same, but there was most likely some small variations. The amount of water added during granulation also differed.

It was not found any relations between the first drop in the falling test and the porosity of the sorbents. Only the mesoporosity was included in the values of porosity since they were calculated based on the results from the N_2 adsorption-desorption measurement. The porosity values lay in the range 6.0-13.7 %, while the porosity of the sorbents $Al(insol)Ce$ and $Al(insol)_AZr$ were 74.9 % and 73.8 % when including the macroporosity. The results were therefore incomplete, and no conclusion could be drawn regarding the relation between the two parameters.

It was concluded that the sorbent $MgZr$ had an exceptional trade-off between the important parameters; cyclic stability, CO_2 sorption capacity and material loss during the first drop of the falling test. The sorbents were in its oxide form when they were dropped in the falling test, and it was uncertain if this is the correct condition to simulate the outcome of the carbonation-calcination cycling. This represents a significant limitation of the work since the conclusion regarding the optimal choice of dopants in the sorbent is partly based on the results from the falling test.

Recommendations

Of the nine synthesized sorbents in this work, it was concluded that the sorbent MgZr had the optimal composition of dopants. In this work, only one sorbent containing both magnesium and zirconium was synthesized, while three other combinations have been synthesized and tested in previous work [54]. It is recommended to synthesize more sorbents containing only aluminium, magnesium or zirconium from the same precursors that were utilized in this work. After this, a second dopant element could be introduced to the basic sorbents and compare the performances. The impact of additional dopants would then be better comprehended.

Research should be performed to determine which conditions the sorbents are exposed to when experiencing mechanical stress in a realistic CO₂ capturing system. A falling test which simulates the same conditions on the sorbents in carbonate form and/or partly carbonated form should be performed to determine a more realistic material loss as a result of sorbent cycling in the reactors.

The amount of spent sorbent after the TGA experiment was 15 mg. It was not enough material to perform characterisation of the spent sorbents, except for SEM pictures which only required small amounts. Therefore, it is recommended to produce bigger batches of sorbents to assure more testing material. Considering that the production of 15 mg spent sorbent lasted for one week, the production should be performed in a reactor set-up which can handle larger amounts of samples. It would be interesting to perform a N₂ adsorption-desorption experiment on spent sorbents to investigate how the cycling has affected specific surface area, pore volume and pore size distribution. It is expected that specific surface area and pore volume have decreased, and that the pore size distribution have experienced a shift in maximum. A XRD analysis would also be of interest to investigate how the crystallite sizes were affected by the cycling. The expectation is to discover an increase in crystallite sizes. It would also be interesting to examine the distribution of elements in spent sorbents using EDS to explore if the cycling has changed the distribution of Ca and the dopants.

The mercury intrusion experiments were expensive, and therefore it is not recommended to characterise more sorbents using this method if it is not of great importance. However, it would be interesting to analyze the sorbent MgZr using mercury intrusion. The results could be compared to the result for the sorbent Al(insol)_AZr since it had the lowest cyclic stability relative to C₁₄, and also the highest material loss, 19 %, during the first drop of the falling test.

Some selected sorbents could be analyzed in the TGA under dry conditions to get a better understanding of the impact of steam in the carbonator. The carbonation-calcination cycling under wet conditions should be extended for MgZr, which is the most promising sorbent.

Bibliography

- [1] E. D. H. R. M. L. P. R. R. J. Sing, K. and T. Siemieniewska, "Reporting physisorption data for gas/solid systems with special reference to the determination of surface area and porosity (recommendations 1984)," *Pure and Applied Chemistry*, vol. 57, no. 4, pp. 611–619, 1985.
- [2] C. H. Bartholomew and R. J. Farrauto, *Catalyst Materials, Properties and Preparation*, ch. 2, pp. 60–117. Wiley-Blackwell, 2010.
- [3] N. Gundersen and N. H. Lundberg, "Petroleum," *Store norske leksikon*, Feb. 2009.
- [4] Miljødirektoratet, "Globale utslipp av klimagasser," *Miljøstatus.no*, 2017.
- [5] Miljødirektoratet, "Karbondioksid (co2)," *Miljøstatus.no*, 2017.
- [6] J. S. Fuglestedt, K. Harstveit, J. Mamen, and R. Benestad, "Klimaendringer," *Store norske leksikon*, 2017.
- [7] K. Hofstad, "Fossilt brensel," *Store norske leksikon*, July 2017.
- [8] IPCC, *IPCC Special Report on Carbon Dioxide Capture and Storage . Prepared by Working Group III of the Intergovernmental Panel on Climate Change*. Cambridge University Press, Cambridge, United Kingdom and New York, 2005.
- [9] L. Mæhlum, "Co2 fangst," *I Store Norske Leksikon*, Mar. 2016.
- [10] M. Wang, A. Lawal, P. Stephenson, J. Sidders, and C. Ramshaw, "Post-combustion co2 capture with chemical absorption: A state-of-the-art review," *Chemical Engineering Research and Design*, vol. 89, no. 9, pp. 1609 – 1624, 2011. Special Issue on Carbon Capture & Storage.
- [11] A. E. Creamer and B. Gao, *Carbon Dioxide Capture: An Effective Way to Combat Global Warming*. Springer International Publishing, 1 ed., 2015.
- [12] Z. Chen, H. S. Song, M. Portillo, J. Lim, J. Grace, and E. Anthony, "Long-term calcination/carbonation cycling and thermal pretreatment for co2 capture by limestone and dolomite," *Energy & Fuels*, vol. 23, pp. 1437–1444, 03 2009.

-
- [13] Y. S. M. X. Wang, S. and J. Gong, "Recent advances in capture of carbon dioxide using alkali-metal-based oxides," *Energy & Environmental Science*, vol. 4, Oct. 2011.
- [14] C. Herce, S. Stendardo, and C. Cortés, "Increasing co₂ carrying capacity of dolomite by means of thermal stabilization by triggered calcination," *Chemical Engineering Journal*, vol. 262, pp. 18 – 28, 2015.
- [15] G. Raade, "Dolomitt," *I Store Norske Leksikon*, May 2017.
- [16] N. Spjeldnæs, "Kalkstein," *I Store Norske Leksikon*, Apr. 2017.
- [17] B. Arstad, A. Lind, K. A. Andreassen, J. Pierchala, K. Thorshaug, and R. Blom, "In-situ xrd studies of dolomite based co₂ sorbents," *Energy Procedia*, vol. 63, pp. 2082 – 2091, 2014. 12th International Conference on Greenhouse Gas Control Technologies, GHGT-12.
- [18] P. Fennell, "1 - calcium and chemical looping technology: An introduction," in *Calcium and Chemical Looping Technology for Power Generation and Carbon Dioxide (CO₂) Capture* (P. Fennell and B. Anthony, eds.), Woodhead Publishing Series in Energy, pp. 3 – 14, Woodhead Publishing, 2015.
- [19] V. Manovic and E. Anthony, "Cao-based pellets supported by calcium aluminate cements for high-temperature co₂ capture," vol. 43, pp. 7117–22, 09 2009.
- [20] A. Coppola, F. Scala, P. Salatino, and F. Montagnaro, "Fluidized bed calcium looping cycles for co₂ capture under oxy-firing calcination conditions: Part 2. assessment of dolomite vs. limestone," *Chemical Engineering Journal*, vol. 231, pp. 544 – 549, 2013.
- [21] P. J. Sun, J. Grace, J. Lim, and E. Anthony, "The effect of cao sintering on cyclic co₂ capture in energy systems," *AIChE Journal*, vol. 53, pp. 2432 – 2442, 09 2007.
- [22] B. Arstad, A. Spjelkavik, K. A. Andreassen, A. Lind, J. Probst, and R. Blom, "Studies of ca-based high temperature sorbents for co₂ capture," *Energy Procedia*, vol. 37, pp. 9 – 15, 2013. GHGT-11 Proceedings of the 11th International Conference on Greenhouse Gas Control Technologies, 18-22 November 2012, Kyoto, Japan.
- [23] M. Erans, V. Manovic, and E. J. Anthony, "Calcium looping sorbents for co₂ capture," *Applied Energy*, vol. 180, pp. 722 – 742, 2016.
- [24] H. Lu, E. P. Reddy, and P. G. Smirniotis, "Calcium oxide based sorbents for capture of carbon dioxide at high temperatures," *Industrial & Engineering Chemistry Research*, vol. 45, no. 11, pp. 3944–3949, 2006.
- [25] G. Busca, "Chapter 4 - practical application and testing of catalytic materials: A synthesis," in *Heterogeneous Catalytic Materials* (G. Busca, ed.), pp. 37 – 56, Amsterdam: Elsevier, 2014.
- [26] I. Chorkendorff and J. W. Niemantsverdriet, "Solid catalysts," in *Concepts of Modern Catalysis and Kinetics* (I. Chorkendorff and J. W. Niemantsverdriet, eds.), ch. 5, pp. 167–214, Wiley-Blackwell, 2005.

-
- [27] Y. Hu, X. Liu, Z. Zhou, W. Liu, and M. Xu, "Pelletization of mgo-based sorbents for intermediate temperature co₂ capture," *Fuel*, vol. 187, pp. 328 – 337, 2017.
- [28] P. Lan and S. Wu, "Mechanism for self-reactivation of nano-cao-based co₂ sorbent in calcium looping," *Fuel*, vol. 143, pp. 9–15, 03 2015.
- [29] H. R. Radfarnia and M. C. Iliuta, "Metal oxide-stabilized calcium oxide co₂ sorbent for multicycle operation," *Chemical Engineering Journal*, vol. 232, pp. 280 – 289, 2013.
- [30] Y. Hu, W. Liu, H. Chen, Z. Zhou, W. Wang, J. Sun, X. Yang, X. Li, and M. Xu, "Screening of inert solid supports for cao-based sorbents for high temperature co₂ capture," *Fuel*, vol. 181, pp. 199 – 206, 2016.
- [31] K. S. Sultana, *Calcium based CO₂ acceptors for sorption enhanced steam reforming*. PhD thesis, Norwegian University of Science and Technology, 2011.
- [32] H. R. Radfarnia and A. Sayari, "A highly efficient cao-based co₂ sorbent prepared by a citrate-assisted sol-gel technique," *Chemical Engineering Journal*, vol. 262, pp. 913 – 920, 2015.
- [33] K. O. Albrecht, K. S. Wagenbach, J. A. Satrio, B. H. Shanks, and T. D. Wheelock, "Development of a cao-based co₂ sorbent with improved cyclic stability," *Industrial & Engineering Chemistry Research*, vol. 47, no. 20, pp. 7841–7848, 2008.
- [34] K. S. Sultana and D. Chen, "Enhanced hydrogen production by in situ co₂ removal on cacezrox nanocrystals," *Catalysis Today*, vol. 171, no. 1, pp. 43 – 51, 2011.
- [35] J. Blamey, E. Anthony, J. Wang, and P. Fennell, "The calcium looping cycle for large-scale co₂ capture," *Progress in Energy and Combustion Science*, vol. 36, no. 2, pp. 260 – 279, 2010.
- [36] F. Donat, N. Florin, E. Anthony, and P. Fennell, "Influence of high-temperature steam on the reactivity of cao sorbent for co₂ capture," *Environmental Science & Technology*, vol. 46, pp. 1262–9, 12 2011.
- [37] I. Lindén, P. Backman, A. Brink, and M. Hupa, "Influence of water vapor on carbonation of cao in the temperature range 400–550 c," *Industrial & Engineering Chemistry Research*, vol. 50, no. 24, pp. 14115–14120, 2011.
- [38] G. Busca, "Chapter 2 - preparation of solid catalysts: A short summary," in *Heterogeneous Catalytic Materials* (G. Busca, ed.), pp. 9 – 22, Amsterdam: Elsevier, 2014.
- [39] M. Eric, C. Xavier, and C. Michel, *Impregnation and Drying*, ch. 4, pp. 59–82. Wiley-Blackwell, 2009.
- [40] R. B. Prime, H. E. Bair, S. Vyazovkin, P. K. Gallagher, and A. Riga, *Thermogravimetric Analysis (TGA)*, ch. 3, pp. 241–317. Wiley-Blackwell, 2008.
- [41] S. K. S. W., R. J., B. G., G. P., V. M., K. D. C., D. A. K., N. J. W., B. T., E. G., M. G.,
-

-
- K. H., and J. H., *Characterization of Solid Catalysts: Sections 3.1.1 – 3.1.3*, ch. 3, pp. 427–582. Wiley-Blackwell, 2008.
- [42] L. P. L., B. Emily, and B. Sandrine, “Surface area/porosity, adsorption, diffusion,” in *Characterization of Solid Materials and Heterogeneous Catalysts* (M. Che and J. C. Védrine, eds.), ch. 19, pp. 853–879, Wiley-Blackwell, 2012.
- [43] S. Lowell and J. E. Shields, *Pore analysis by adsorption*, ch. 8, pp. 54–74. Dordrecht: Springer Netherlands, 1984.
- [44] K. Kaneko, “Determination of pore size and pore size distribution: 1. adsorbents and catalysts,” *Journal of Membrane Science*, vol. 96, no. 1, pp. 59 – 89, 1994.
- [45] P. Liu and G. Chen, “Chapter nine - characterization methods: Basic factors,” in *Porous Materials* (P. Liu and G. Chen, eds.), pp. 411 – 492, Boston: Butterworth-Heinemann, 2014.
- [46] Y. Leng, “X-ray spectroscopy for elemental analysis,” in *Materials Characterization* (Y. Leng, ed.), ch. 6, pp. 191–219, Wiley-Blackwell, 2013.
- [47] J. Linder, “Grunntilstand,” *Store norske leksikon*, 2018.
- [48] Y. Leng, “X-ray diffraction methods,” in *Materials Characterization* (Y. Leng, ed.), ch. 2, pp. 47–82, Wiley-Blackwell, 2013.
- [49] J. W. Niemantsverdriet, “Microscopy and imaging,” in *Spectroscopy in Catalysis* (J. W. Niemantsverdriet, ed.), ch. 7, pp. 179–216, Wiley-Blackwell, 2007.
- [50] Y. Leng, “Scanning electron microscopy,” in *Materials Characterization* (Y. Leng, ed.), ch. 4, pp. 127–161, Wiley-Blackwell, 2013.
- [51] J. W. Niemantsverdriet, “Diffraction and extended x-ray absorption fine structure (exafs),” in *Spectroscopy in Catalysis* (J. W. Niemantsverdriet, ed.), ch. 6, pp. 147–177, Wiley-Blackwell, 2007.
- [52] T. Holtebekk, “Spektroskop,” *Store norske leksikon*, 2018.
- [53] T. Holtebekk, “Røntgendiffraktometer,” *Store norske leksikon*, 2017.
- [54] A. S. Lilleng, “Tkp4580 specialization project: Synthesis of high-temperature solid sorbent for CO₂ capture,” 2017.
- [55] G. Aylward and T. Findlay, *SI Chemical Data*. John Wiley & Sons Australia, 2008.
- [56] R. R. Lourenco, R. A. Simões, and J. d. A. Rodrigues, “Preparation of refractory calcium aluminate cement using the sonochemical process,” *Materials Research*, vol. 16, pp. 731 – 739, 08 2013.

Calculations

A.1 Amount of precursor needed for IWI

The following presents the calculations made to determine the amount of the precursors cement, aluminium nitrate, magnesium nitrate, zirconium nitrate and cerium nitrate needed in order to achieve a given weight percent of the elements in the sorbent.

It is assumed that the final sorbent consists of calcined dolomite and the dopant i . By defining the desired weight percent dopant in the final sorbent, the mass of this dopant in the sorbent is given by

$$m_i = \frac{\omega_i m_{\text{calcined dolomite}}}{1 - \omega_i - \omega_j} \quad (\text{A.1})$$

where m_i is the mass of element i in the sorbent, ω_i is the fractional weight percent of dopant i in the sorbent, $m_{\text{calcined dolomite}}$ is the mass of calcined dolomite and ω_j is the fractional weight percent of dopant $j \neq i$.

The molar amount of dopant i in the sorbent, n_i , is

$$n_i = \frac{m_i}{M_i} \quad (\text{A.2})$$

where M_i is the molecular weight of element i .

The molar amount of the precursor of dopant i in the sorbent, $n_{i,\text{precursor}}$, is

$$n_{i,\text{precursor}} = \alpha n_i \quad (\text{A.3})$$

where α is the stoichiometric coefficient between $n_{i,\text{precursor}}$ and n_i .

The required mass of precursor needed to achieve a defined weight percent of dopant i in the final sorbent,

$$m_{\text{precursor},i} = \frac{n_{i,\text{precursor}} M_{i,\text{precursor}}}{\beta} \quad (\text{A.4})$$

where $M_{i,\text{precursor}}$ is the molecular weight of the precursor for element i and β is the purity of the precursor.

A.2 Nominal weight percent dopant in sorbent

After impregnation of dolomite, the nominal weight percent of elements in the sorbent was calculated. The following will present the method for calculating the actual content of dopants. The abbreviation IS is used for Impregnation Solution.

The total weight of the prepared impregnation solution is

$$m_{\text{IS, tot}} = m_{\text{H}_2\text{O}} + \sum_i^N m_{\text{precursor},i} \quad (\text{A.5})$$

where $m_{\text{H}_2\text{O}}$ is the weight of H_2O added to the precursors to obtain dissolution and $m_{\text{precursor},i}$ is the weight of precursor of element i .

The amount of impregnation solution used for the impregnation is

$$m_{\text{IS,used}} = m_{\text{IS + beaker, tot}} - m_{\text{remains of IS + beaker, tot}} \quad (\text{A.6})$$

where $m_{\text{IS + beaker, tot}}$ is the total weight of the impregnation solution and the beaker, and $m_{\text{remains of IS + beaker, tot}}$ is the weight of the remains of impregnation solution after the impregnation and the beaker.

The weight percent of the precursor for element i in the impregnation solution is

$$w_{\text{precursor},i,\text{IS}} = \frac{m_{\text{precursor},i} \beta}{m_{\text{IS,tot}}} \quad (\text{A.7})$$

where β is the purity of the precursor.

The mass of precursor introduced into calcined dolomite through impregnation is given by multiplication of Equation (A.6) and (A.7),

$$m_{\text{precursor},i,\text{sorbent}} = w_{i,\text{IS}} m_{\text{IS,used}} \quad (\text{A.8})$$

Then the molar amount of precursor introduced into dolomite through impregnation is given by,

$$n_{\text{precursor},i,\text{sorbent}} = \frac{m_{\text{precursor},i,\text{sorbent}}}{M_{i,\text{precursor}}} \quad (\text{A.9})$$

where $M_{i,\text{precursor}}$ is the molecular weight of the precursor of element i .

The molar amount of element i in dolomite as a result of the impregnation is

$$n_{i,\text{sorbent}} = n_{\text{precursor},i,\text{sorbent}} \quad (\text{A.10})$$

The introduction of an element into dolomite leads to formation of an oxide, denoted by MO. The molar amount of MO formed in dolomite is

$$n_{\text{MO},\text{sorbent}} = \alpha n_{i,\text{sorbent}} \quad (\text{A.11})$$

where α is the stoichiometric coefficient between $n_{\text{MO},\text{sorbent}}$ and $n_{i,\text{sorbent}}$.

The mass of oxide MO formed in the sorbent is

$$m_{\text{MO},\text{sorbent}} = n_{\text{MO},\text{sorbent}} M_{\text{MO}} \quad (\text{A.12})$$

where M_{MO} is the molecular weight of the oxide MO.

It is assumed that the final sorbent consists of calcined dolomite and the metal oxides. Then the correct weight percent dopant in the sorbent, $\omega_{i,\text{sorbent}}$, is given by

$$\omega_{i,\text{sorbent}} = \frac{n_{i,\text{sorbent}} M_i}{m_{\text{calcined dolomite}} + \sum_k^N m_{\text{MO},\text{sorbent},k}} \quad (\text{A.13})$$

where M_i is the molecular weight of element i and $\sum_k^N m_{\text{MO},\text{sorbent},k}$ is the sum over mass of oxide k , ..., N present in the sample due to impregnation of element k .

A.3 CO₂ capacity

The definition of CO₂ capacity is,

$$C = \frac{m_{\text{CO}_2}}{\sum_M^k m_{\text{MO}}} \quad (\text{A.14})$$

where m_{CO_2} is the mass of captured CO₂ and $\sum_M^k m_{\text{MO}}$ is the mass of sorbent consisting of metal oxides MO.

The following describes how the CO₂ capacity was calculated using raw data from Linsesis TGA. First, the mass of sorbent in oxide form, $\sum_M^k m_{MO}$, was found using information from the calcination performed in Linseis TGA,

$$\sum_M^k m_{MO} = m_{\text{sorbent prior to cal}} - (m_1 - m_2) \quad (\text{A.15})$$

Here, $m_{\text{sorbent prior to cal}}$ is the mass of sorbent loaded into the Linsesis TGA sample holder prior to calcination, m_1 is the initial mass of sorbent prior to calcination recorded by Linseis TGA and m_2 is the mass of completely calcined sorbent recorded by Linseis TGA. The points m_1 and m_2 are shown in Figure A.1 as an example.

Next, it is assumed that the weight increase of the sorbent in Linseis TGA is due to sorption of CO₂. Thus, the mass of captured CO₂ in cycle i , $m_{CO_2,i}$, is found by,

$$m_{CO_2,i} = m_{T,i} - m_{B,i} \quad (\text{A.16})$$

Here, $m_{T,i}$ is the mass of sorbent at maximum CO₂ sorption in cycle i (subscript T stands for top) and $m_{B,i}$ is the mass of sorbent at complete regeneration in cycle i (subscript B stands for bottom). The points $m_{T,i}$ and $m_{B,i}$ are shown in Figure A.1 as an example. Then the CO₂ capacity is calculated by inserting Equation A.15 and A.16 into Equation A.14.

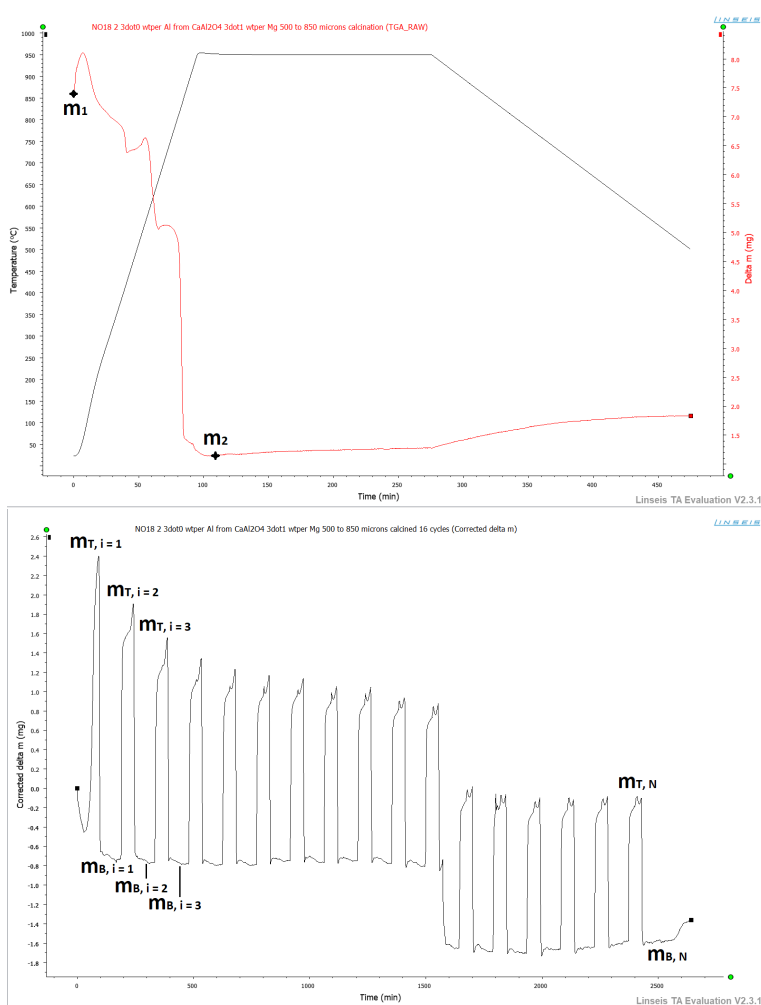


Figure A.1: The top image shows the calcination file for Al(sol)Mg where the points m_1 and m_2 are included as an example for calculation of $\sum_M^k m_{MO}$. The bottom image shows the cyclic CO_2 capture and regeneration of Al(sol)Mg where the points $m_{T,i}$ and $m_{B,i}$ are included as an example for calculation of $m_{\text{CO}_2,i}$.

A.3.1 CO_2 capacity in interval one for Al(sol)Mg

An error was made during the start-up of interval one of the carbonation-calcination cycling for sorbent Al(sol)Mg. The measurement was started without a correction file beneath the raw data. Therefore, values from both the raw data and correction file, given in Figure B.2 and B.3 were used when calculating the CO_2 capacities of interval one.

The calculation followed the same procedure as the one defined in section A.3, but the

nominator of Equation A.14 is in this case,

$$m_{CO_2,i} = (m_{T,i,raw} - m_{B,i,raw}) - (m_{T,i,correction} - m_{B,i,correction}) \quad (A.17)$$

where $m_{T,i,raw}$ and $m_{T,i,correction}$ is the mass at maximum CO₂ capture in cycle i in the raw file and correction file, respectively, and $m_{B,i,raw}$ and $m_{B,i,correction}$ is the mass at complete regeneration in cycle i in the raw file and correction file, respectively.

A.3.2 Pre-calcination file for MgZr

The pre-calcination of MgZr resulted in a raw file which stands out when compared to the pre-calcination raw files of the other sorbents, as seen in Figure B.31. The reason for this is unclear.

The calculation of CO₂ capacities of all intervals for the sorbent MgZr followed the same procedure as the one defined in section A.3, but the denominator of Equation A.14 was in this case,

$$\sum_M^k m_{MO} = m_{\text{sorbent after cal}} - m_{B,1} \quad (A.18)$$

where $m_{\text{sorbent after cal}}$ is the mass of sorbent after the pre-calcination procedure in Linseis TGA and $m_{B,1}$ is the mass of sorbent at complete regeneration in C₁.

A.4 Theoretical maximum CO₂ capacity

The theoretical maximum CO₂ capturing capacity of a sorbent is given by,

$$C_{\max} = \frac{m_{CO_2,\max}}{\sum_M^k m_{MO}} \quad (A.19)$$

where $m_{CO_2,\max}$ is the theoretical maximum mass of CO₂ the sorbent can capture according to Reaction 1.3 in section 1.1 and $\sum_M^k m_{MO}$ is the total mass of sorbent consisting of the metal oxides MO.

The capture of CO₂ takes place according to reaction 1.3, so it is observed that the molar relation between CaO and CO₂ is 1:1. The addition of certain dopants lead to the formation of an inert phase together with CaO. Thus, this molar amount of CaO was not able to participate in the capturing reaction. Therefore, Equation A.19 can be written as,

$$C_{\max} = \frac{(n_{CaO} - \sum_M^n n_{CaMO})M_{CO_2}}{\sum_M^k m_{MO}} \quad (A.20)$$

where n_{CaO} is the molar amount of CaO in the sorbents due to presence of calcined dolomite, $\sum_M^n n_{CaMO}$ is the molar amount of CaO-capturing inert phases and M_{CO_2} is the molecular mass of CO_2 .

A.5 Relative loss in CO_2 capturing capacity

The relative loss in CO_2 capturing capacity from cycle i to cycle j , given as $L_{i,j}$, is calculated by,

$$L_{i,j} = \frac{C_i - C_j}{C_i} \quad (A.21)$$

Here, C_i and C_j are the CO_2 capacity in cycle i and j , respectively, and is found using the approach given in Appendix A.3.

A.6 Porosity from N_2 adsorption-desorption measurement

The following described how the porosity of the sorbents were calculated using results from the N_2 adsorption-desorption measurement. The porosity is defined as,

$$\theta = \frac{V_p}{V_t} = \frac{V_p}{V_s + V_p} \quad (A.22)$$

where θ is the porosity, V_p is the pore volume, V_s is the volume of compact solid and V_t is the total volume of the porous material [45].

The pore volume, V_p , can be found from the isotherm report. The pores of the sorbents are completely filled when the relative pressure is approximately 1, $p/p_0 \approx 1$. The isotherm report provides the value for quantity adsorbed N_2 as cm^3/g STP at $p/p_0 \approx 1$, v_{ads} . Assuming that N_2 is an ideal gas, the number of moles N_2 adsorbed, $n_{N_2,ads}$, can be calculated using the ideal gas law,

$$n_{N_2,ads} = \frac{Pv_{ads}}{RT} \quad (A.23)$$

where R is the universal gas constant, and P and T are standard pressure and temperature, respectively.

Number of moles gaseous N_2 adsorbed equals number of moles liquid N_2 filling the pores,

$$n_{N_2,ads} = n_{N_2} \quad (A.24)$$

The mass of liquid N_2 present in the pores is given by,

$$m_{N_2} = n_{N_2} M_{N_2} \quad (\text{A.25})$$

where M_{N_2} is the molecular mass of N_2 .

Then the volume of liquid N_2 filling the pores is given by,

$$V_{N_2(l)} = \frac{m_{N_2(l)}}{\rho_{N_2}} \quad (\text{A.26})$$

where ρ_{N_2} is the density of N_2 . V_{N_2} is equal to the pore volume of the material, V_p .

$$V_p = V_{N_2} \quad (\text{A.27})$$

The volume of compact material, V_s , can be found by,

$$V_s = \frac{1}{\rho_{\text{sorbent}}} \quad (\text{A.28})$$

where ρ_{sorbent} is the material density of the sorbent. The sorbents have been doped with the elements Mg, Zr, Al and Ce, and thus, contain inert phases containing these elements. However, these inert phases have been neglected when calculating ρ_{sorbent} since they are present in small amounts. Therefore, ρ_{sorbent} was calculated based on the assumption that the sorbents contain only CaO and MgO, present in a molar relationship of 1:1. The following presents the calculation to determine ρ_{sorbent} .

The mole fractions of CaO and MgO in calcined dolomite are x_{CaO} and x_{MgO} , respectively. The total molar amount of calcined dolomite is $n_{\text{calcined dolomite}}$. Then the molar amount of compound i , n_i , in calcined dolomite is,

$$n_i = x_i n_{\text{calcined dolomite}} \quad (\text{A.29})$$

where $i = \{\text{CaO, MgO}\}$. The mass of compound i , m_i , in calcined dolomite is given by,

$$m_i = n_i M_i \quad (\text{A.30})$$

where M_i is the molecular mass of compound i . The mass fraction of compound i in calcined dolomite, ω_i , is given by,

$$\omega_i = \frac{m_i}{\sum_{i=1}^N m_i} \quad (\text{A.31})$$

where $\sum_{i=1}^N m_i$ is the total mass of calcined dolomite. Then, the calculated material density of calcined dolomite is given by,

$$\rho_{\text{sorbent}} = \sum_{i=1}^N \omega_i \rho_i \quad (\text{A.32})$$

where ρ_i is the density of compound i .

Finally, since V_p is known from Equation A.27 and V_s is known from Equations A.28 and A.32, the porosity of the sorbent can be found from Equation A.22.

A.7 Total relative percentage weight loss during the falling test

The total relative material loss during the falling test is given by,

$$\text{Total relative weight loss} = \frac{m_{\text{tot},i} - m_{\text{tot},i+1}}{m_{\text{tot},i}} \quad (\text{A.33})$$

where $m_{\text{tot},i}$ and $m_{\text{tot},i+1}$ is the total mass of sorbents being dropped down the tube in drop i for $i = \{1,2,3,4\}$. For $i = 5$, the total relative material loss was found by,

$$\text{Total relative weight loss} = \frac{m_{\text{tot},5} - (m_{\text{tot},5} - m_{\text{tot res},5})}{m_{\text{tot},5}} \quad (\text{A.34})$$

where $m_{\text{tot res},5}$ is the total mass of residue produced after dropping sorbents with mass $m_{\text{tot},5}$ down the tube.

The total mass of sorbents being dropped down the tube in throw i is given by,

$$m_{\text{tot},i} = m_{250-500\mu\text{m},i} + m_{500-850\mu\text{m},i} \quad (\text{A.35})$$

where $m_{250-500\mu\text{m},i}$ and $m_{500-850\mu\text{m},i}$ are the mass of sorbents with size 250-500 μm and 500-850 μm , respectively, being dropped separately down the tube in throw i . These values are given in Table B.7 and B.8 in Appendix A.7 as $m_{\text{sample } 250-500\mu\text{m}}$ and $m_{\text{sample } 500-850\mu\text{m}}$, respectively.

The total mass of residue produced after dropping sorbents with mass $m_{\text{tot},5}$ down the tube is found by,

$$m_{\text{tot res},5} = m_{\text{res}<250\mu\text{m},5} + m_{\text{res}<500\mu\text{m},5} \quad (\text{A.36})$$

where $m_{\text{res}<250\mu\text{m},5}$ and $m_{\text{res}<500\mu\text{m},5}$ is the mass of residue produced when dropping $m_{250-500\mu\text{m},5}$ and $m_{500-850\mu\text{m},5}$ down the tube. These values are given in Table B.7 and B.8 in Appendix A.7 as $m_{\text{residue}<250\mu\text{m}}$ and $m_{\text{residue}<500\mu\text{m}}$, respectively.

Appendix B

Raw data

B.1 Synthesis of sorbents

Table B.1: The amount of precursors and distilled H₂O used for preparation of impregnation solutions, the total amount of impregnation solution used for impregnation and amount of distilled H₂O used for granulation.

Sorbent	$m_{\text{precursor } i}$	$m_{\text{precursor } j}$ [g]	$m_{H_2O, \text{impreg sol}}$ [g]	$m_{\text{impreg sol, used}}$ [g]	$m_{H_2O, \text{granulation}}$ [g]
Al(sol)Mg	8.8741	6.9603	3.4991	19.2871	6.0678
Al(insol)Mg	1.8700*	6.9643	3.5210	12.2436	9.0639**
Al(sol)Ce	8.8786	1.9094	4.6695	15.3475	9.3488
Al(insol)Ce	1.8660*	1.9076	6.9858	10.4340	8.2395
Al(insol) _A Zr	1.8411*	3.2473	5.8779	9.0959	10.2343
MgCe	6.9619	1.9122	6.0713	14.3277	7.7264
MgZr	6.8919	3.2089	7.1862	16.1257	4.9520
Ce	1.8540	-	10.7380	12.5152	7.3608
Al(insol) _B Zr	4.1676*	2.9087	3.1016	6.7106	8.8510

*Amount of insoluble CaAl₂O₄.

** This number is not correct. The beaker with distilled water was shoved during granulation.

B.2 Tammann temperature

Table B.2: The melting temperature, T_m , and Tammann temperature, T_T , of the stabilizing phases.

Compound	T_m [°C]	T_T [°C]
CaO	2927 [55]	1522
MgO	2852 [55]	1483
CaZrO ₃	2452	1275 [31]
CeO ₂	2600 [55]	1352
Ca ₁₂ Al ₁₄ O ₃₃	1430 [56]	744

B.3 Thermogravimetric analysis (TGA)

B.3.1 Al(sol)Mg

Calcination

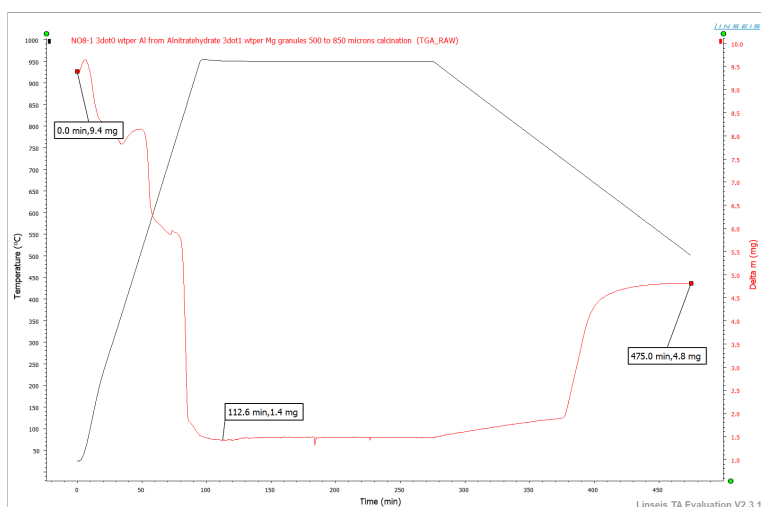


Figure B.1: Raw data, without correction, from calcination of the sorbent Al(sol)Mg in Linseis TGA.

Cyclic CO₂ capture and regeneration

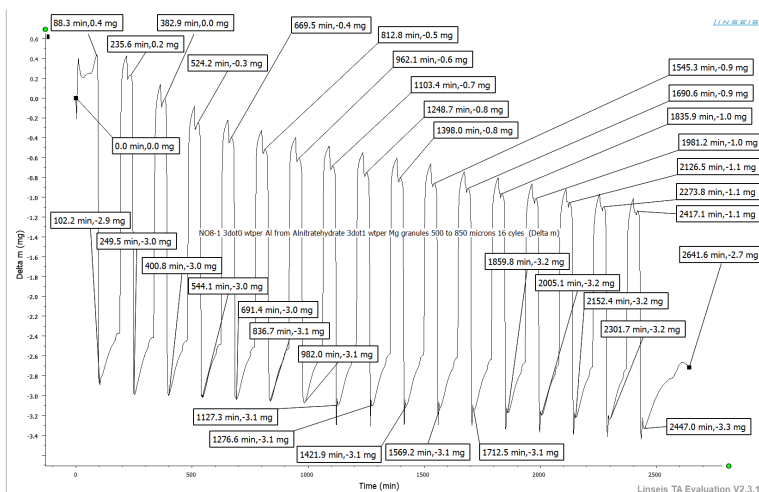


Figure B.2: Raw data, without correction, from the CO₂ capturing experiment performed in Linseis TGA for the sorbent Al(sol)Mg. The picture shows C₁ to C₁₇.

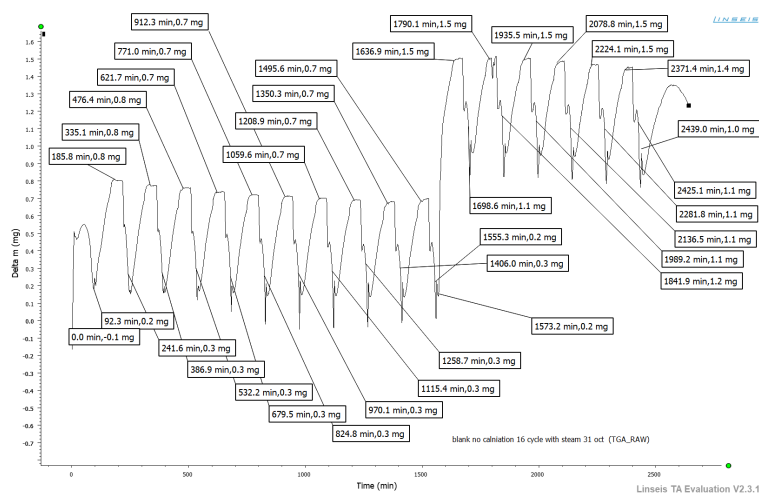


Figure B.3: The correction curve used for all measurements of cyclic CO₂ capture and regeneration. The values in this correction curve was used together with values from Figure B.2 to find corrected values for C₁ to C₁₇.

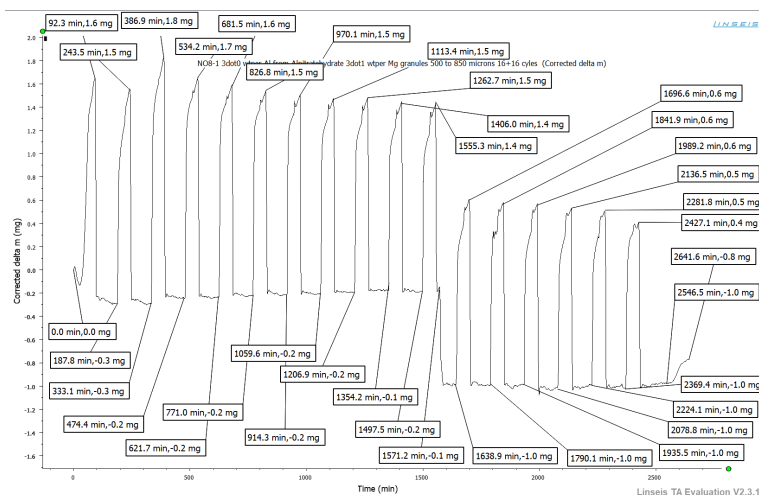


Figure B.4: Raw data from the CO₂ capturing experiment performed in Linseis TGA for the sorbent Al(sol)Mg. The picture shows C₁₈ to C₃₄.

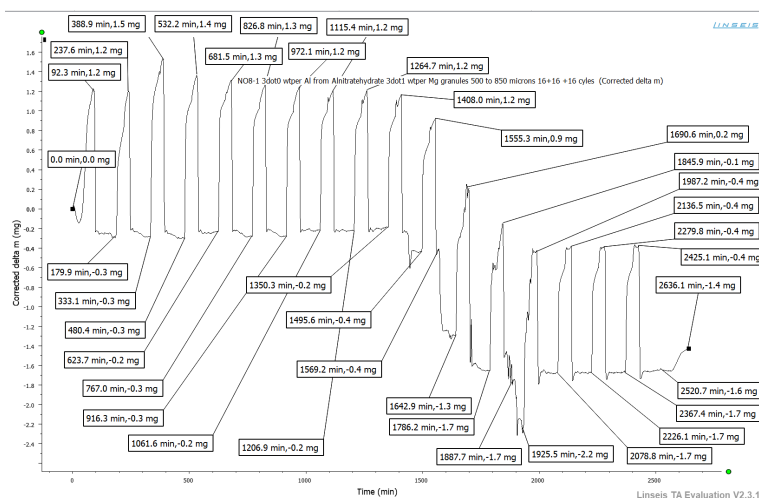
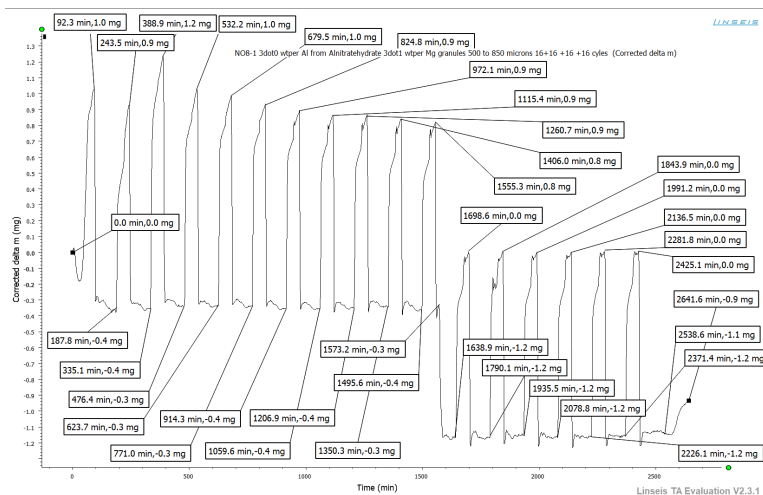


Figure B.5: Raw data from the CO₂ capturing experiment performed in Linseis TGA for the sorbent Al(sol)Mg. The picture shows C₃₅ to C₅₁.



Cyclic CO₂ capture and regeneration

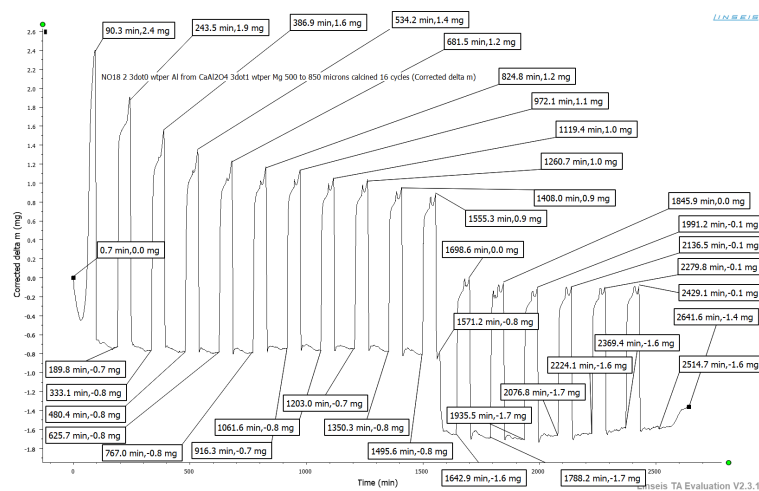


Figure B.8: Raw data from the CO₂ capturing experiment performed in Linseis TGA for the sorbent Al(insol)Mg. The picture shows C₁ to C₁₇.

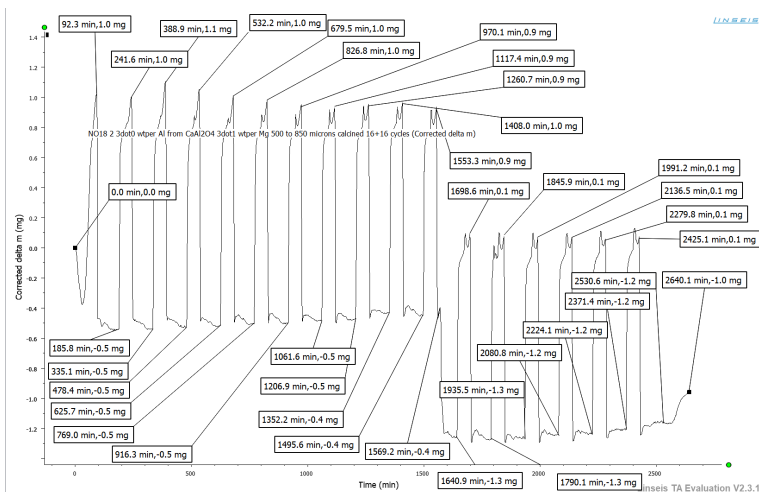


Figure B.9: Raw data from the CO₂ capturing experiment performed in Linseis TGA for the sorbent Al(insol)Mg. The picture shows C₁₈ to C₃₄.

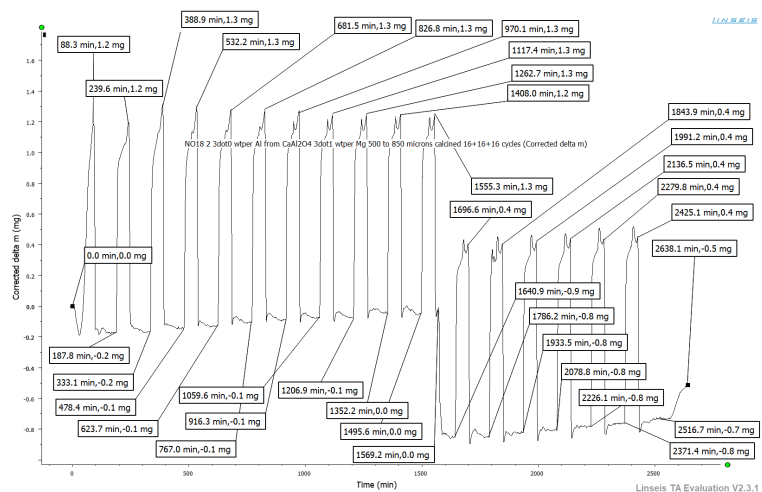


Figure B.10: Raw data from the CO₂ capturing experiment performed in Linseis TGA for the sorbent Al(insol)Mg. The picture shows C₃₅ to C₅₁.

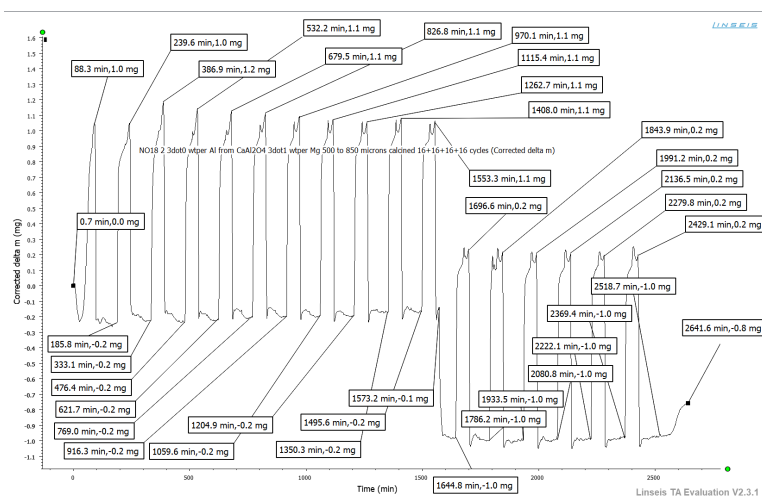


Figure B.11: Raw data from the CO₂ capturing experiment performed in Linseis TGA for the sorbent Al(insol)Mg. The picture shows C₅₂ to C₆₈.

B.3.3 Al(sol)Ce

Calcination

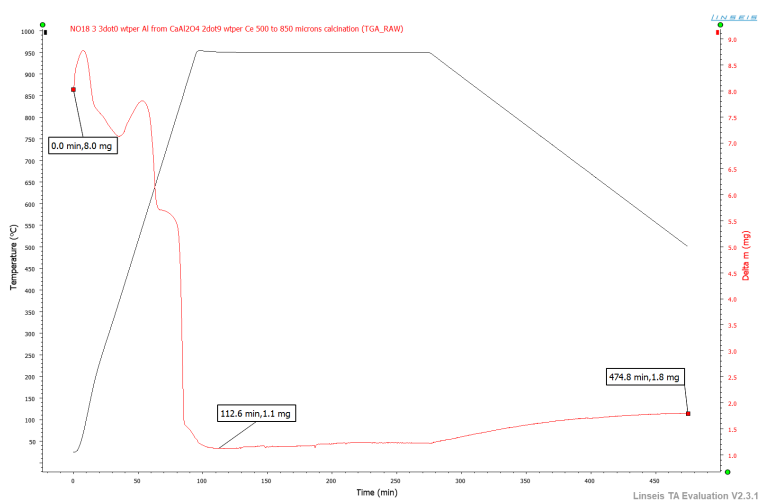


Figure B.12: Raw data, without correction from calcination of the sorbent Al(sol)Ce in Linseis TGA.

Cyclic CO₂ capture and regeneration

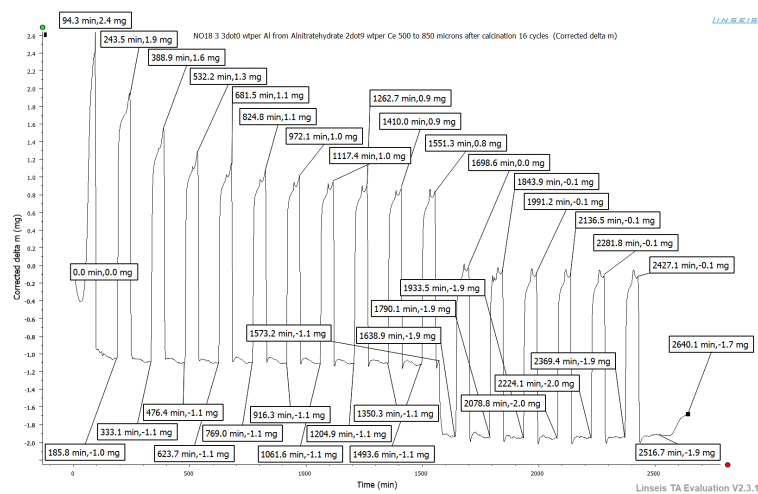


Figure B.13: Raw data from the CO₂ capturing experiment performed in Linseis TGA for the sorbent Al(sol)Ce. The picture shows C₁ to C₁₇.

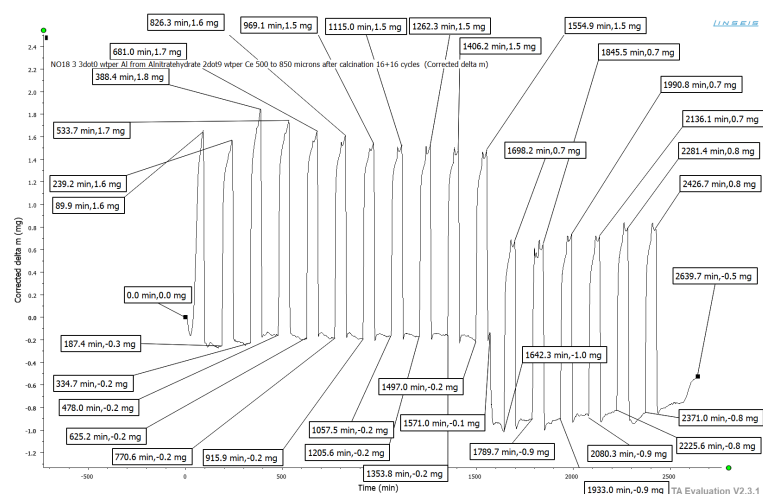


Figure B.14: Raw data from the CO₂ capturing experiment performed in Linseis TGA for the sorbent Al(sol)Ce. The picture shows C₁₈ to C₃₄.

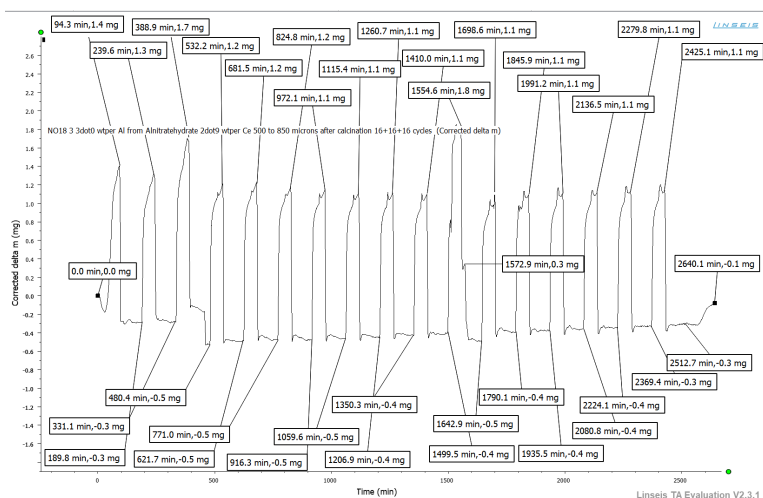


Figure B.15: Raw data from the CO₂ capturing experiment performed in Linseis TGA for the sorbent Al(sol)Ce. The picture shows C₃₅ to C₅₁.

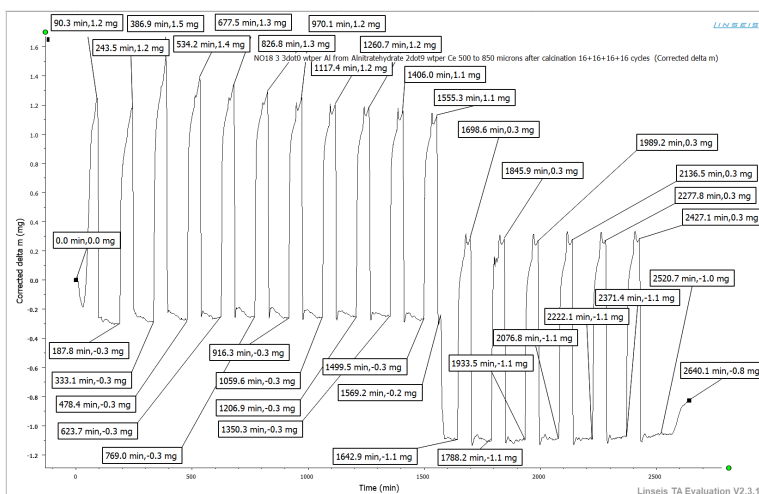


Figure B.16: Raw data from the CO₂ capturing experiment performed in Linseis TGA for the sorbent Al(sol)Ce. The picture shows C₅₂ to C₆₈.

B.3.4 Al(insol)Ce

Calcination

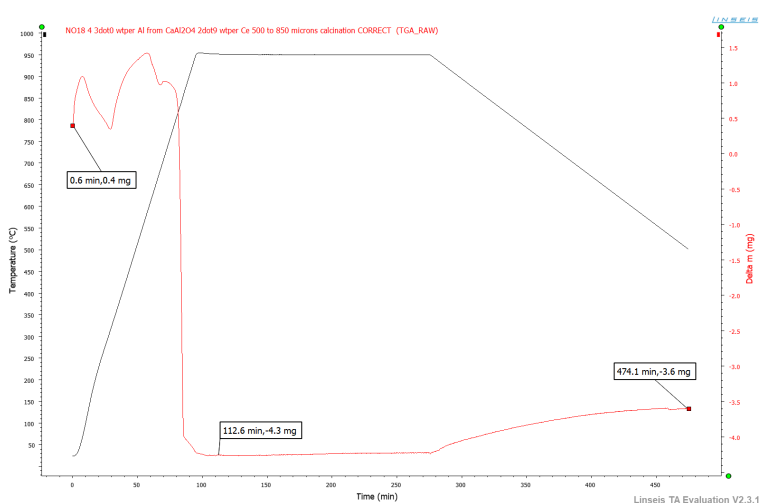


Figure B.17: Raw data, without correction, from calcination of the sorbent Al(insol)Ce in Linseis TGA.

Cyclic CO₂ capture and regeneration

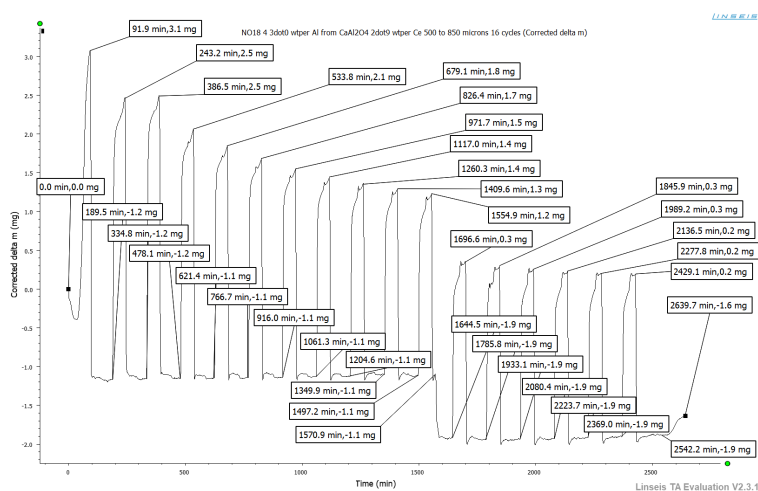


Figure B.18: Raw data from the CO₂ capturing experiment performed in Linseis TGA for the sorbent Al(insol)Ce. The picture shows C₁ to C₁₇.

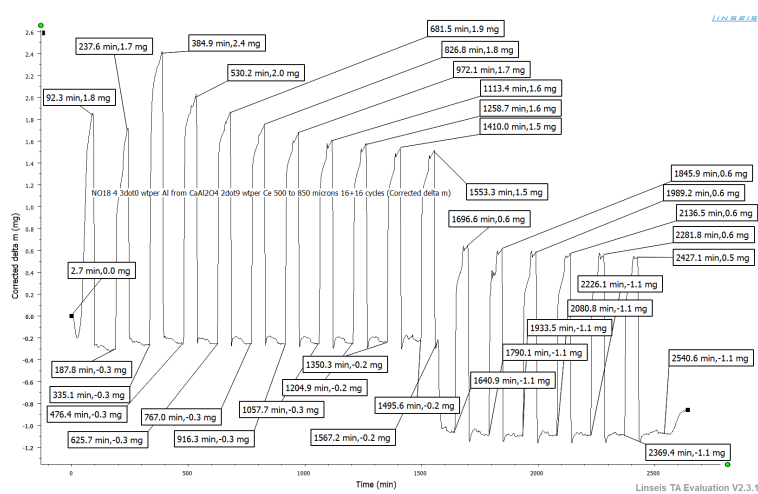


Figure B.19: Raw data from the CO₂ capturing experiment performed in Linseis TGA for the sorbent Al(insol)Ce. The picture shows C₁₈ to C₃₄.

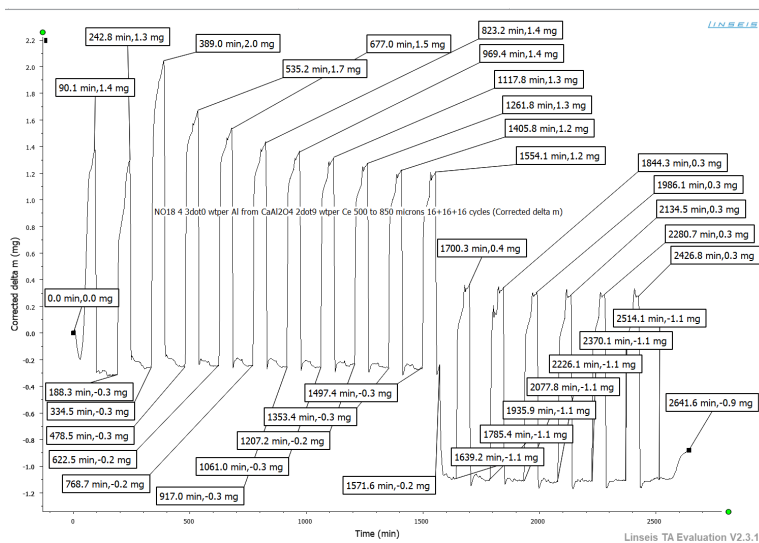


Figure B.20: Raw data from the CO₂ capturing experiment performed in Linseis TGA for the sorbent Al(insol)Ce. The picture shows C₃₅ to C₅₁.

B.3.5 Al(insol)_AZr

Calcination

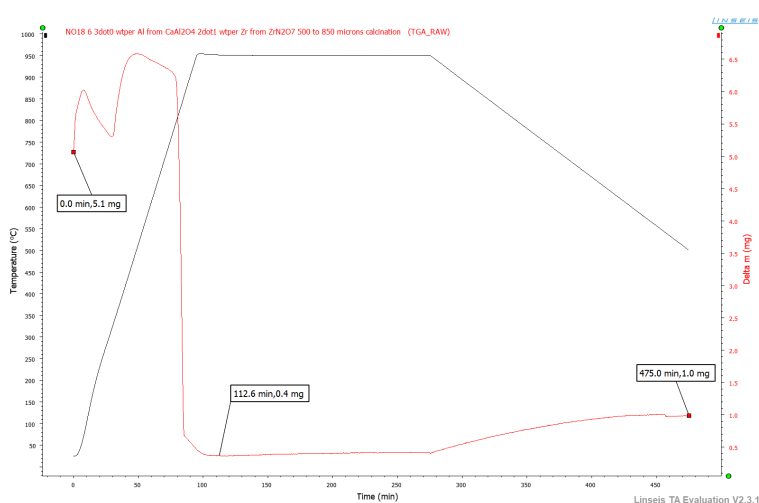


Figure B.21: Raw data, without correction, from calcination of the sorbent Al(insol)_AZr in Linseis TGA.

Cyclic CO₂ capture and regeneration

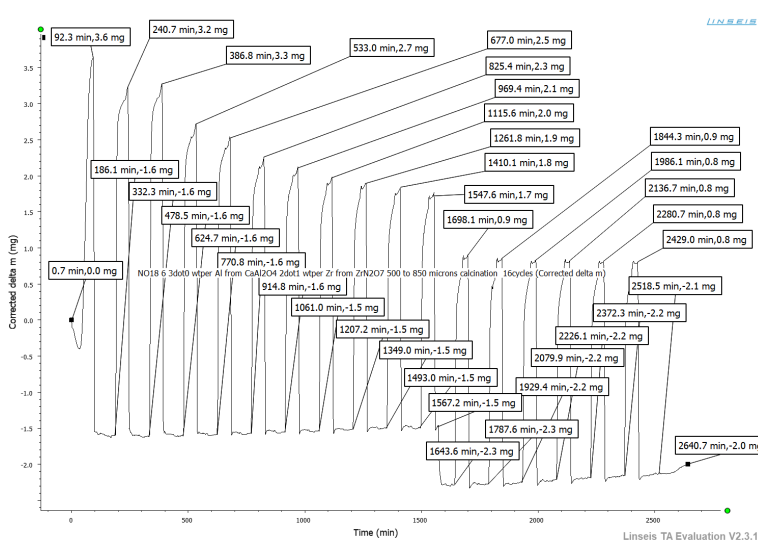


Figure B.22: Raw data from the CO₂ capturing experiment performed in Linseis TGA for the sorbent Al(insol)_AZr. The picture shows C₁ to C₁₇.

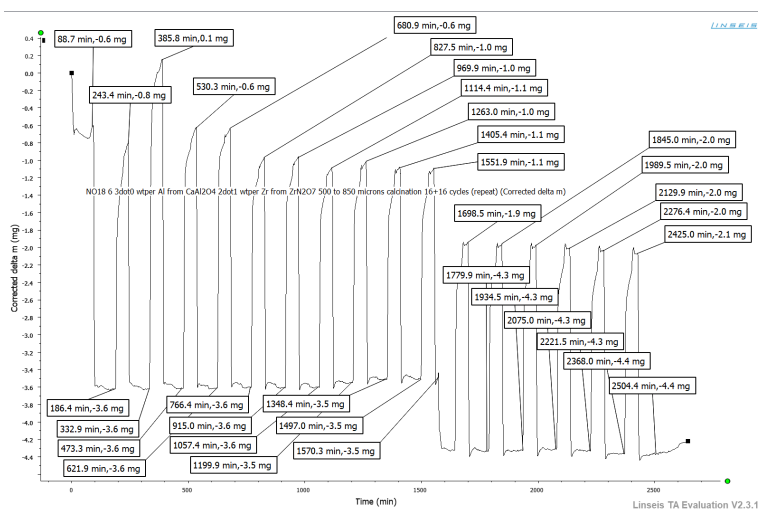


Figure B.23: Raw data from the CO₂ capturing experiment performed in Linseis TGA for the sorbent Al(insol)_AZr. The picture shows C₁₈ to C₃₄.

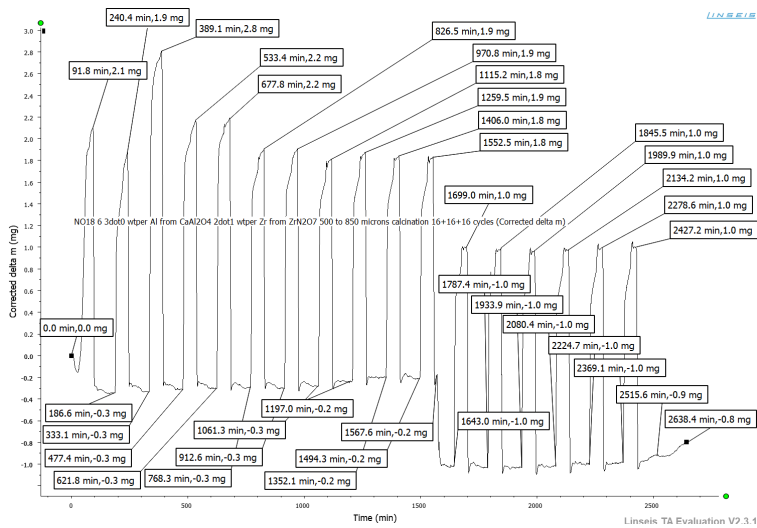


Figure B.24: Raw data from the CO₂ capturing experiment performed in Linseis TGA for the sorbent Al(insol)_AZr. The picture shows C₃₅ to C₅₁.

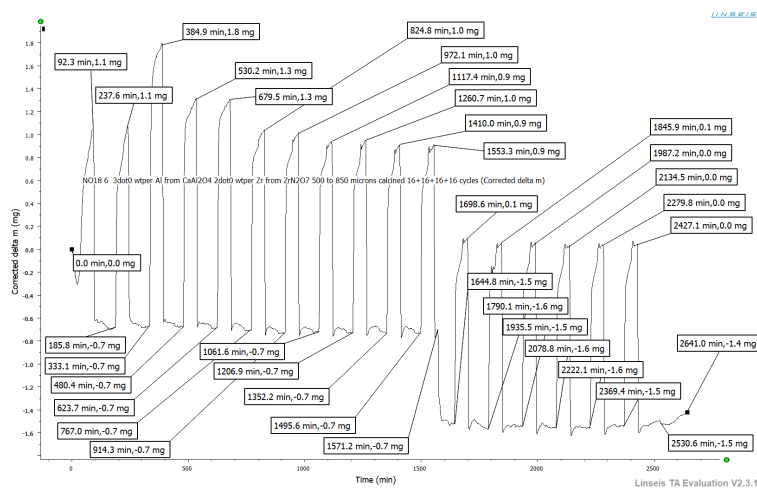


Figure B.25: Raw data from the CO₂ capturing experiment performed in Linseis TGA for the sorbent Al(insol)_AZr. The picture shows C₅₂ to C₆₈.

B.3.6 MgCe

Calcination

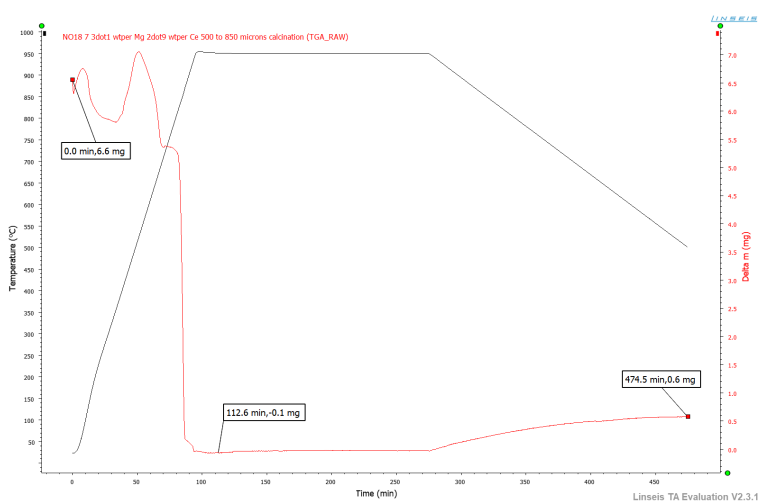


Figure B.26: Raw data, without correction, from calcination of the sorbent MgCe in Linseis TGA.

Cyclic CO₂ capture and regeneration

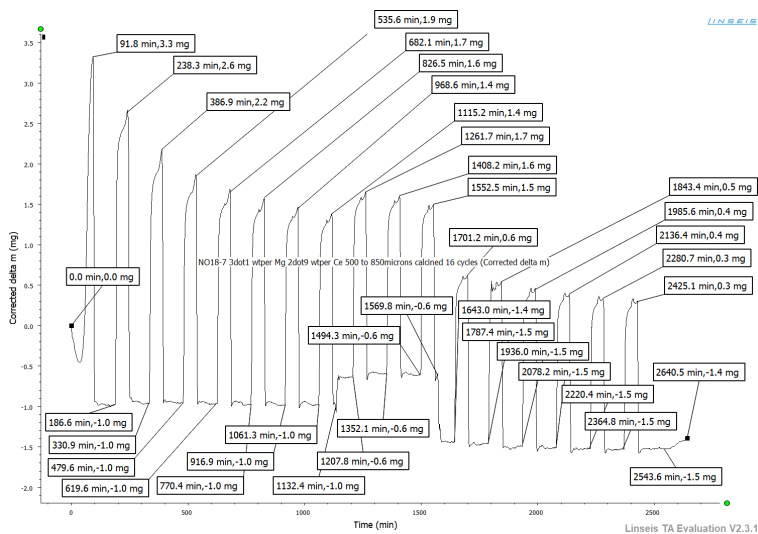


Figure B.27: Raw data from the CO₂ capturing experiment performed in Linseis TGA for the sorbent MgCe. The picture shows C₁ to C₁₇.

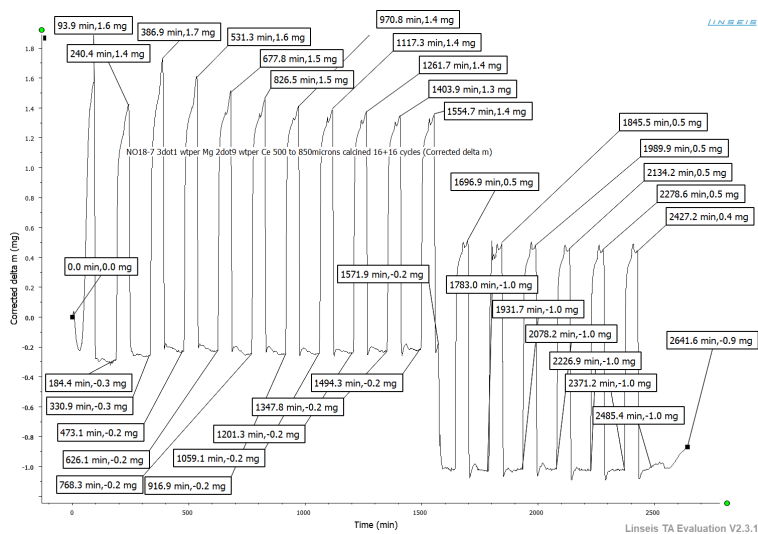


Figure B.28: Raw data from the CO₂ capturing experiment performed in Linseis TGA for the sorbent MgCe. The picture shows C₁₈ to C₃₄.

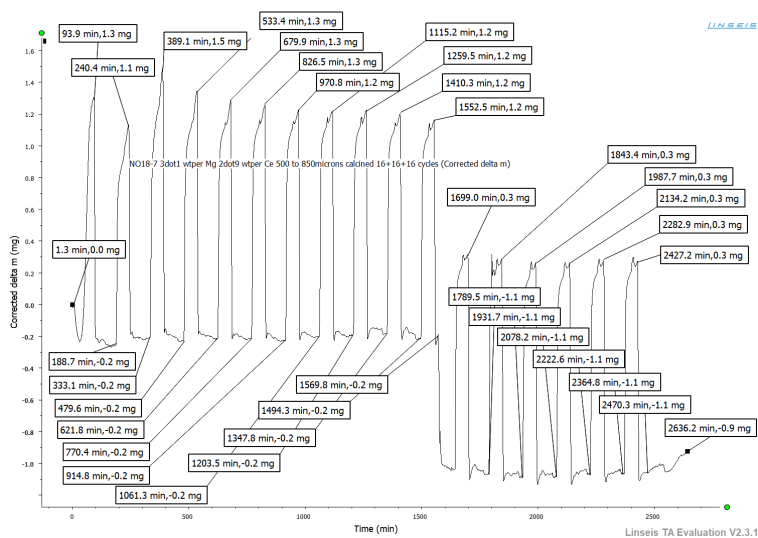


Figure B.29: Raw data from the CO₂ capturing experiment performed in Linseis TGA for the sorbent MgCe. The picture shows C₃₅ to C₅₁.

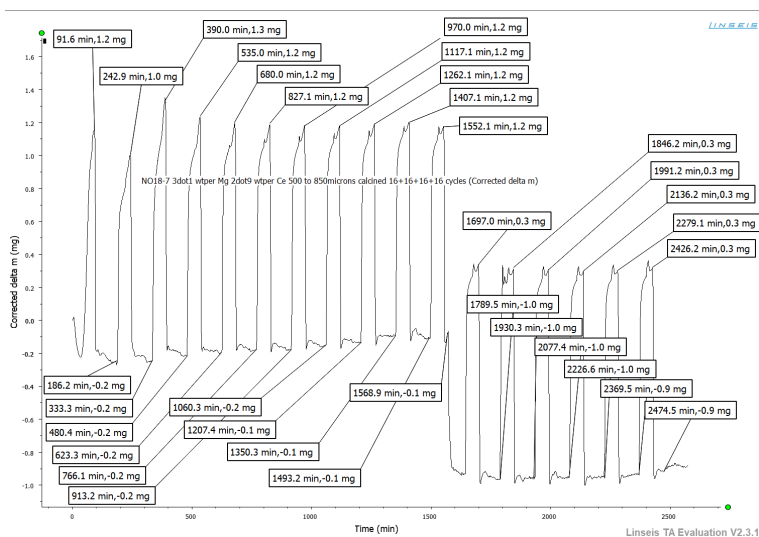


Figure B.30: Raw data from the CO₂ capturing experiment performed in Linseis TGA for the sorbent MgCe. The picture shows C₅₂ to C₆₈.

B.3.7 MgZr

Calcination

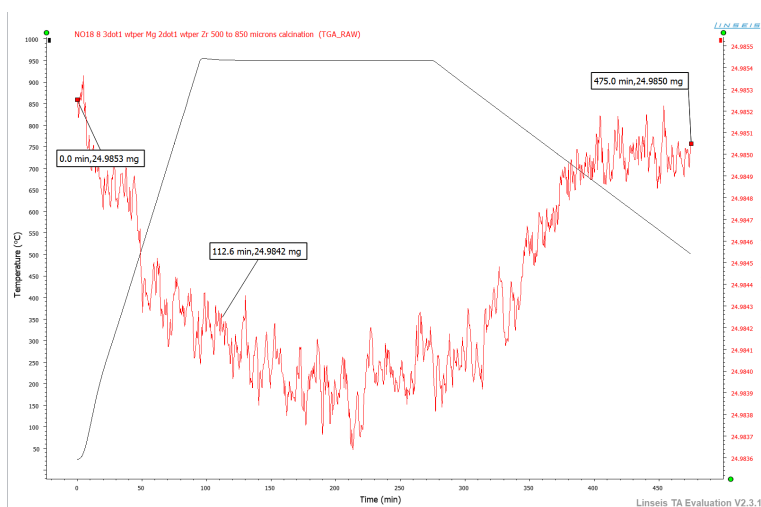


Figure B.31: Raw data, without correction, from calcination of the sorbent MgZr in Linseis TGA.

Cyclic CO₂ capture and regeneration

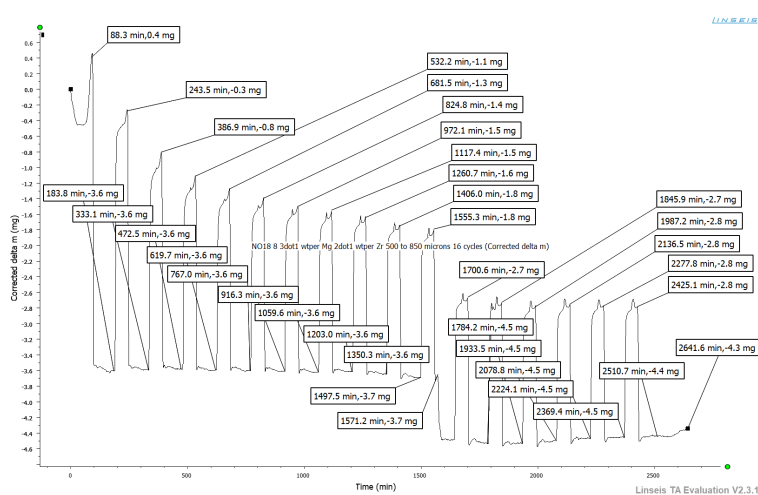


Figure B.32: Raw data from the CO₂ capturing experiment performed in Linseis TGA for the sorbent MgZr. The picture shows C₁ to C₁₇.

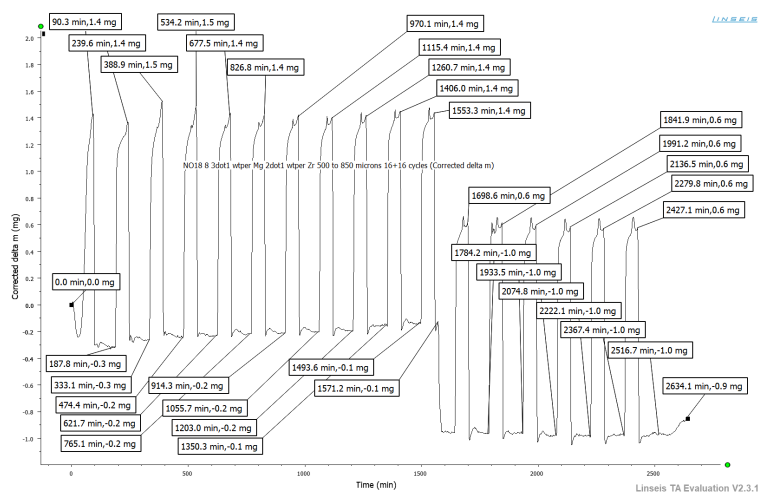


Figure B.33: Raw data from the CO₂ capturing experiment performed in Linseis TGA for the sorbent MgZr. The picture shows C₁₈ to C₃₄.

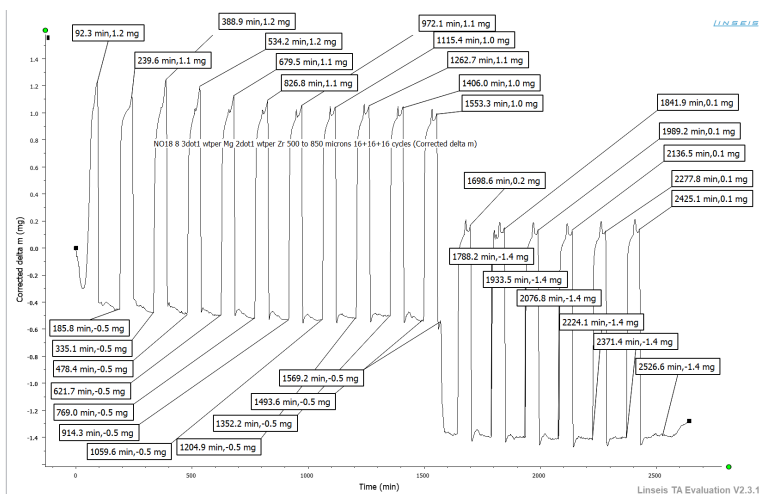


Figure B.34: Raw data from the CO₂ capturing experiment performed in Linseis TGA for the sorbent MgZr. The picture shows C₃₅ to C₅₁.

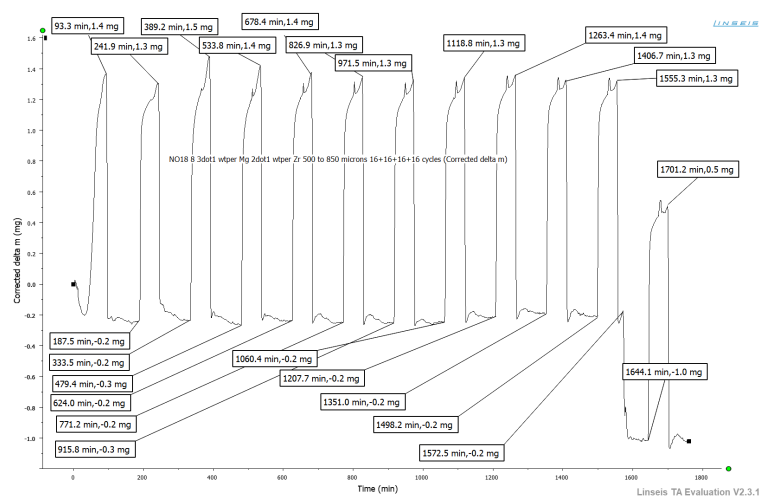


Figure B.35: Raw data from the CO₂ capturing experiment performed in Linseis TGA for the sorbent MgZr. The picture shows C₅₂ to C₆₃.

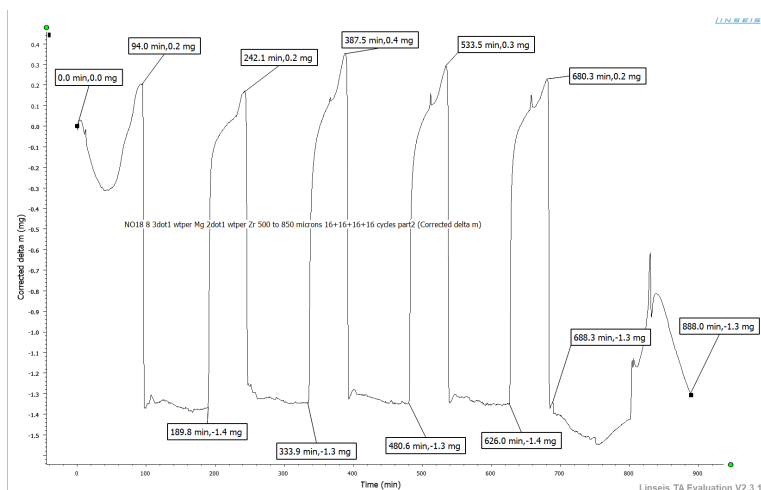


Figure B.36: Raw data from the CO₂ capturing experiment performed in Linseis TGA for the sorbent MgZr. The picture shows C₆₄ to C₆₈.

B.3.8 Ce

Calcination

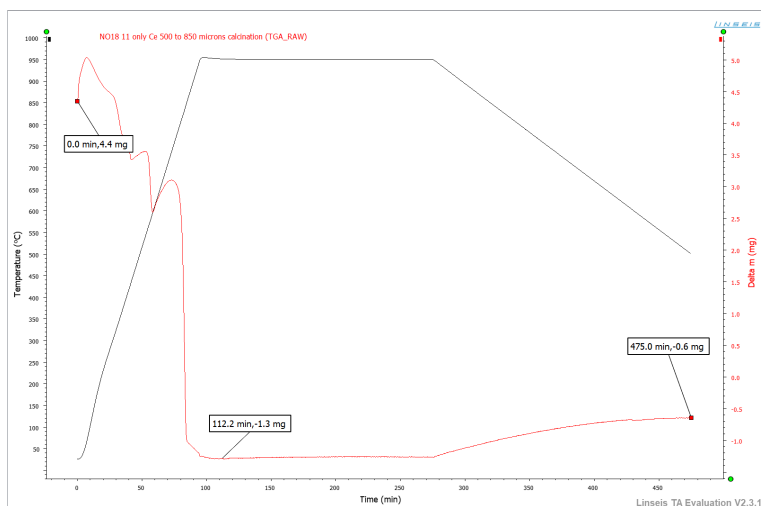


Figure B.37: Raw data, without correction, from calcination of the sorbent Ce in Linseis TGA.

Cyclic CO₂ capture and regeneration

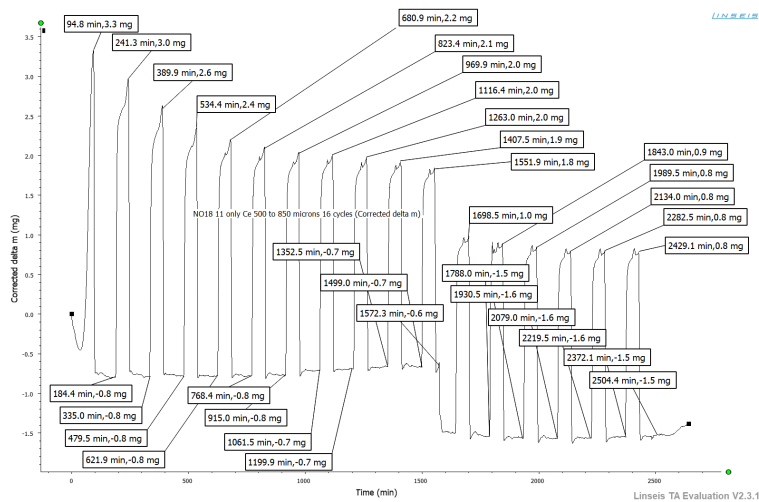


Figure B.38: Raw data from the CO₂ capturing experiment performed in Linseis TGA for the sorbent Ce. The picture shows C₁ to C₁₇.

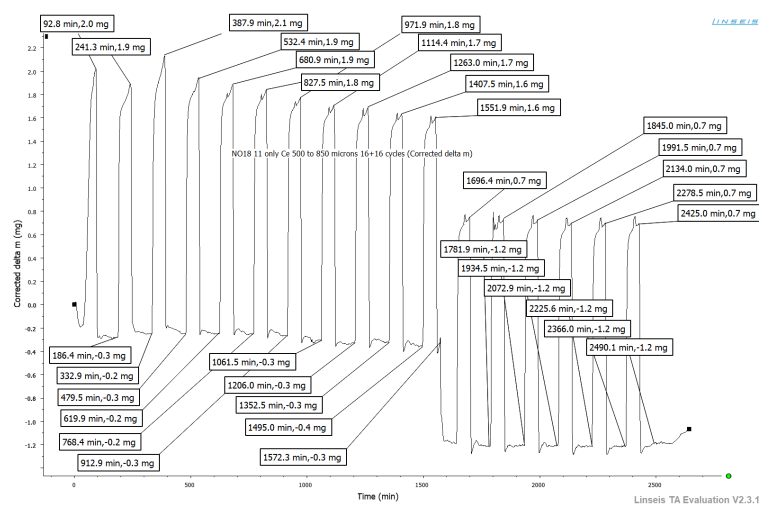


Figure B.39: Raw data from the CO₂ capturing experiment performed in Linseis TGA for the sorbent Ce. The picture shows C₁₈ to C₃₄.

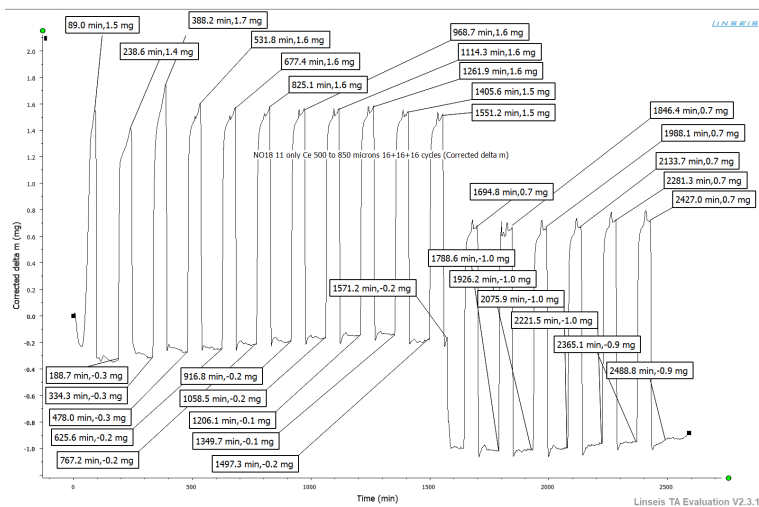


Figure B.40: Raw data from the CO₂ capturing experiment performed in Linseis TGA for the sorbent Ce. The picture shows C₃₅ to C₅₁.

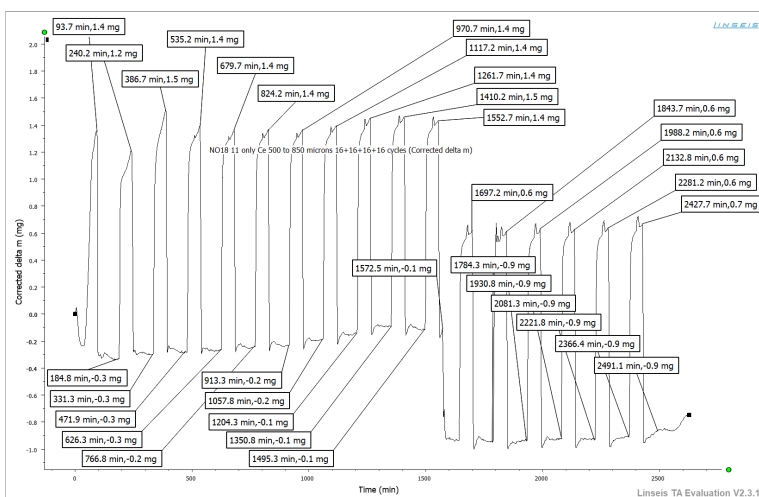


Figure B.41: Raw data from the CO₂ capturing experiment performed in Linseis TGA for the sorbent Ce. The picture shows C₅₂ to C₆₈.

B.3.9 Al(insol)_BZr

Calcination

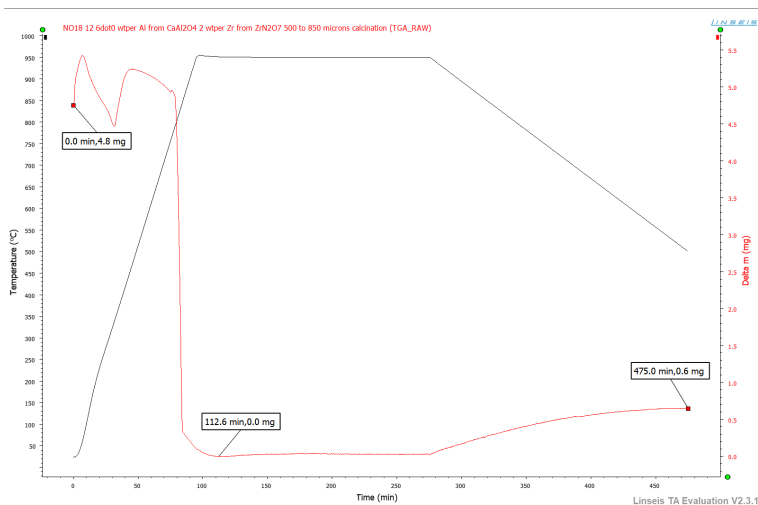


Figure B.42: Raw data, without correction, from calcination of the sorbent $\text{Al}(\text{insol})_B\text{Zr}$ in Linseis TGA.

Cyclic CO_2 capture and regeneration

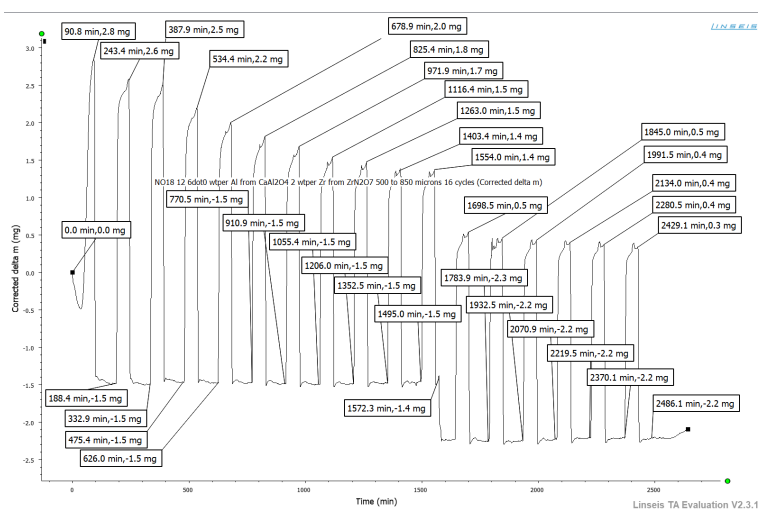


Figure B.43: Raw data from the CO_2 capturing experiment performed in Linseis TGA for the sorbent $\text{Al}(\text{insol})_B\text{Zr}$. The picture shows C_1 to C_{17} .

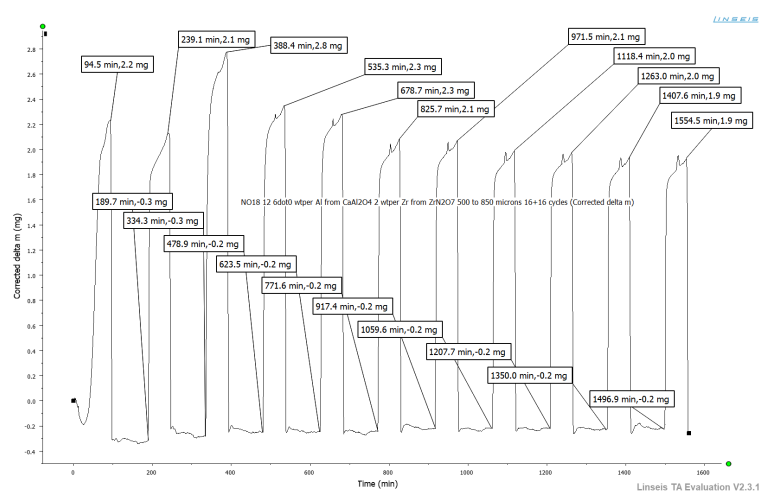


Figure B.44: Raw data from the CO₂ capturing experiment performed in Linseis TGA for the sorbent Al(insol)_BZr. The picture shows C₁₈ to C₂₈.

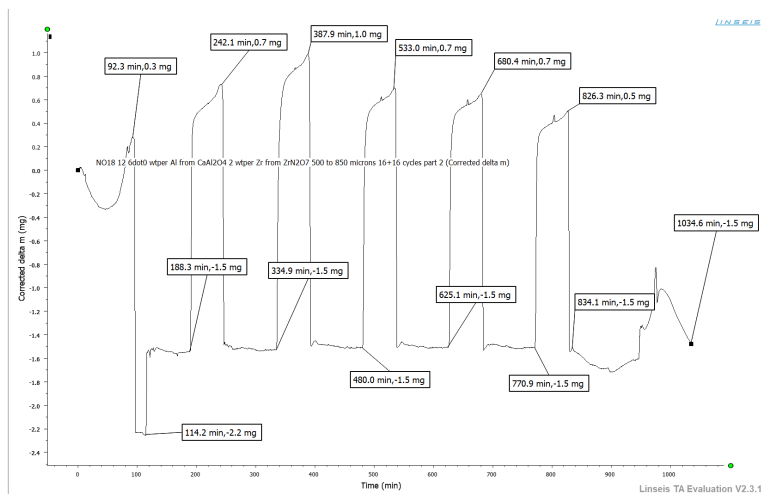


Figure B.45: Raw data from the CO₂ capturing experiment performed in Linseis TGA for the sorbent Al(insol)_BZr. The picture shows C₂₉ to C₃₄.

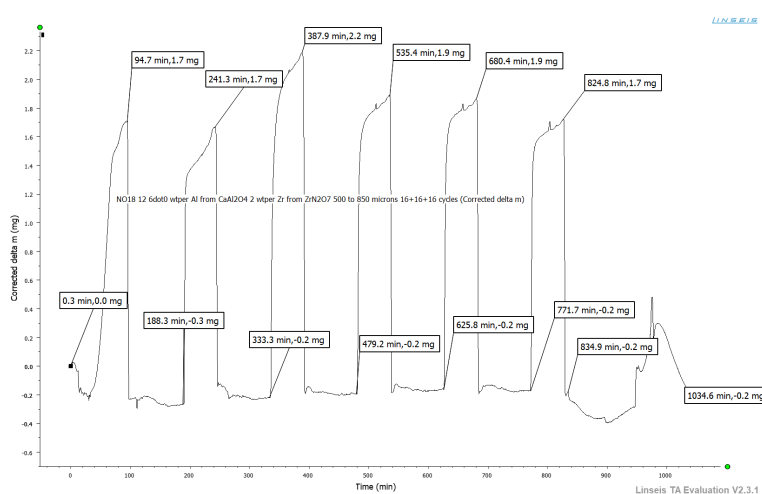


Figure B.46: Raw data from the CO₂ capturing experiment performed in Linseis TGA for the sorbent Al(insol)_BZr. The picture shows C₃₅ to C₄₀.

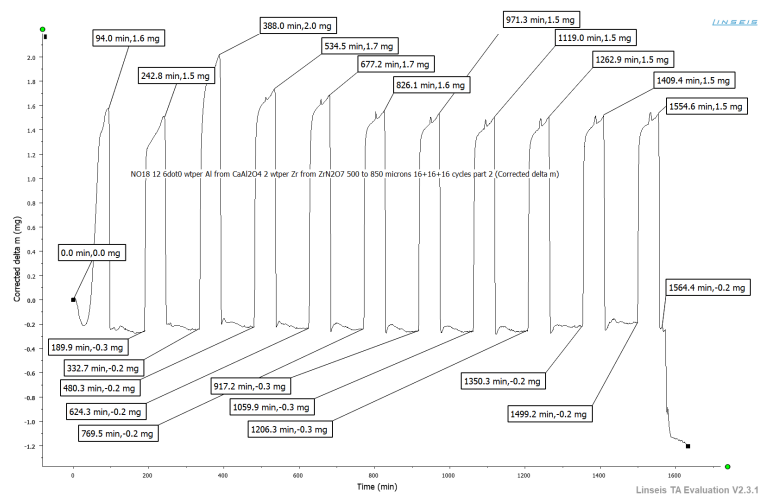


Figure B.47: Raw data from the CO₂ capturing experiment performed in Linseis TGA for the sorbent Al(insol)_BZr. The picture shows C₄₀ to C₅₁.

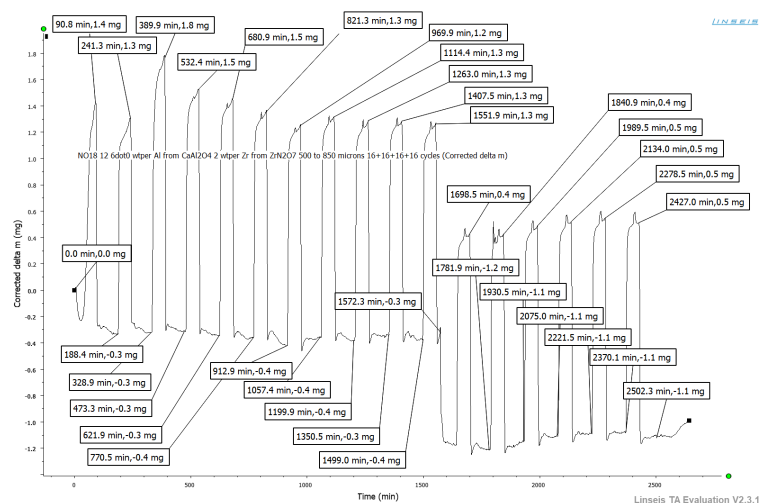


Figure B.48: Raw data from the CO₂ capturing experiment performed in Linseis TGA for the sorbent Al(insol)_BZr. The picture shows C₅₂ to C₆₈.

B.4 X-ray diffraction (XRD)

The analyzed diffraction diagrams of the sorbents are given in Figure B.49-B.58. The background noise and contamination caused by K α ₂ radiation were removed.

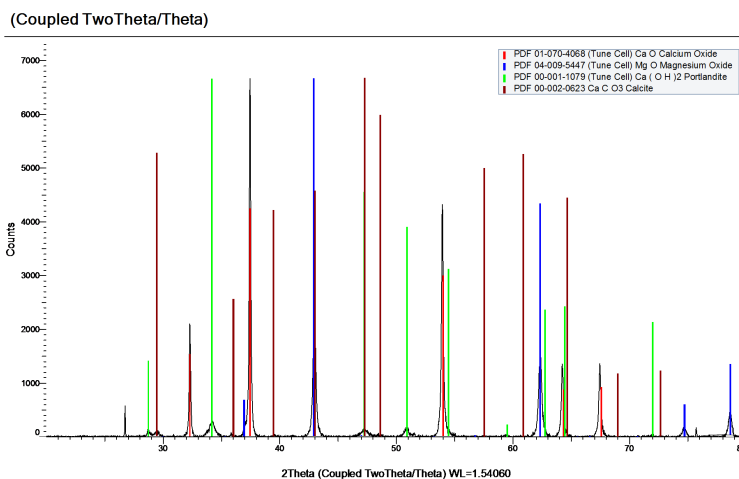


Figure B.49: Diffraction diagram of calcined dolomite.

(TwoTheta)

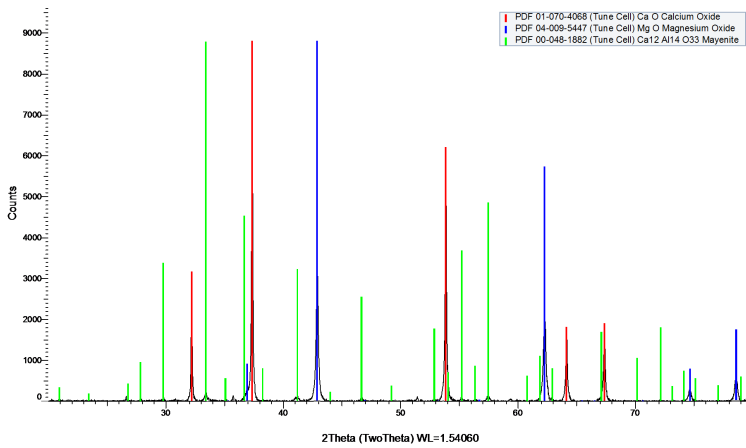


Figure B.50: Diffraction diagram of Al(sol)Mg.

(TwoTheta)

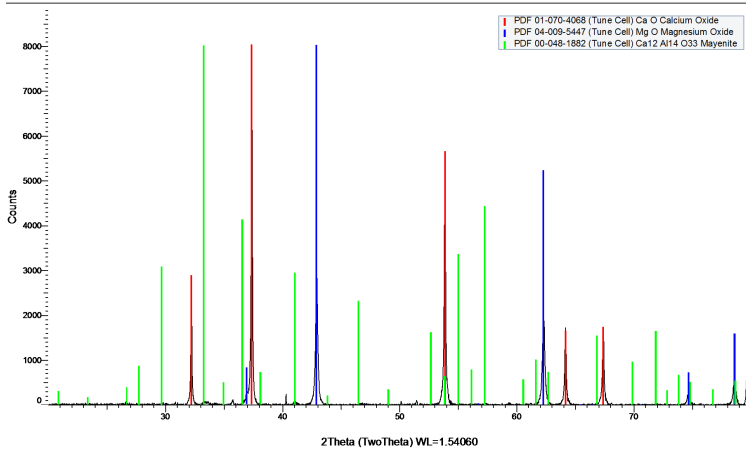


Figure B.51: Diffraction diagram of Al(insol)Mg.

(TwoTheta)

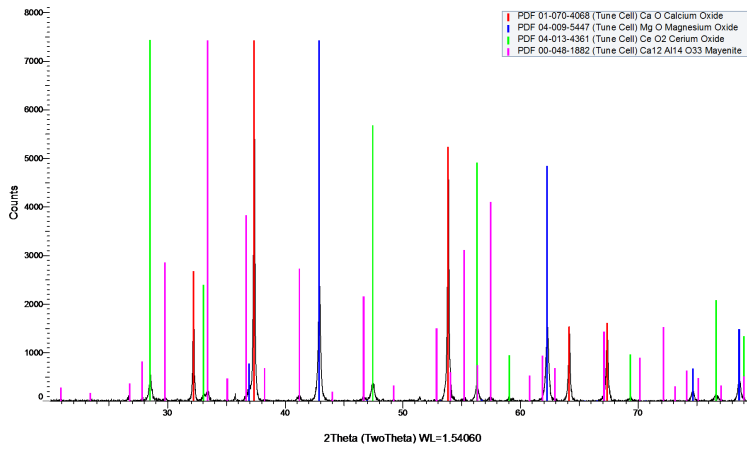


Figure B.52: Diffraction diagram of Al(sol)Ce.

(TwoTheta)

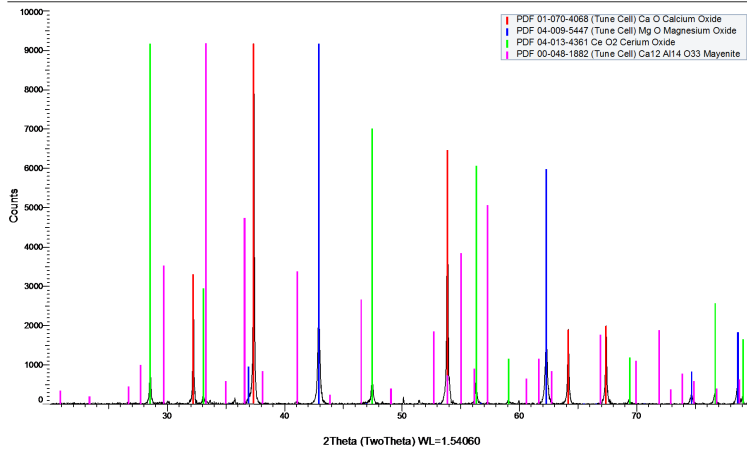


Figure B.53: Diffraction diagram of Al(insol)Ce.

(Coupled TwoTheta/Theta)

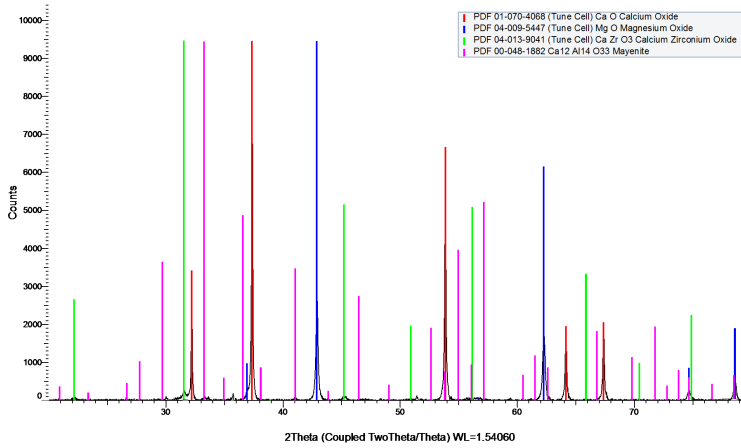


Figure B.54: Diffraction diagram of Al(insol)₄Zr.

(Coupled TwoTheta/Theta)

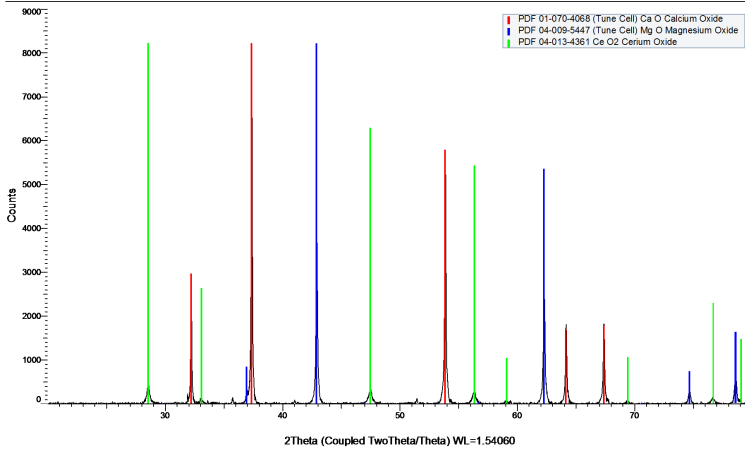


Figure B.55: Diffraction diagram of MgCe.

(Coupled TwoTheta/Theta)

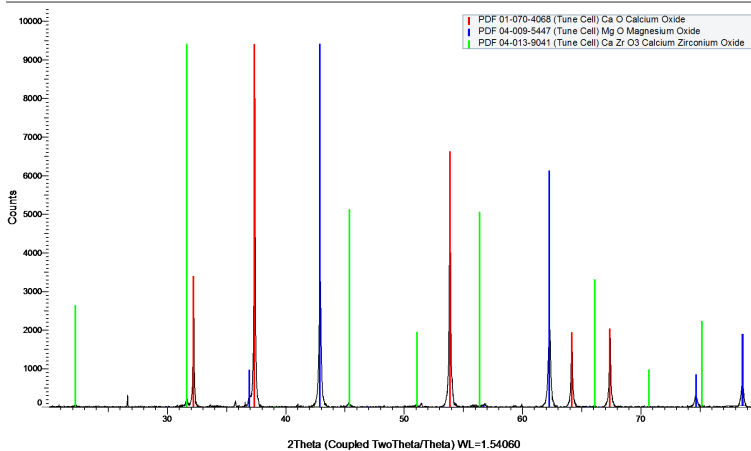


Figure B.56: Diffraction diagram of MgZr.

(Coupled TwoTheta/Theta)

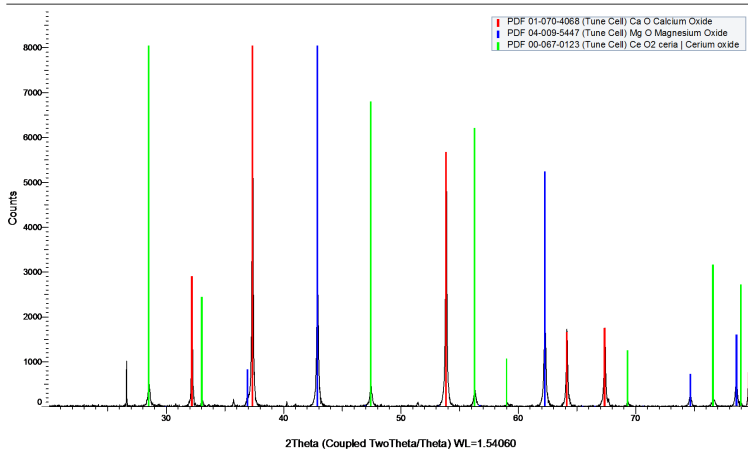


Figure B.57: Diffraction diagram of the sorbent Ce.

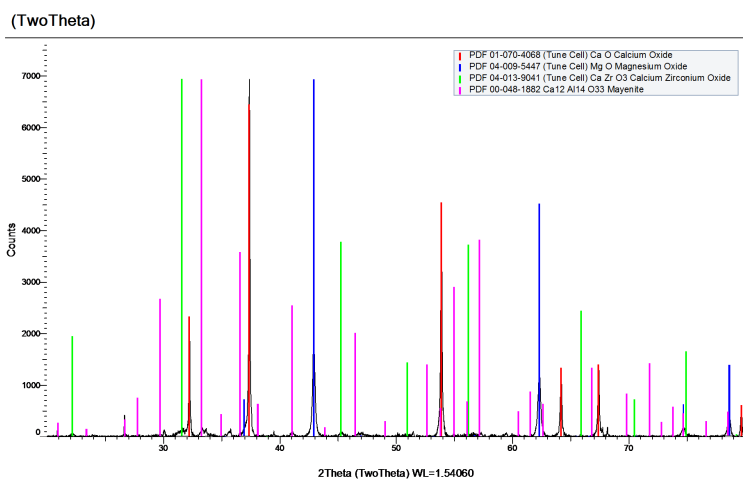


Figure B.58: Diffraction diagram of Al(insol)_BZr.

The raw data for crystallite size of CaO, MgO, CaZrO₃ and CeO₂ is given in Table B.3, B.4, B.5 and B.6. An average value was calculated based on these numbers.

Table B.3: The crystallite size, given as cs_j for peak j , of CaO calculated from six peaks in the diffraction diagram.

Sorbent	cs_1 [nm]	cs_2 [nm]	cs_3 [nm]	cs_4 [nm]	cs_5 [nm]	cs_6 [nm]
Calcined dolomite	67	65	57	53	52	62
Al(sol)Mg	87	88	76	70	67	72
Al(insol)Mg	86	82	75	72	73	78
Al(sol)Ce	85	80	70	64	64	64
Al(insol)Ce	104	98	88	80	84	91
Al(insol) _A Zr	95	88	79	76	77	75
MgCe	89	88	81	76	78	85
MgZr	92	87	82	71	76	87
Ce	89	85	76	76	73	75
Al(insol) _B Zr	96	92	77	71	72	78

Table B.4: The crystallite size, given as cs_j for peak j , of MgO calculated from four peaks in the diffraction diagram.

Sorbent	cs_1 [nm]	cs_2 [nm]	cs_3 [nm]	cs_4 [nm]
Calcined dolomite	36	33	39	35
Al(sol)Mg	47	46	50	48
Al(insol)Mg	45	47	48	50
Al(sol)Ce	44	41	51	41
Al(insol)Ce	44	45	47	55
Al(insol) _A Zr	47	44	47	44
MgCe	64	63	59	62
MgZr	48	47	47	45
Ce	53	53	56	56
Al(insol) _B Zr	41	41	37	46

Table B.5: The crystallite size, given as cs_j for peak j , of CaZrO₃ calculated from four peaks in the diffraction diagram.

Sorbent	cs_1 [nm]	cs_2 [nm]
Al(insol) _A Zr	36	36
MgZr	45	36
Al(insol) _B Zr	50	53

Table B.6: The crystallite size, given as cs_j for peak j , of CeO₂ calculated from four peaks in the diffraction diagram.

Sorbent	cs_1 [nm]	cs_2 [nm]	cs_3 [nm]	cs_4 [nm]
Al(sol)Ce	42	34	36	33
Al(insol)Ce	61	60	60	69
MgCe	36	35	35	39
Ce	42	45	49	33

B.5 Mechanical test

Table B.7: The mass of sorbent with size 250-500 μm used in each drop and the mass of residue with size < 250 μm .

Sorbent	Drop	$m_{\text{sample } 250-500\mu\text{m}}$ [g]	$m_{\text{residue } < 250\mu\text{m}}$ [g]
Al(sol)Mg	1	1.0031	0.0311
	2	0.9657	0.0113
	3	0.9494	0.0051
	4	0.9355	0.0032
	5	0.9332	0.0030

Al(insol)Mg	1	0.4794	0.0103
	2	0.4688	0.0031
	3	0.4649	0.0018
	4	0.4634	0.0010
	5	0.4615	0.0010
Al(sol)Ce	1	1.0009	0.0950
	2	0.8925	0.0246
	3	0.8648	0.0118
	4	0.8508	0.0080
	5	0.8417	0.0074
Al(insol)Ce	1	1.0042	0.0569
	2	0.9285	0.0193
	3	0.9097	0.0118
	4	0.8907	0.0074
	5	0.8841	0.0069
Al(insol) _A Zr	1	1.0012	0.1812
	2	0.8040	0.0608
	3	0.7389	0.0328
	4	0.6947	0.0190
	5	0.6722	0.0166
MgCe	1	1.0004	0.0128
	2	0.9871	0.0052
	3	0.9814	0.0023
	4	0.9796	0.0021
	5	0.9770	0.0015
MgZr	1	0.9987	0.0054
	2	0.9928	0.0021
	3	0.9897	0.0010
	4	0.9886	0.0012
	5	0.9871	0.0013
Ce	1	1.0034	0.0898
	2	0.9124	0.0207
	3	0.8895	0.0111
	4	0.8780	0.0071
	5	0.8698	0.0068
Al(insol) _B Zr	1	1.0086	0.0783
	2	0.9205	0.0349
	3	0.8815	0.0187
	4	0.8598	0.0113
	5	0.8456	0.0096

Table B.8: The mass of sorbent with size 500-850 μm used in each drop, the mass of residue with size $< 500 \mu\text{m}$.

Sorbent	Drop	$m_{\text{sample } 500-850\mu\text{m}}$ [g]	$m_{\text{residue } < 500\mu\text{m}}$ [g]
Al(sol)Mg	1	0.9986	0.0420
	2	0.9468	0.0213
	3	0.9242	0.0120
	4	0.9129	0.0115
	5	0.8997	0.0048
Al(insol)Mg	1	1.0014	0.0252
	2	0.9723	0.0124
	3	0.9564	0.0048
	4	0.9486	0.0045
	5	0.9395	0.0038
Al(sol)Ce	1	1.0014	0.2644
	2	0.7331	0.0565
	3	0.6733	0.0202
	4	0.6521	0.0114
	5	0.6399	0.0058
Al(insol)Ce	1	1.0040	0.0504
	2	0.9513	0.0134
	3	0.9385	0.0096
	4	0.9273	0.0054
	5	0.9224	0.0062
Al(insol) _A Zr	1	0.9966	0.1824
	2	0.8083	0.0579
	3	0.7487	0.0269
	4	0.7223	0.0122
	5	0.7087	0.0145
MgCe	1	1.0009	0.0106
	2	0.9905	0.0052
	3	0.9831	0.0029
	4	0.9791	0.0027
	5	0.9759	0.0036
MgZr	1	0.9966	0.0060
	2	0.9907	0.0042
	3	0.9855	0.0042
	4	0.9804	0.0029
	5	0.9783	0.0026
Ce	1	1.0018	0.1803
	2	0.8178	0.0422
	3	0.7738	0.0168
	4	0.7566	0.0091
	5	0.7473	0.0064
Al(insol) _B Zr	1	1.0050	0.0925

	2	0.8696	0.0329
	3	0.8391	0.0255
	4	0.8153	0.0207
	5	0.7394	0.0160

B.6 N₂ adsorption-desorption analysis

B.6.1 Specific surface area, pore volume, pore diameter and porosity

Table B.9: The result from two N₂ adsorption-desorption measurements. Single point surface area calculated when $p/p_0 = 0.20$, BJH desorption cumulative pore volume, BJH desorption average pore diameter and the porosity.

Sorbent	SA [m ² /g]		V _p [cm ³ /g]		d _p [nm]		θ [%]	
Calcined dolomite	17.6		0.08		18.7		21.9	
Al(sol)Mg	7.4	6.4	0.05	0.04	23.5	29.6	14.2	11.7
Al(insol)Mg	7.3	6.7	0.05	0.04	25.1	28.1	14.5	12.8
Al(sol)Ce	7.2	5.5	0.04	0.03	23.6	27.3	11.2	8.6
Al(insol)Ce	8.2	7.1	0.03	0.02	17.8	16.2	8.6	6.3
Al(insol) _A Zr	7.7	6.6	0.02	0.03	14.5	20.9	7.5	8.8
MgCe	4.6	3.9	0.03	0.02	28.6	25.1	8.0	6.0
MgZr	6.2	5.0	0.02	0.02	18.7	20.0	7.2	6.7
Ce	5.8	5.9	0.02	0.02	14.1	15.7	6.1	5.9
Al(insol) _B Zr	8.5	9.0	0.03	0.03	16.2	17.4	8.7	8.6

B.6.2 Pore size distribution plots

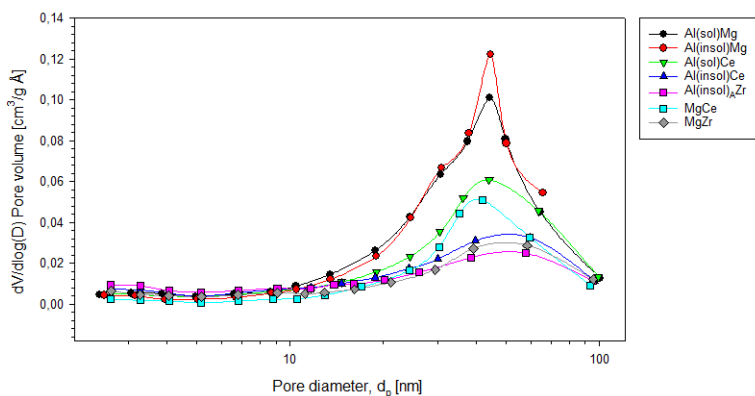


Figure B.59: Pore size distribution of Al(sol)Mg, Al(insol)Mg, Al(sol)Ce, Al(insol)Ce, Al(insol)_AZr, MgCe and MgZr generated using the desorption branch.

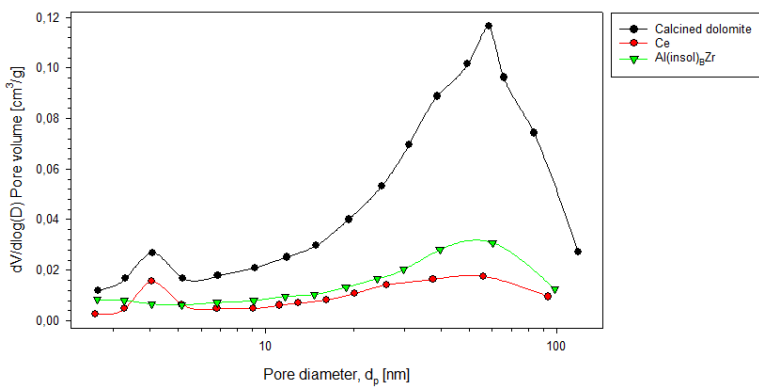


Figure B.60: Pore size distribution of calcined dolomite, Ce and Al(insol)_BZr generated using the desorption branch.

B.6.3 Adsorption isotherm

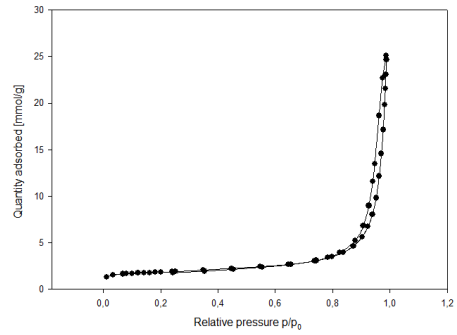
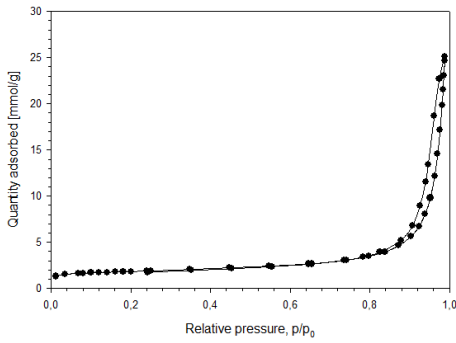


Figure B.61: The adsorption isotherms for Al(sol)Mg from two N₂ adsorption-desorption measurements.

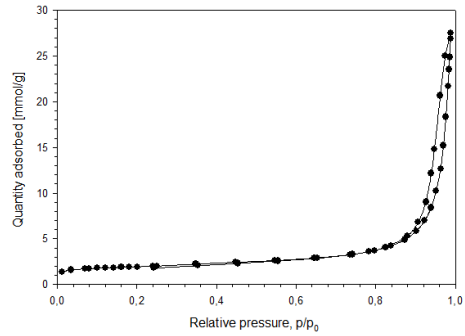
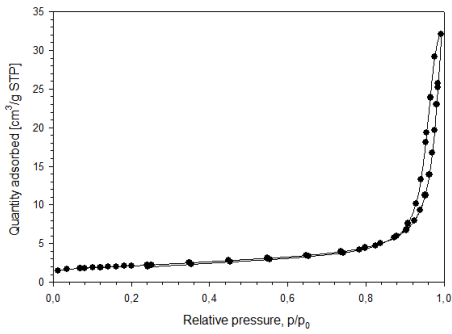


Figure B.62: The adsorption isotherms for Al(insol)Mg from two N₂ adsorption-desorption measurements.

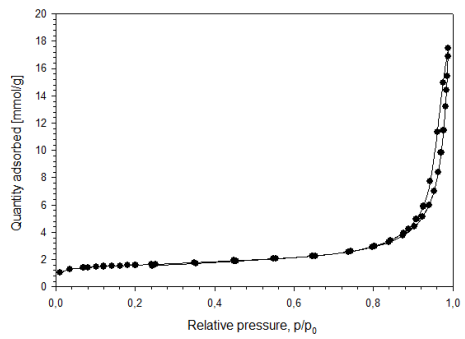
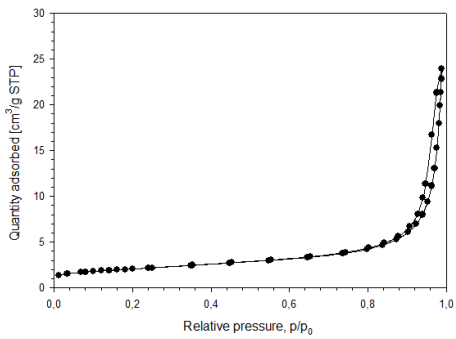


Figure B.63: The adsorption isotherms for Al(sol)Ce from two N₂ adsorption-desorption measurements.

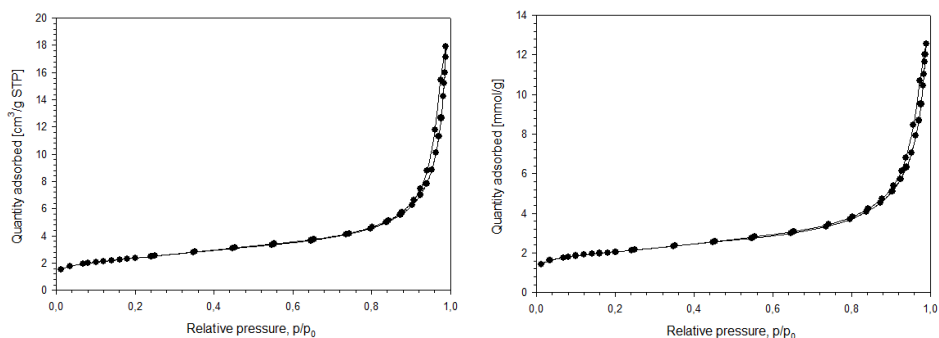


Figure B.64: The adsorption isotherms for Al(insol)Ce from two N₂ adsorption-desorption measurements.

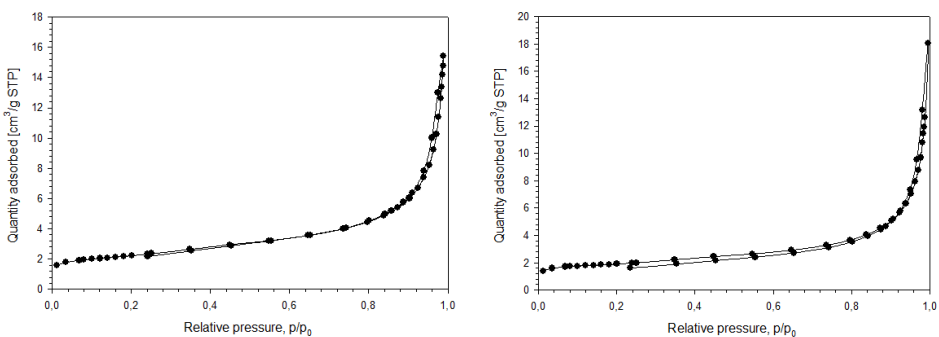


Figure B.65: The adsorption isotherms for Al(insol)_AZr from two N₂ adsorption-desorption measurements.

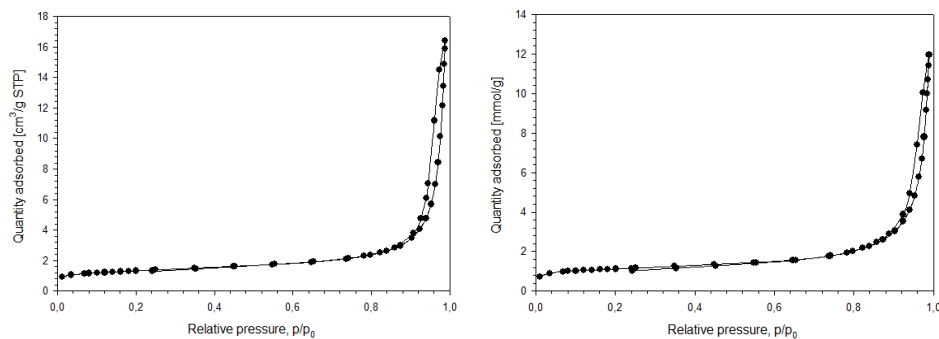


Figure B.66: The adsorption isotherms for MgCe from two N₂ adsorption-desorption measurements.

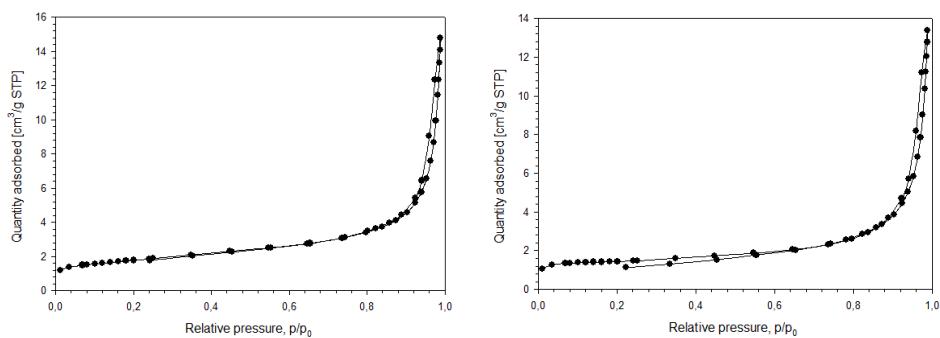


Figure B.67: The adsorption isotherms for MgZr from two N₂ adsorption-desorption measurements.

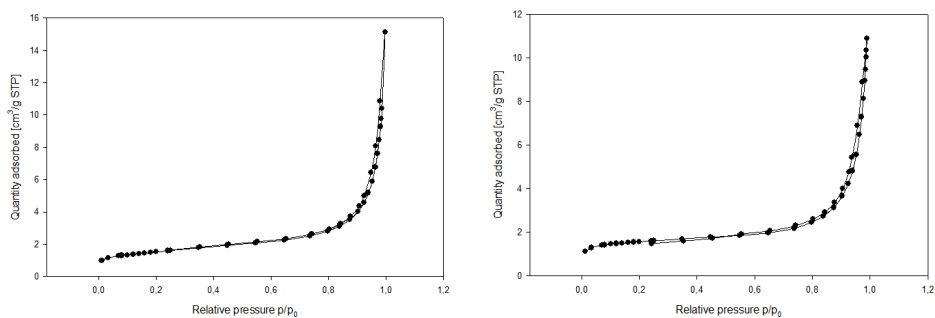


Figure B.68: The adsorption isotherms for the sorbent Ce from two N₂ adsorption-desorption measurements.

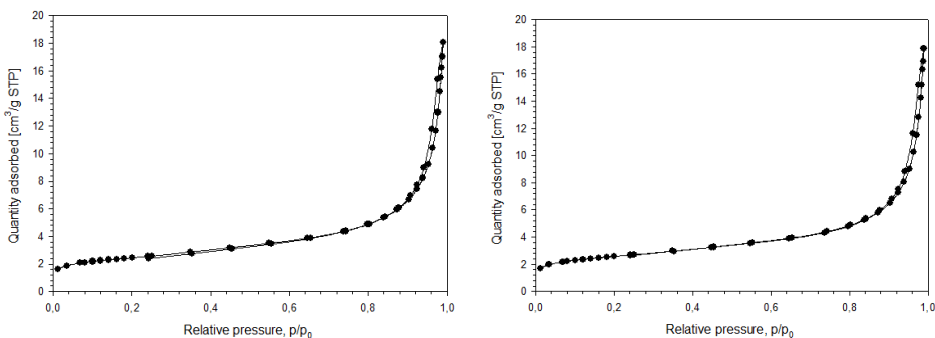


Figure B.69: The adsorption isotherms for Al(insol)_BZr from two N₂ adsorption-desorption measurements.

B.7 Energy-dispersive x-ray spectrometry

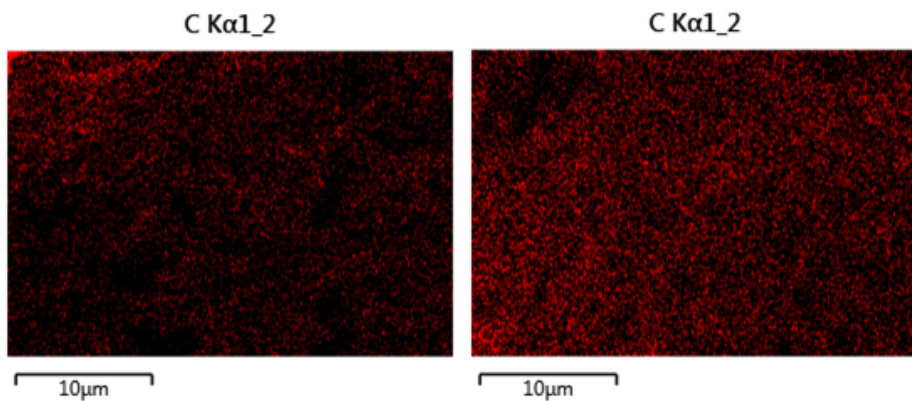


Figure B.70: EDS pictures of the Fondu cement and calcined dolomite.

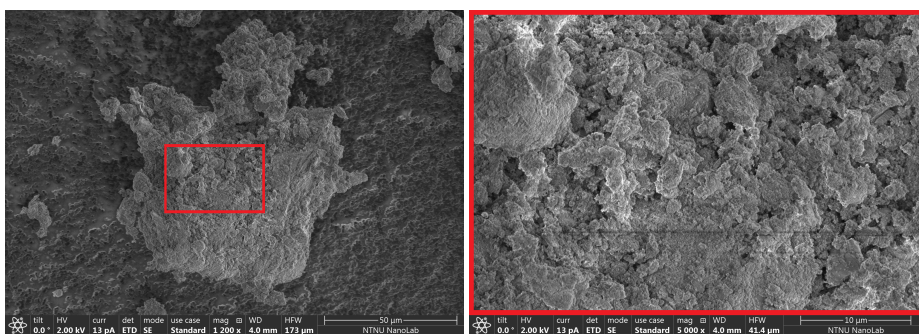


Figure B.71: SEM pictures giving an overview of the area analyzed by EDS for Al(sol)Mg.

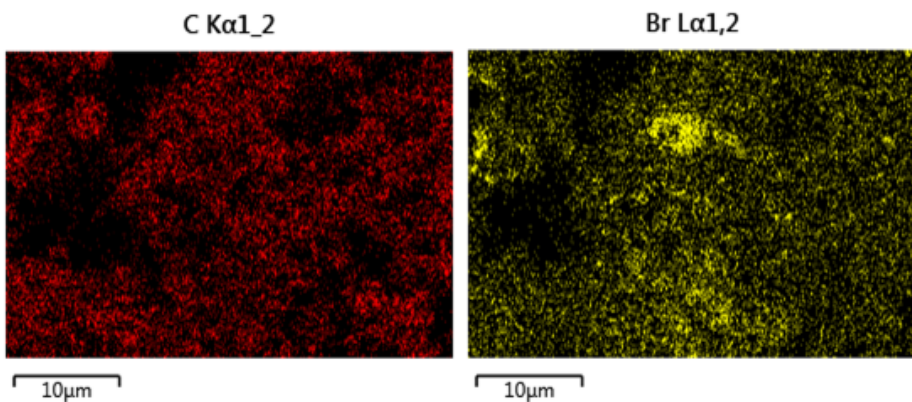


Figure B.72: EDS pictures of Al(sol)Mg.

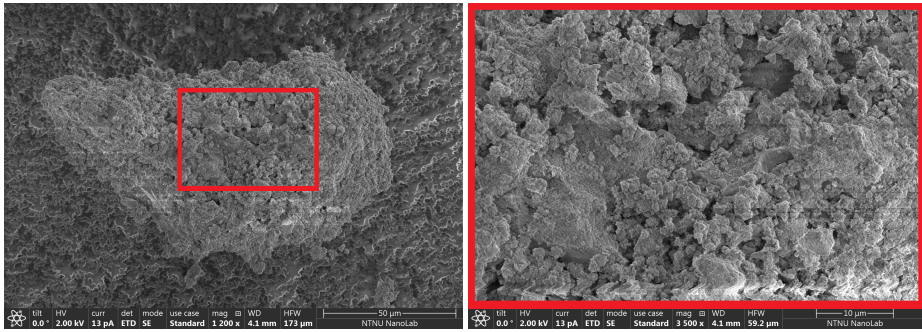


Figure B.73: SEM pictures giving an overview of the area analyzed by EDS for Al(insol)Mg.

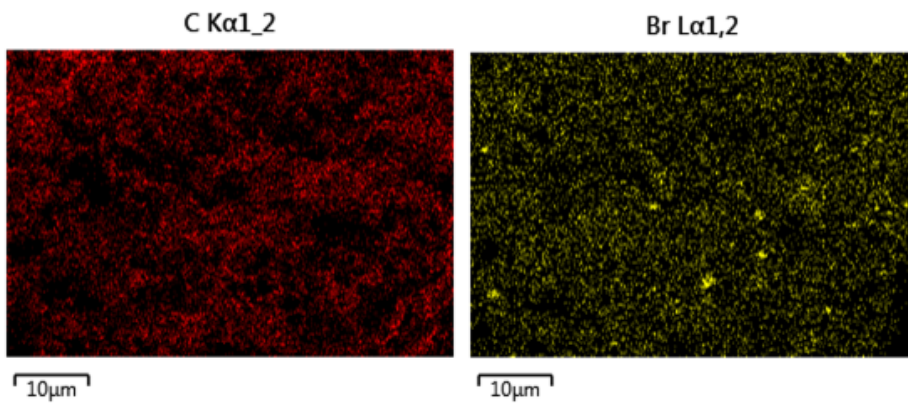


Figure B.74: EDS pictures of Al(insol)Zr.

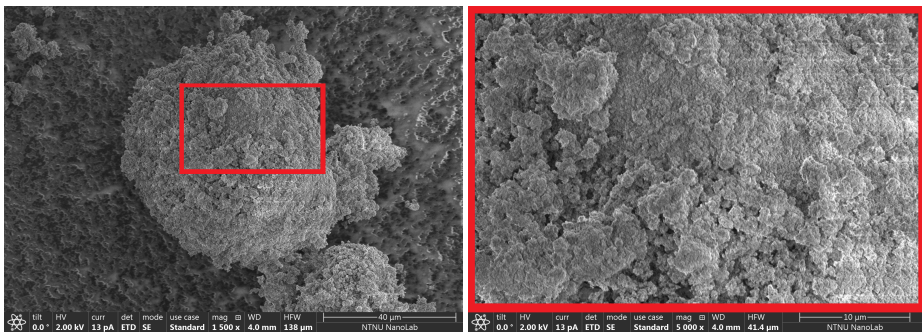


Figure B.75: SEM pictures giving an overview of the area analyzed by EDS for Al(insol)_AZr.

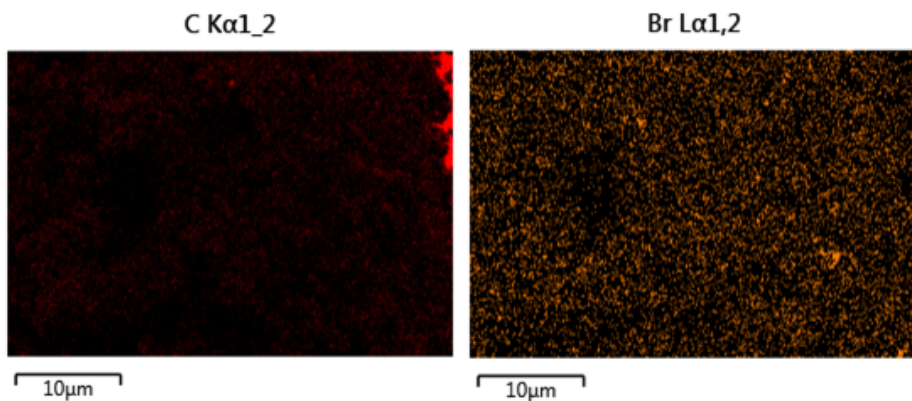


Figure B.76: EDS pictures of $\text{Al}(\text{insol})_{\text{AZr}}$.

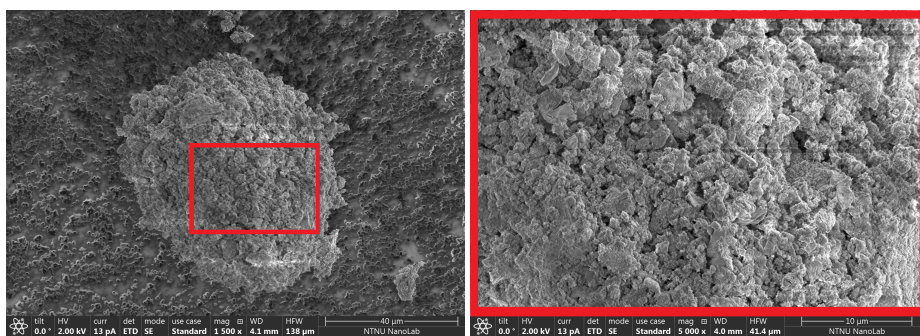


Figure B.77: SEM pictures giving an overview of the area analyzed by EDS for MgZr.

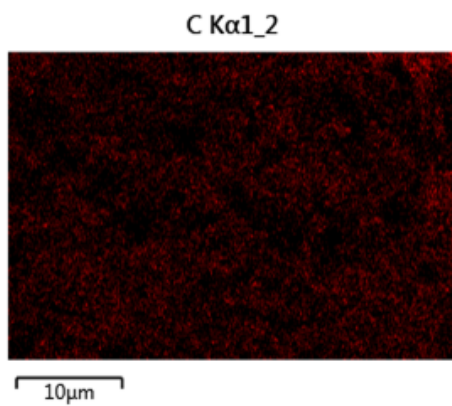


Figure B.78: EDS pictures of MgZr.

Appendix C

Other

Section C.1.1 and C.1.2 contain the relevant results from the specialisation project. The product data sheet for Fondu cement and the risk assessment are also given.

C.1 Specialisation project

C.1.1 Synthesis of sorbents

Dolomite calcined at 800 °C for 6 hours was doped with the elements Zr, Al and Mg using the method of incipient wetness impregnation. The precursors, desired weight percent dopant and nominal weight percent dopant are given in Table C.1, followed by a defined sample name. The desired weight is denoted by D wt % i, whilst the nominal weight is denoted by N wt% i.

Table C.1: The precursors used, the desired weight percent dopant in the sorbent and the actual weight percent dopant in the sorbent, denoted by *D wt% i* and *N wt% i*, respectively, and the defined sample name that is used as identification.

Precursor		D wt% Mg + Zr	N wt% Mg + Zr	Sample name
Mg(NO ₃) ₂ 6H ₂ O	ZrN ₂ O ₇	2 + 1	1.9 + 0.9	Mg _{1.9} Zr _{0.9}
Mg(NO ₃) ₂ 6H ₂ O	ZrN ₂ O ₇	2 + 2	1.9 + 1.9	Mg _{1.9} Zr _{1.9}
Mg(NO ₃) ₂ 6H ₂ O	ZrN ₂ O ₇	3 + 1	2.9 + 1.0	Mg _{2.9} Zr _{1.0}
Precursor		D wt% Al + Zr	N wt% Al + Zr	Sample name
Al(NO ₃) ₃ 9H ₂ O	ZrN ₂ O ₇	3 + 1.5	2.9 + 1.5	Al _{2.9} Zr _{1.5}
Al(NO ₃) ₃ 9H ₂ O	ZrN ₂ O ₇	3 + 2	2.9 + 1.9	Al _{2.9} Zr _{1.9}
Precursor		D wt% Al + Zr	N wt% Al + Zr	Sample name
Al(NO ₃) ₃ 9H ₂ O	ZrCl ₄	3 + 2	2.3 + 1.5	Al _{2.3} Zr _{1.5}
Precursor		D wt% Mg	N wt% Mg	Sample name
Mg(NO ₃) ₂ 6H ₂ O		5	3.3	Mg _{3.3}

C.1.2 Thermogravimetric analysis (TGA)

The CO₂ capacity and cyclic stability of all sorbents were tested in dry TGA. The CO₂ capacity for C₁, C₃₈, C₆₀ and C₁₂₂ (C₁₂₀) is presented in Table 6.2. The relative loss in C₆₀ and C₁₂₂ (C₁₂₀) is also given in Table 6.2.

Table C.2: An overview of the CO₂ capacity of all the sorbents in C₁, C₃₈, C₆₀ and C₁₂₂. The loss in CO₂ capacity for cycle *j* relative to cycle *i*, *L_{i,j}*, is also presented.

Sorbent	C ₁ [%]	C ₃₈ [%]	C ₆₀ [%]	C ₁₂₂ [%]	L _{1,38} [%]	L _{1,122} [%]
Mg _{1.9} Zr _{0.9}	37.6	22.3	19.3	14.4	49	62
Mg _{1.9} Zr _{1.9}	35.1	22.6	19.7	15.6	44	56
Mg _{2.9} Zr _{1.0}	35.8	18.9	18.2	14.7	49	59
Al _{2.9} Zr _{1.5}	34.1	21.8	20.0	16.1	41	53
Al _{2.9} Zr _{1.9}	37.9	24.6	22.2	18.0	41	52
Al _{2.3} Zr _{1.5}	31.6	23.0	21.3	17.2*	33	46**
Mg _{3.3}	41.2	23.6	19.5		53	

* indicates the CO₂ capacity in C₁₂₀.

** indicates the loss in CO₂ capacity for C₁₂₀ relative to C₁.

CIMENT FONDU®

Refractory applications

Reference FC-CF-RE-GB-KFR-032007

Updated 31/03/2008

1 General characteristics

Ciment Fondu® is a hydraulic binder, with an alumina content of approximately 40%.

The principal components of Ciment Fondu® are calcium aluminates which make it an ideal binder for refractory applications. Its high monocalcium aluminate content yields refractory concrete with excellent mechanical properties. Due to the iron oxide content of Ciment Fondu®, it is unsuitable for refractory concretes where iron oxide may not be tolerated, for example in reducing atmospheres.

The rheological properties of Ciment Fondu® are well adapted for all types of placing methods, particularly for casting and gunning. It is recommended for applications where rapid hardening and excellent performance are required.

Ciment Fondu® does not contain any additives, and is suited to the manufacture of refractory premixes.

Ciment Fondu® is produced and controlled within a quality management system that is certified according to ISO 9001.

2 Specification

The properties of Ciment Fondu® produced in Europe conform to the requirements defined in the norm: EN 14647 : "Calcium Aluminate Cement"

The *specification limits* indicated are determined with an acceptable quality level (AQL) of 2.5% defined in the standard ISO 3951.

The *strict specification limits* define the absolute limits of product conformity applicable for individual values.

The EN specification limits are conformed with the requirement defined in the norm EN 14647.

The *usual range* represents typical values of production.

Chemical composition

Main constituents (%)

	Usual range	Specification limit
Al ₂ O ₃	37.5 - 41.0	> 37.0
CaO	35.5 - 39.0	< 41.0
SiO ₂	3.5 - 5.5	< 6.0
Fe ₂ O ₃	13.0 - 17.5	< 18.5
MgO	-	< 1.5
TiO ₂	-	< 4.0

Other constituents (%)

	Strict specification limit
S (as sulphide ions)	≤ 0.1
Cl (as chloride ions)	≤ 0.1
Na ₂ O + 0,659 K ₂ O	≤ 0.4
SO ₃	≤ 0.5

The chemical characteristics of Ciment Fondu® have been determined according to the following:

- EN 196-2: Methods of testing cement - Chemical analysis of cement.

Fineness

	Usual range	Specification limit
Blaine Specific surface (cm ² /g)	2850 - 3450	> 2700

- Determined in accordance with EN 196-6: Methods of testing cements - Measurement of fineness.

Neat paste setting time

	Usual range	Specification limit
Initial set (min)	180 - 300	> 120
Final set (min)	210 - 330	< 480

- Determined in accordance with EN 196-3: neat cement paste at standard consistency; mechanical mixing ; Vicat test equipment using 300g weight ; temperature 20°C ; relative humidity >90%.

Mechanical strength

Compressive strength, MPa		
Age	Usual range	Strict specification limit
6 h	35 - 50	> 30
24 h	60 - 80	> 50

- Composition of mortar according to EN 14647: 1350g of sand, 500g of calcium aluminate cement, 200g of water
- Test conditions according to EN 196-1: test prisms 40x40x160mm; temperature 20°C ; prisms cured at >90% relative humidity for 24 hours (NF standard) or 6h (BS standard), followed by immersion in water.

3 Additional data

This information is given for guidance only.

- Principal mineralogical phase*: CA
- Secondary phases*: C₁₂A₇, C₂S, C₂AS, C₄AF

* C=CaO, A=Al₂O₃, S= SiO₂, F=Fe₂O₃

- Bulk density: 1100 kg/m³
- Specific gravity: 3.2 - 3.3 g/cm³
- Pyrometric cone equivalent (on neat cement paste):
1270 - 1290 °C
- Heat of hydration

6h	340 kJ/kg
24h	445 kJ/kg
5 days	445 kJ/kg

Beyond the minimal requirements of the standard EN 14647, the French production benefits from controls and complementary requirements such as defined in the reference frame NF 002.

Workability - French production

	Specification limit
Spread after 15 min (%)	> 30

The workability of Ciment Fondu® has been determined by measuring the flow properties using the ASTM C230 flow table. The test is carried out using a standard siliceous sand mortar.

Kerneos warrants that the products comply with the specifications stated herein to the exclusion of any other warranty, express or implied. Kerneos makes no representation or warranty of any kind, either express or implied, as to the merchantability or fitness for a particular purpose or use of the products. The warranty shall be limited to the replacement of the non-conforming products or, at Kerneos' option, the refund of the purchase price. Any technical advice, recommendations or information are given based Kerneos' current knowledge and experience of the products and are deemed to be accurate. However, Kerneos undertakes no liability or responsibility of any kind in respect thereof. Users are invited to check that they have the latest version of this document.

- Composition of mortar according to EN 14647: 1350g of sand, 500g of calcium aluminate cement, 200g of water
- Test carried out with 25 shocks after 15 min retained in cone mould, d₁ (diameter of base) = 100mm.
% of flow = d₂ (mm) - d₁ (mm)

	Usual range	Specification limit
Initial set (min)	130 - 200	> 120
Final set (min)	140 - 220	< 240

Mortar setting time - French production

- Composition of mortar according to EN 14647: 1350g of sand, 500g of calcium aluminate cement, 200g of water
- Preparation according to EN 196-1.
- Measurement according to NF P15-431: Vicat test equipment as EN 196-3 but using a 1000g test weight ; temperature 20°C ; samples immersed in water or cured at > 90% relative humidity.
- Final setting time measured in accordance with NF P15-330: the Vicat needle no longer penetrates the mortar.

Mechanical strength - French production

Mechanical strength in MPa		
Age	Modulus of rupture strict specification limit	Compressive strength strict specification limit
6 h	> 4	> 30
24 h	> 5	> 50
28 d	> 6.5	> 60

- Composition of mortar according to EN 14647: 1350g of sand, 500g of calcium aluminate cement, 200g of water
- Test conditions according to EN 196-1: test prisms 40x40x160mm; temperature 20°C ; prisms cured at >90% relative humidity for 24 hours (NF standard) or 6h (BS standard), followed by immersion in water.

4 Storage and Shelf Life

As with all hydraulic binders, Ciment Fondu® must be stored in dry conditions, off the ground. In this case, it will retain its properties for at least 6 months. In many instances, properties are retained for more than one year.



ID	20321	Status	Dato
Risikoområde	Risikovurdering: Helse, miljø og sikkerhet (HMS)	Opprettet	15.06.2017
Opprettet av	Ane Sofie Lilleng	Vurdering startet	15.06.2017
Ansvarlig	Ane Sofie Lilleng	Tiltak besluttet	
		Avsluttet	

Risikovurdering:**CAT, master student, 2018, Ane Sofie Lilleng****Gyldig i perioden:**

-

Sted:

K5-148, K5-228, K5-317, K5-425, K5-448, Kjemihall D

Mål / hensikt

Risikovurdering av arbeidsoppgaver som skal utføres våren 2018 i forbindelse med masteroppgaven.

Bakgrunn

For å kunne gjennomføre masteroppgaven trenger studenten en risikovurdering av aktivitetene som beskrives under seksjonen Beskrivelse og avgrensninger.

Beskrivelse og avgrensninger

- Bruk av HTF2 i kjemihall D til kalsinering (egen opplæring, tilgjengelig risikovurdering på operasjonsprosedyre).
- Behandling og håndtering av pulvermaterialer. Bruk av sikter og siktemaskiner til å sikte og fraksjonere pulver.
- Bæring/bruk av kjemikalierne $Mg(NO_3)_2 \cdot 6H_2O$, $ZrO(NO)_2$, $Ce(NO_3)_3 \cdot 6H_2O$ og $Al(NO_3)_3 \cdot 9H_2O$. Lage vannløsninger med disse kjemikalierne.
- Bruk av vanlig laboratorisk utstyr: Vekt, pH-måler, flasker etc.
- Tørring utført ved ambient trykk og $T < 100$ grader celsius.
- Karakterisering (egen opplæring, tilgjengelig risikovurdering på operasjonsprosedyre). BET, SEM, S(T)EM, XRD, TGA, XRF.
- Materialtest (egen opplæring, tilgjengelig risikovurdering på operasjonsprosedyre). TGA, mikrobalsereaktor.

Forutsetninger, antakelser og forenklinger

Antar fullstendig opplæring før aktivitetene utføres, og at det finnes tilgjengelig risikovurdering for kalsinering, karakterisering og materialtest. Antar at studenten får egen opplæring til disse gjøremålene før aktiviteten skal utføres selv. Forutsetter at studenten har riktig forståelse for frakt og håndtering av kjemikalier, og at studenten har generell forståelse for riktig oppførsel på lab.

Vedlegg

[Ingen registreringer]

Referanser

[Ingen registreringer]



Oppsummering, resultat og endelig vurdering

I oppsummeringen presenteres en oversikt over farer og uønskede hendelser, samt resultat for det enkelte konsekvensområdet.

Farekilde: Fondu sement

Uønsket hendelse: Eksponering på hud og/eller øyne

Konsekvensområde: Helse

Risiko før tiltak:  Risiko etter tiltak: 

Farekilde: Rom K5-425: Bruk av flytende N2

Uønsket hendelse: Hudkontakt med flytende N2

Konsekvensområde: Helse

Risiko før tiltak:  Risiko etter tiltak: 

Farekilde: Rom K5-317: Bruk av kjemikalier

Uønsket hendelse: Uønsket kontakt/hendelse med kjemikalier

Konsekvensområde: Helse

Risiko før tiltak:  Risiko etter tiltak: 

Farekilde: Kontakt med varme flater

Uønsket hendelse: Kontakt med varme flater

Konsekvensområde: Helse

Risiko før tiltak:  Risiko etter tiltak: 

Endelig vurdering

Hendelsene "Hudkontakt med flytende N2" og "Uønsket kontakt/hendelse med kjemikalier" har middels risiko. Likevel vurderer jeg det som forsvarlig å utføre arbeidet enten i løpet av vanlig arbeidstid eller etter arbeidstid. Jeg har vurdert konsekvensen som stor ved disse hendelsene, men samtidig mener jeg det er svært lite sannsynlig at hendelsene inntreffer.

Arbeid etter arbeidstid vil hovedsaklig innebære bruk av TGA, BET og HTF2 i kjemihall D. Bruk av kjemikalier vil for det meste foregå i løpet av vanlig arbeidstid. Dermed vil aktiviteter med akseptabel risiko bli utført etter arbeidstid når jeg er alene på lab.

Involverte enheter og personer

En risikovurdering kan gjelde for en, eller flere enheter i organisasjonen. Denne oversikten presenterer involverte enheter og personell for gjeldende risikovurdering.

Enheter /-er risikovurderingen omfatter

- Institutt for kjemisk prosesssteknologi

Deltakere

Li He
Kumar Ranjan Rout
Edd Anders Blekkan

Lesere

Karin Wiggen Dragsten
De Chen

Andre involverte/interessenter

[Ingen registreringer]

Følgende akseptkriterier er besluttet for risikoområdet Risikovurdering: Helse, miljø og sikkerhet (HMS):

Helse



Materielle verdier



Omdømme



Ytre miljø



Oversikt over eksisterende, relevante tiltak som er hensyntatt i risikovurderingen

I tabellen under presenteres eksisterende tiltak som er hensyntatt ved vurdering av sannsynlighet og konsekvens for aktuelle uønskede hendelser.

Farekilde	Uønsket hendelse	Tiltak hensyntatt ved vurdering
Fondu sement	Eksponering på hud og/eller øyne	
Rom K5-425: Bruk av flytende N2	Hudkontakt med flytende N2	
Rom K5-317: Bruk av kjemikalier	Uønsket kontakt/hendelse med kjemikalier	
Kontakt med varme flater	Kontakt med varme flater	

Eksisterende og relevante tiltak med beskrivelse:

Personlig verneutstyr

Labbriller, labfrakk, ansiktsmaske, labsko. Bruk av syrebestandige hansker, og kulde- og varmebeskyttende hansker ved behov.

Avtrekksskap

Riktig bruk av avtrekksskap. Studenten skal sjekke at avtrekksskapet har tilstrekkelig avtrekk ved testing med papirlapp. Kjemikalier som avgir helsefarlig/brannfarlig gass, sjenerede lukt og støv skal håndteres i avtrekksskap. Glasskjermen skal være trukket lengst mulig ned under arbeidet.

Retningslinjer

- Følge generelle regler på lab for bruk av utstyr og oppførsel.
- Bruk av working-alone-alarm ved arbeid på lab uten andre til stede.
- Være kjent med hvor nærmeste brannslukker, evakueringsrute og møtepunkt er.
- Være kjent med hvor øyeskylleren og dusjen er plassert.
- Være kjent med hvordan gassalarmen fungerer.

Risikoanalyse med vurdering av sannsynlighet og konsekvens

I denne delen av rapporten presenteres detaljer dokumentasjon av de farer, uønskede hendelser og årsaker som er vurdert. Innledningsvis oppsummeres farer med tilhørende uønskede hendelser som er tatt med i vurderingen.

Følgende farer og uønskede hendelser er vurdert i denne risikovurderingen:

- **Fondu sement**
 - Eksponering på hud og/eller øyne
- **Rom K5-425: Bruk av flytende N2**
 - Hudkontakt med flytende N2
- **Rom K5-317: Bruk av kjemikalier**
 - Uønsket kontakt/hendelse med kjemikalier
- **Kontakt med varme flater**
 - Kontakt med varme flater

Detaljert oversikt over farekilder og uønskede hendelser:**Farekilde: Fondu sement**

Produktet kan gi alvorlig øyeskade, irritere huden og kan forårsake irritasjon på luftveiene. Inneholder kjemikalie (r) som skal betraktes som kreftfremkallende.

Uønsket hendelse: Eksponering på hud og/eller øyne

Kontakt med kroppsvæsker kan føre til en sterk basisk reaksjon. Ved kontakt med vann kan produktet virke etsende på hud og øyne. Jevnlig hudkontakt kan gi eksem. Støv og partikler kan rispe og irritere øynene.

Ved disse hendelsene, skyl øyne grundig og fjern eventuelle linser hvis mulig. Ta av tilsølte klær og sko, og vask med mye såpe og vann.

Sannsynlighet for hendelsen (felles for alle konsekvensområder): **Lite sannsynlig (2)**

Kommentar:

Har valgt at det er lite sannsynlig at jeg vil bli eksponert på hud/øyne. Det er fordi jeg vil bruke personlig verneutstyr (støvmaske, vernebriller, labfrakk, tildekkende sko, hansker) ved håndtering av materialet.

Konsekvensområde: Helse

Vurdert konsekvens: **Middels (2)**

Kommentar: Jeg anser konsekvensen som middels dersom

- det oppstår en sterk basisk reaksjon som følge av hudkontakt med materialet og vann/kroppsvæsker.
- jeg får eksem på lang sikt på grunn av langvarig hudeksponering av materialet.
- støvdannelse risper øynene mine.

Risiko:

Farekilde: Rom K5-425: Bruk av flytende N2

N2 adsorpsjon-desorpsjon maskinen benyttes i rom K5-425, og det trengs flytende N2 til testen.

Uønsket hendelse: Hudkontakt med flytende N2

Ved henting og frakt av flytende N2 fra kjemihall D til rom K5-148 er det fare for hudkontakt med N2. Flytende N2 er en nedkjølt gass som kan forårsake alvorlige forfrysninger. Ved alvorlig forfrysning skal den frostskaadede delen varmes opp med lunket vann. Skal ikke gni på området. Lege skal kontaktes umiddelbart.

Sannsynlighet for hendelsen (felles for alle konsekvensområder): **Svært lite sannsynlig (1)**

Kommentar:

Ved håndtering av flytende N2 vil personlig verneutstyr som vernebriller, labfrakk, egnede sko og kuldebestandige hansker bli brukt. Flytende N2 vil bli fraktet til K5-148 i en metallbeholder plassert i en bølge med solid håndtak.

Konsekvensområde: Helse

Vurdert konsekvens: **Stor (3)**

Kommentar: Jeg vurderer konsekvensen som stor dersom jeg får hudkontakt med flytende N2 siden det kan medføre alvorlige forfrysninger.

Risiko:

Farekilde: Rom K5-317: Bruk av kjemikalier

I rom K5-317 vil følgende kjemikalier bli brukt:

Al(NO₃)₃·9H₂O
Mg(NO₃)₂·6H₂O
ZrN₂O₇
Ce(NO₃)₃·6H₂O

Uønsket hendelse: Uønsket kontakt/hendelse med kjemikalier

Kjemikaliene studenten skal benytte har følgende faremomenter:

- Brannfarlig væske/damp
- Gir alvorlig øyeskade
- Kan forårsake døsigheit eller svimmelhet
- Farlig ved svelging
- Gir alvorlig etseskader på hud og øyne
- Irriterer huden
- Kan være etsende for metaller

Alle disse hendelsene er svært uønskede.

Sannsynlighet for hendelsen (felles for alle konsekvensområder): **Svært lite sannsynlig (1)**

Kommentar:

Har valgt at det er svært liten sannsynlighet for hendelsen. Dette er valgt fordi jeg skal

- være forberedt før labarbeid starter (vite hva jeg skal oppnå, hvor mye som skal måles ut, vite i hvilken beholder rester av kjemikalier skal).
- benytte nødvendig verneutstyr ved håndtering av kjemikaliene. Dermed er det liten sannsynlighet for kontakt med hud, hår og øyne.
- ikke jobbe med kjemikaliene rundt åpen flamme/gnister.
- jobbe i avtrekksskap dersom kjemikaliet avgir brannfarlig eller helsefarlig gass.

Konsekvensområde: Helse

Vurdert konsekvens: **Svært stor (4)**

Kommentar: Jeg vurderer konsekvensen som svært stor dersom jeg

- får hud-, hår- eller øyekontakt med kjemikalier som gir alvorlig øyeskade og alvorlige etseskader på hud og øyne.
- puster inn gass som er giftig og som kan skade forplantningsevnen.
- svelger kjemikalier.

Risiko:


Farekilde: Kontakt med varme flater

Kjemihall D: Bruk av High Temperature Furnace 2 (HTF2). Temperaturen i ovnen vil nå 950 C.

Uønsket hendelse: Kontakt med varme flater

HTF2 vil nå temperaturer på 900 C. Den uønskede hendelsen er kontakt med ovnen når programmet kjører. Kontakt med varme flater kan føre til forbrenningsskader. Ved forbrenningsskader skal området skylles med lunket vann.

Sannsynlighet for hendelsen (felles for alle konsekvensområder): **Svært lite sannsynlig (1)**

Kommentar:

Det er svært lite sannsynlig at jeg vil få kontakt med varme flater fordi

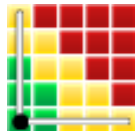
- jeg vil ikke åpne HTF2 før temperaturen er forsvarlig lav. Jeg vil bruke varmeisolerende hansker når skålene med prøver skal hentes ut av ovnen.
- microbalance reactor vil være omgitt av isolerende materiale. Bruk av varmeisolerende hansker.

Konsekvensområde: Helse

Vurdert konsekvens: **Liten (1)**

Kommentar: Vurderer konsekvensen som liten ved kontakt med varme flater fordi

- kontakten med varme flater er svært kort på grunn av reaksjonsevnen.
- jeg vil umiddelbart skylle området med lunkent vann.

Risiko:



Oversikt over besluttede risikoreducerende tiltak:

Under presenteres en oversikt over risikoreducerende tiltak som skal bidra til å redusere sannsynlighet og/eller konsekvens for uønskede hendelser.

Detaljert oversikt over besluttede risikoreducerende tiltak med beskrivelse:



Detaljert oversikt over vurdert risiko for hver farekilde/uønsket hendelse før og etter besluttede tiltak